

A CALORIMETRIC INVESTIGATION OF RECRYSTALLIZATION IN
AL-MG-SI-CU ALLOYS

A CALORIMETRIC INVESTIGATION OF RECRYSTALLIZATION IN
AL-MG-SI-CU ALLOYS

By

MOHAMED ABOU KHATWA, M.Sc., B.Sc.

A Thesis

Submitted to the School of Graduate Studies

in Partial Fulfilment of the Requirements

for the Degree

Doctor of Philosophy

McMaster University

© Copyright by Mohamed Abou Khatwa, June 2009

Vandermeer, R. A., Juul Jensen, D., & Woldt, E. (1997). Grain boundary mobility during recrystallization of copper. *Metallurgical and Materials Transactions A: Physical Metallurgy and Materials Science*, 28 A, 749-754.

Vandermeer, R. A. (1997). On the migration of grain boundaries during recrystallization. In T. R. McNelley (Ed.), *Proceedings of ReX'96, the Third International Conference on Recrystallization and Related Phenomena* (pp. 55-67). Monterey, California: Monterey Institute for Advanced Studies.

Vandermeer, R. A. & Juul Jensen, D. (1998). Migration of high angle grain boundaries during recrystallization. *Interface Science*, 6, 95-104.

Vandermeer, R. A. (2000). Kinetic aspects of nucleation and growth in recrystallization. In N. Hansen, X. Huang, D. Juul Jensen, E. M. Lauridsen, T. Leffers, W. Pantleon, T. J. Sabin, & J. A. Wert (Eds.), *Recrystallization-Fundamental Aspects and Relations to Deformation Microstructure. Proceedings of the 21st Riso International Symposium on Materials Science* (pp. 179-199). Roskilde, Denmark: Riso National Laboratory.

Vandermeer, R. A. & Juul Jensen, D. (2001). Microstructural path and temperature dependence of recrystallization in commercial aluminum. *Acta Materialia*, 49, 2083-2094.

Vandermeer, R. A. (2001). Advances in the study of recrystallization kinetics. In G. Gottstein & D. A. Molodov (Eds.), *Recrystallization and Grain Growth. Proceedings of the First Joint International Conference* (pp. 645-657). Springer-Verlag.

Vandermeer, R. A. & Jensen, D. J. (2003). Recrystallization in hot vs cold deformed commercial aluminum: a microstructure path comparison. *Acta Materialia*, 51, 3005-3018.

Verdier, M., Brechet, Y., & Guyot, P. (1999). Recovery of AlMg alloys: flow stress and strain-hardening properties. *Acta Materialia*, 47, 127-134.

Vyazovkin, S. & Wight, C. A. (1997). Kinetics in Solids. *Annual Review of Physical Chemistry*, 48, 125-149.

Vyazovkin, S. (2001). Two types of uncertainty in the values of activation energy. *Journal of Thermal Analysis and Calorimetry*, 64, 829-835.

Wang, J., Iwahashi, Y., Horita, Z., Furukawa, M., Nemoto, M., Valiev, R. Z. et al. (1996). An Investigation of microstructural stability in an Al-Mg alloy with submicrometer grain size. *Acta Materialia*, 44, 2973-2982.

DOCTOR OF PHILOSOPHY (2009)

MCMASTER UNIVERSITY

(Department of Materials Science and Engineering)

Hamilton, Ontario, Canada

TITLE: A Calorimetric Investigation of Recrystallization in Al–Mg–Si–Cu Alloys

AUTHOR: Mohamed Abou Khatwa, M.Sc., B.Sc.

SUPERVISOR: Dr. Dmitri Malakhov

NUMBER OF PAGES: xvii, 214

*To my mother,
with eternal love and gratitude*

Abstract

The recrystallization behavior of three Al–Mg–Si–Cu alloys with varying iron and manganese additions was studied by differential power scanning calorimetry under non-isothermal annealing conditions. The influence of cold deformation on the precipitation sequence and its interaction with recrystallization was also investigated. The DSC experiments were complemented by hardness measurements and microstructural studies by optical and electron microscopy. The DSC signals, after optimization of the baseline, were used for the calculation of the kinetic parameters of the recrystallization process. Two different modeling approaches based on global JMAK kinetics were implemented. The first approach utilizes the classical isothermal JMAK expression directly, while the second approach introduces a path variable related to the thermal history of the material in the JMAK description. Model-independent estimates of the activation energy were also evaluated using the Flynn-Wall-Ozawa integral isoconversion method.

The results show that the initial stages of recrystallization are not affected by the preceding precipitation processes and recrystallization always follows the precipitation of the Q' phase. However, during recrystallization enhanced coarsening of the Q' phase takes place leading to its transformation to the more stable Q phase. The Q phase exerts a Zener pinning pressures on the migrating boundaries preventing the formation of an equilibrium grain structure. Moreover, for high Fe and Mn additions, discontinuous precipitation of Mg₂Si overlaps with the end of recrystallization and exerts an additional

pinning pressure on the boundaries. Varying the Fe and Mn content significantly affects the recrystallization kinetics. PSN is promoted in alloys with the higher Fe and Mn content and the recrystallization temperature shifts to lower values. The modeling results show that the recrystallization process conforms to the classical JMAK type behavior. The course of the reaction was reproduced successfully by the path variable approach and the evaluated activation energies were in good agreement with the isoconversional model-independent estimates. However, when the classical JMAK expression was applied directly to non-isothermal measurements, a dependency of the recrystallization process on thermal history was observed.

Acknowledgements

I would like to express my deep and sincere gratitude to my supervisor, Dr. Dmitri Malakhov, for his constant support, encouragement, and guidance throughout the entire course of this research. His immense knowledge and meticulous scholarship are inspiring. I would like to thank my supervisory committee members, Dr. David Wilkinson and Dr. Hatem Zurob, for their invaluable comments and insights during the different phases of this research. Their time and expertise are greatly appreciated.

I would like to express my sincere thanks to Dr. Xiang Wang for his help with the TEM investigation, Mr. Mehdi Hossienifier for the many discussions we had and for his valuable assistance during the rolling procedures and Dr. Haiou Jin from Novelis Inc. for the EBSD measurements. I am especially grateful to Novelis Inc. for the financial support of this research.

I am forever indebted to my parents and sisters for their endless support throughout my years at McMaster University. My most heartfelt thanks go to my wife for her steadfast love and encouragement. Finally, I would like to thank my son, Yusef; I am so grateful for your presence in my life.

Table of Contents

Abstract.....	IV
Acknowledgements.....	VI
List of Figures.....	X
List of Tables.....	XVII
CHAPTER 1	1
Introduction.....	1
CHAPTER 2	9
Literature Review.....	9
2.1 Nucleation of Recrystallization.....	9
2.2 Effect of Particles and Precipitation on Recrystallization	11
2.2.1 Recrystallization of Supersaturated Solid Solutions.....	11
2.3 The Effect of Stable Particles on Recrystallization	15
2.4 Interaction Between Recrystallization and Second Phase Particles in Heat-Treatable Aluminum Alloys	17
2.4.1 Second Phase Particles in AA6xxx Series Alloys	18
2.4.2 Recrystallization Kinetics in Al-Mg-Si Automotive Alloys.....	24
CHAPTER 3	32
Phase Equilibria in Al–Mg–Si–Cu Alloys.....	32
3.1 Thermodynamic Estimations	33
3.2 Experiment.....	37
3.2.1 Materials	37
3.2.2 Phase Characterization.....	37
3.3 Results and Discussion	40
3.3.1 Characterization of Intermetallic Phases	40
3.3.2 Thermodynamics of the ζ -phase.....	43
3.4 Re-assessment of the Thermodynamic Properties of the ζ -phase	47
3.5 Conclusions.....	55
CHAPTER 4	57
Recrystallization Kinetics	57
4.1 Formal Kinetics of Primary Recrystallization (The Johnson-Mehl-Avrami-Kolmogorov (JMAK) Model).....	57
4.1.1 Criticisms to the JMAK Equation.....	60
4.2 The Microstructural Path Methodology (MPM).....	68
4.3 Network Models.....	71
4.4 Monte Carlo Simulations	72

CHAPTER 5	74
Experimental Procedure.....	74
5.1 Materials	74
5.2 Cold Rolling.....	75
5.3 Differential Power Scanning Calorimetry	78
5.3.1 Operational Principles.....	78
5.3.2 The Importance of the Baseline	81
5.3.3 Methods of Baseline Construction.....	82
5.4 Calorimetric Studies of Recrystallization	85
5.4.1 DSC Sample Preparation	85
5.4.2 Procedures.....	86
5.4.3 Identification of Thermal Events	86
5.4.4 Quantitative Analysis of the Calorimetric Data.....	89
5.5 Grain Structure Examination	98
5.5.1 Optical Microscopy.....	98
5.5.2 Electron Back Scatter Diffraction (EBSD).....	99
5.6 Hardness Measurements	100
5.7 Transmission Electron Microscopy	100
 CHAPTER 6	 102
Kinetic Modeling of Recrystallization.....	102
6.1 Solid-State Reaction Kinetics from Thermal Analysis.....	103
6.1.1 Isothermal Kinetic Analysis.....	106
6.1.2 Non-Isothermal Kinetic Analysis	107
6.2 Applicability of the Johnson-Mehl-Avrami-Kolmogorov (JMAK) Model to Non-Isothermal Kinetic Analysis	113
6.3 Activation Energy Determination.....	116
6.4 Numerical Solution of the Recrystallization Kinetics	118
6.4.1 Formal JMAK Approach	118
6.4.2 Path Variable Approach for Non-isothermal Transformations.....	123
 CHAPTER 7	 129
Results and Discussion	129
7.1 Thermal Events	129
7.1.1 Effect of Solute Content.....	129
7.1.2 Effect of Cold Rolling.....	133
7.2 The Deformed State	143
7.3 Optical Microscopy.....	145
7.4 Softening Behavior	149
7.5 Electron Back Scatter Diffraction.....	152
7.5.1 Recrystallization Microstructures and Textures	152
7.5.2 Effect of Fe and Mn Contents.....	156
7.6 Thermo-Analytical Analysis of Calorimetric Data.....	162
7.6.1 Recrystallization Temperature Range.....	164

7.7	The Stored Energy of Deformation.....	168
7.7.1	Effect of Solute Content and Degree of Deformation	172
7.8	Recrystallization Kinetics	174
7.8.1	Model-free Estimates of the Activation Energy of Recrystallization.....	175
7.8.2	Formal JMAK Approach	183
7.8.3	The Path Variable Approach.....	189
CHAPTER 8		195
Conclusions.....		195
Bibliography		201
Appendix.....		213

List of Figures

Figure 2.1: Temperature-dependence of the start of precipitation and recrystallization: t_p start of precipitation in an undeformed alloy, t'_p at dislocations, t_r start of recrystallization in a solid solution, t'_r start of recrystallization influenced by precipitating particles. (Hornbogen and Koster, 1978)..... 12

Figure 2.2: Schematic sketch of continuous recrystallization. (Hornbogen and Koster, 1978) 14

Figure 2.3: Schematic diagram of the effect of particle size, volume fraction and prior strain on recrystallization kinetics and mechanisms. (Humphreys and Hatherly, 1995).. 17

Figure 2.4: Dark field TEM micrograph of non-shearable rod-shaped β' precipitates following 4% tensile strain showing fringes due to Orowan looping. (Starke, 1989)..... 19

Figure 2.5: Dark field TEM micrographs of Q' precipitates. (Wang et al., 2006)..... 21

Figure 2.6: Yield stress evolution for the 40% cold rolled AA6111 annealed at 325 °C with different precipitation conditions (T4: naturally aged, T6: peak aged, OA:overaged) and for the solution treated material aged at 325 °C (AG). The data points at a time of 10^{-1} min represent the as-deformed or as solution treated yield stresses. (Go et al., 2003)..... 27

Figure 2.7: TEM micrograph showing the recrystallization front with heterogeneous migration. (Lillywhite et al., 2000)..... 30

Figure 2.8: Schematic representation of the grain boundary migration mechanisms: a) controlled by the phase transformation of β' to β phase and b) controlled by coarsening of β particles. (Lillywhite et al., 2000)..... 31

Figure 3.1: Amounts of intermetallics accumulating in the alloy during casting..... 35

Figure 3.2: Equilibrium amounts of intermetallics..... 35

Figure 3.3: Accumulation of Cu in the FCC phase for the alloy with the composition given in Table 3.1. 36

Figure 3.4: Accumulation of Cu in the FCC phase for the alloy in which the Cu content was changed from 0.2 to 0.7 wt.%. 36

Figure 3.5: Intermetallic particles extracted from the as-cast alloy.....	38
Figure 3.6: Morphologies of thermodynamically stable phases.	39
Figure 3.7: XRD spectra of intermetallic particles.	41
Figure 3.8: Amounts of intermetallics accumulating in the alloy during casting.....	44
Figure 3.9: Equilibrium amounts of intermetallics.	44
Figure 3.10: Influence of decreased Gibbs energies on the contents of the ζ -phase and all intermetallics.....	45
Figure 3.11: Isoplethal section with 2wt. % Fe and 10 wt.% Si (1: L+ β AlFeSi, 2: β AlFeSi+FCC+L, 3: FCC+L+ ζ and 4: β AlFeSi+Si+FCC).	48
Figure 3.12: Isoplethal section with 2wt. % Fe and 14 wt.% Si (1: L+ β AlFeSi, 2: L+Si+ β AlFeSi, 3: Si+L+ ζ and 4: β AlFeSi+Si+FCC).	48
Figure 3.13: Isoplethal section with 1 wt.% Fe and 10 wt.% Si (1: L+ β AlFeSi, 2: L+ β AlFeSi+ ζ , 3: L+ β AlFeSi+FCC, 4: L+ β AlFeSi+FCC+ ζ , 5: FCC+L+ ζ , 6: β AlFeSi+Si+FCC and 7: FCC+Si+ ζ).	52
Figure 3.14: Isoplethal section with 1 wt.% Fe and 14 wt.% Si (1: L+ β AlFeSi, 2: L+ β AlFeSi+ ζ , 3: L+ β AlFeSi+Si, 4: β AlFeSi+Si+L+ ζ , 5: L+Si+ ζ , 6: β AlFeSi+Si+FCC and 7: FCC+Si+ ζ).	52
Figure 3.15: Isoplethal section with 2 wt.% Fe and 10 wt.% Si (1: L+ β AlFeSi, 2: β AlFeSi+FCC+L, 3: FCC+L+ ζ , 4: α AlMnSi+FCC+L+ ζ , 5: β AlFeSi+Si+FCC and 6: FCC+Si+ ζ).	53
Figure 3.16: Isoplethal section with 2 wt.% Fe and 14 wt.% Si (1: L+ β AlFeSi, 2: L+Si+ β AlFeSi, 3: β AlFeSi+Si+FCC, 4: FCC+Si+ ζ and 5: α AlMnSi+Si+FCC+ ζ).	53
Figure 3.17: Isoplethal section with 3 wt.% Fe and 10 wt.% Si (1: L+ β AlFeSi, 2: L+FCC+ β AlFeSi, 3: FCC+L+ ζ , 4: β AlFeSi+Si+FCC and 5: Si+FCC+ ζ).	54
Figure 3.18: Isoplethal section with 3 wt.% Fe and 14 wt.% Si (1: L+ β AlFeSi, 2: β AlFeSi+Si+L, 3: Si+L+ ζ , 4: β AlFeSi+Si+FCC and 5: Si+FCC+ ζ).	54
Figure 3.19: Isothermal section at 660°C (933.15 K) with 10 wt.% Si (1: L+ β AlFeSi and 2: L+ β AlFeSi+ ζ).	55

Figure 3.20: Isothermal section at 580°C (853.15 K) with 10 wt.% Si (1: L+Si+βAlFeSi).	55
Figure 3.21: Isothermal section at 660°C (933.15 K) with 14 wt.% Si (1: L+βAlFeSi and 2: L+βAlFeSi+ζ).	55
Figure 3.22: Isothermal section at 580°C (853.15 K) with 14 wt.% Si (1: L+Si+βAlFeSi).	55
Figure 4.1: The basis of the Monte Carlo simulation method. (Humphreys and Hatherly, 1995)	73
Figure 5.1: Phase Stability diagrams for: (a) 6111-NC, (b) 6111-HC and (c) 6111-LC..	76
Figure 5.2: Schematic cross-section of a Pyris Diamond power-compensation DSC. (Starink, 2004)	78
Figure 5.3: Schematic curve for a first-order phase transition. (Hemminger and Sarge, 1991)	81
Figure 5.4: Successive DSC scans of deformed Al–Mg–Si–Cu samples illustrating the inapplicability of canonical methods to calorimetric recrystallization studies: a) 6111- NC-90, b) 6111-HC-90 and c) 6111-LC-90.	88
Figure 5.5: Points corresponding to the onset and finish of a transformation and estimated slopes at these points.....	93
Figure 5.6: Experimental points and the slopes are used for building a spline describing the heat flux curve and a spline $g_2(t)$ connecting the first and last points of the peak. ..	94
Figure 5.7: Calculated $g_2(t)$ in all peak points are used for building an initial approximation to a baseline.	95
Figure 5.8: Iterations resulting in a self-consistent baseline.....	96
Figure 6.1: Schematic representation of the dependence of the stage of transformation on the thermal history for a thermally activated transformation. (Mittemeijer, 1992)	124
Figure 7.1: DSC thermogram for 6111-NC-SHT alloy at scan rates of 20 and 40 °C/min.	131
Figure 7.2: DSC thermograms for 6111-LC-SHT and 6111-HC-SHT at a scan rate of 40 °C/min.	132

Figure 7.3: DSC thermograms for undeformed and cold rolled 6111-NC alloys at a scan rate of 40 °C/min.....	133
Figure 7.4: TEM micrographs of a 6111-NC-90 sample heated up to 330 °C at a rate of 40 °C/min: a) BF image, b) DF image and c) the corresponding [001] _{Al} SADP.....	136
Figure 7.5: TEM micrograph of a 6111-NC-90 sample heated up to 330 °C at a rate of 40 °C/min illustrating the deformation microstructure as well as recovery and recrystallization effects.	139
Figure 7.6: TEM micrograph of a 6111-NC-90 sample heated up to 400 °C at a rate of 40 °C/min.	139
Figure 7.7: TEM micrograph of a 6111-NC-90 sample heated up to 460 °C at a rate of 40 °C/min.	140
Figure 7.8: DSC thermograms for 6111-LC-90 and 6111-HC-90 at a scan rate of 40 °C/min.	141
Figure 7.9: TEM micrograph of a 6111-HC-90 sample heated up to 500 °C at a rate of 40 °C/min, illustrating the formation of equilibrium Mg ₂ Si precipitates.	142
Figure 7.10: EDS spectrum from the fine Mg ₂ Si precipitates.	142
Figure 7.11: EDS spectrum from the large intermetallic particles.	143
Figure 7.12: TEM micrograph of as-rolled 6111-HC-90.....	144
Figure 7.13: TEM micrograph of as-rolled 6111-HC-90 illustrating an almost uniform distribution of dislocations.....	144
Figure 7.14: Development of microstructure in 6111-NC-90 during linear heating at a rate of 40 °C/min: a) as-deformed, b) 340 °C quench, c) 390 °C quench, d) 430 °C quench, e) 450 °C quench and f) 470 °C quench.....	147
Figure 7.15: Development of microstructure in 6111-LC-90 during linear heating at a rate of 40 °C/min: a) 410 °C quench and b) 480 °C quench.....	148
Figure 7.16: Development of microstructure in 6111-HC-90 during linear heating at a rate of 40 °C/min: a) 450 °C quench and b) 500 °C quench.....	148
Figure 7.17: Variation of Vickers hardness with temperature during annealing of 6111-NC-90 (heating rate=40 °C/min).	150

Figure 7.18: Variation of Vickers hardness with temperature during annealing of 6111-HC-90 (heating rate=40 °C/min).	150
Figure 7.19: Variation of Vickers hardness with temperature during annealing of 6111-LC-90 (heating rate=40 °C/min).	151
Figure 7.20: Orientation map of 6111-NC-90 quenched from 460 °C. The RD is vertical and the ND is horizontal.	154
Figure 7.21: Orientation map of 6111-NC-90 quenched from 460 °C illustrating the clustering of small recrystallized grains in the vicinity of large second-phase particles. The RD is vertical and the ND is horizontal.	154
Figure 7.22: Histogram of grain size distribution in 6111-NC-90 quenched from 460 °C.	155
Figure 7.23: Orientation maps showing the spatial distribution of the Cube texture (a) and the Goss texture (b) for a 6111-NC-90 sample quenched from 460 °C. The RD is vertical and the ND is horizontal.	156
Figure 7.24: Orientation map of 6111-HC-90 quenched from 500 °C. The RD is vertical and the ND is horizontal.	157
Figure 7.25: Histogram of grain size distribution in 6111-HC-90 quenched from 500 °C.	158
Figure 7.26: TEM micrograph of 6111-HC-90 quenched from 500 °C illustrating additional boundary pinning by Mg ₂ Si precipitates.	159
Figure 7.27: Orientation maps showing the spatial distribution of the Cube texture (a) and the Goss texture (b) for the 6111-HC-90 sample quenched from 500 °C. The RD is vertical and the ND is horizontal.	160
Figure 7.28: Orientation map of 6111-LC-90 quenched from 480 °C. The RD is vertical and the ND is horizontal.	161
Figure 7.29: Histogram of grain size distribution in 6111-LC-90 quenched from 480 °C.	161
Figure 7.30: Orientation maps showing the spatial distribution of the Cube texture (a) and the Goss texture (b) for the 6111-LC-90 sample quenched from 480 °C. The RD is vertical and the ND is horizontal.	162

Figure 7.31: Samples of isolated recrystallization peaks with the constructed baselines for DSC scans recorded at a rate of 40 °C/min: a) 6111-NC-90, b) 6111-HC-90 and c) 6111-LC-90.	163
Figure 7.32: Recrystallization temperature ranges for the 6111-NC alloy as a function of heating rate and degree of deformation.	165
Figure 7.33: Recrystallization temperature ranges for the 6111-HC alloy as a function of heating rate and degree of deformation.	166
Figure 7.34: Recrystallization temperature ranges for the 6111-LC alloy as a function of heating rate and degree of deformation.	167
Figure 7.35: Effect of solute content and degree of deformation on the recrystallization temperature.	168
Figure 7.36: Variation of stored energy with heating rate for the 6111-NC alloy.....	169
Figure 7.37: Variation of stored energy with heating rate for the 6111-HC alloy.....	170
Figure 7.38: Variation of stored energy with heating rate for the 6111-LC alloy.....	171
Figure 7.39: Effect of solute content and degree of deformation on the stored energy of deformation.	174
Figure 7.40: Flynn-Wall-Ozawa isoconversional plots for the 6111-NC alloy: a) 80% and b) 90% cold rolling reduction.	177
Figure 7.41: Dependence of the activation energy on extent of conversion for the 6111-NC alloy using the FWO method.....	178
Figure 7.42: Flynn-Wall-Ozawa isoconversional plots for the 6111-LC alloy: a) 80% and b) 90% cold rolling reduction.	180
Figure 7.43: Dependence of the activation energy on extent of conversion for the 6111-LC alloy using the FWO method.	181
Figure 7.44: Flynn-Wall-Ozawa isoconversional plots for the 6111-HC alloy: a) 80% and b) 90% cold rolling reduction.	182
Figure 7.45: Dependence of the activation energy on extent of conversion for the 6111-HC alloy using the FWO method.....	183

Figure 7.46: Recrystallization kinetics for the 6111-NC alloy during non-isothermal annealing at various heating rates: a) 80% and b) 90% cold rolling reduction. 184

Figure 7.47: Recrystallization kinetics for the 6111-LC alloy during non-isothermal annealing at various heating rates: a) 80% and b) 90% cold rolling reduction. 185

Figure 7.48: Recrystallization kinetics for the 6111-HC alloy during non-isothermal annealing at various heating rates: a) 80% and b) 90% cold rolling reduction. 186

Figure 7.49: Effect of solute content and degree of deformation on the Avrami exponent evaluated from the formal JMAK approach. 188

Figure 7.50: Recrystallization kinetics by the path variable approach for the 6111-NC alloy during non-isothermal annealing at various heating rates: a) 80% and b) 90% cold rolling reduction..... 191

Figure 7.51: Recrystallization kinetics by the path variable approach for the 6111-LC alloy during non-isothermal annealing at various heating rates: a) 80% and b) 90% cold rolling reduction..... 192

Figure 7.52: Recrystallization kinetics by the path variable approach for the 6111-HC alloy during non-isothermal annealing at various heating rates: a) 80% and b) 90% cold rolling reduction..... 193

Figure 7.53: Effect of solute content and degree of deformation on the Avrami exponent evaluated from the path variable approach. 194

List of Tables

Table 2.1: Structural variance of common intermetallic phases in 6xxx Al alloys (Claves et al., 2002)	24
Table 2.2: Heat treatments, recrystallization time and the resultant grain sizes for the samples isothermally annealed at 300 °C.....	28
Table 3.1: Chemical composition of the alloy investigated in wt.%	33
Table 3.2: Sublattice models of phases.....	34
Table 3.3: Experimentally determined weight % of intermetallic phases	40
Table 3.4: Elemental ratios for intermetallics extracted from the heat-treated alloy.....	43
Table 3.5: Comparison between experimentally measured and calculated liquidus temperatures (differences are given in parentheses).....	50
Table 4.1: Values of n in the JMAK kinetic relation (Christian, 1975)	60
Table 5.1: Chemical composition of the investigated alloys in wt.%.....	75
Table 5.2: Processing route and sample designation	77
Table 7.1: Residual calorimetric stored energy released during recrystallization.....	171
Table 7.2: Recrystallization kinetic parameters evaluated from the formal JMAK approach.....	188
Table 7.3: Recrystallization kinetic parameters evaluated from the path variable approach	194

CHAPTER 1

Introduction

Due to an increasing demand for satisfying the North American corporate average fuel efficiency standards, there is a growing need for the reduction of vehicle body weight in the automotive industry. Estimates reveal that 8-10% fuel economy improvement could be achieved for a 10% of vehicle weight reduction. This has driven tremendous efforts towards the replacement of steel and cast iron with alternative lighter weight material in vehicles production. Aluminum, with its good formability, corrosion resistance and high stiffness stands out as one of the most potential candidates for such replacement (Miller et al., 2000; Quainoo and Yannacopoulos, 2004). Current areas of application in the automotive industry include the use of aluminum sheets for the exterior body panels. In North America, age-hardenable Al–Mg–Si–Cu alloys such as 6111, have been the alloys of choice for such application. This stems from their satisfaction of the competing requirements of low yield strength sheet for formability and high yield strength component for dent resistance. Such requirement is fulfilled through the paint bake cycle which is carried out at an average temperature of 175 °C for 30 minutes and thus, only achieves a fraction of the total aging potential which requires 8 hours at such temperature (Bryant, 1999). However, the cost of aluminum alloy sheets remains a limiting factor against its full exploitation in industry in comparison to steel sheets.

A substantial part of this cost is due to traditional multi-step thermomechanical processes employed for achieving the final structural properties of flat-rolled sheets. During metal fabrication, the increase in dislocation density associated with deformation impedes further processing. Therefore, intermediate annealing steps are essential in order to soften the material and allow further formability. The intermediate heat treatments are also intended for optimizing the engineering properties of the sheets through grain size and texture control. For example, while formation of recrystallized grains with the cube texture component decreases the anisotropic behavior of cold rolled aluminum sheets during forming (Weiland, 1995), their profound existence and segregation along the rolling direction is identified as the main reason behind the occurrence of roping. This limits sheet formability and deteriorates its surface quality (Engler and Hirsch, 2002; Jin and Lloyd, 2005). Consequently, a balance between the recrystallized and retained deformation textures is vital to improve formability and surface appearance of aluminum sheets. Such balance could be achieved by controlling the precipitation states during thermomechanical processing. Large particles promote recrystallization by particle stimulated nucleation (PSN) resulting in weak or near random recrystallization texture. On the other hand, small Mg_2Si particles suppress the motion of high angle grain boundaries during recrystallization leading to pronounced cube recrystallization texture components with an inherited banded structure from the rolled sheets. Therefore, the development of alternative one or two step process routes for microstructural and texture control over aluminum sheet products is desirable in terms of complying with both better forming properties and cost reductions of raw sheets. However, with a decreased

complexity of the thermomechanical processing schedule, opportunities for tailoring a desired microstructure or microtexture will be limited. As a result, recrystallization becomes a key process in controlling the final structures and properties of the material. Therefore, predicting the relations among its various aspects and the thermomechanical process parameters during sheet manufacturing is a crucial step towards improved process design and optimization of the annealing treatments. This requires an understanding of the interactions of processing and alloy variables with recrystallization and the associated kinetics of nucleation and grain growth. The parameters which are commonly known to control recrystallization processes are the stored energy of deformation, the solute elements and the second phase particles (Weiland, 2004).

Investigation of recrystallization processes entails a through consideration of two important aspects. First, a proper assessment of the progress of the reaction and, second, the acquisition of representative experimental data. Various experimental methods have been employed in measuring recrystallization through the temporal evolution of different microstructural features, such as grain morphology, texture and dislocation densities. Metallography either by optical or electron microscopy provides quantitative information on the volume fraction of recrystallized material and/or the stored energy by observing grains morphologies, local misorientations and dislocations using a series of measurements of “frozen states” of the material along the annealing path. Quantification of recrystallization can also be based on the associated softening behavior of the material either by yield stress measurements or hardness measurements, or by the development of

the different texture components representing the deformed or recrystallized states as obtained by X-ray diffraction, laser ultrasonics and neutron diffraction (Woldt and Jensen, 1995; Kruger et al., 2003). In addition, 3D maps of recrystallized grain structures can be reconstructed from diffraction data obtained by the 3D X-ray Diffraction (3DXRD) microscope employing synchrotron radiation (Jensen and Poulsen, 2000). Nucleation and growth rates of new grains can also be monitored in-situ by 3DXRD. The time and/or temperature dependent release of the stored energy of deformation is also directly measured using a calorimeter. While all the above mentioned methods have been successfully employed in recrystallization studies, calorimetry, in general, and differential scanning calorimetry (DSC), in particular, hold a set of advantages. Firstly, DSC data is a volume-integrated signal that is not limited to selected regions of the sample. Thus, it yields information on a large volume of material without any interference with the occurring transformation (Hemminger and Sarge, 1991; Haessner, 1992). Secondly, recrystallization resembles the crystallization of a melt where the material transforms by nucleation and growth processes. Therefore, its kinetics is usually described within the framework of the mathematical treatment of the JMAK model. The essence of the calorimetric data is that it directly compares to the model under the assumption of a homogeneous dislocation distribution where the recrystallized volume will be proportional to the released stored energy. The kinetics of primary recrystallization can also be characterized by the solid-state reaction kinetic theory that is readily evaluated from multiple isothermal or non-isothermal calorimetric experiments. This flexibility in employing both isothermal and non-isothermal conditions for the study

of recrystallization kinetics, coupled with the development of relevant thermal analysis procedures has contributed significantly to the revival of calorimetry as an essential tool for the investigation of the recrystallization phenomenon. Thirdly, the ease of sample preparation, the speed of data acquisition and the improved accuracy in the measuring system are also important advantages in comparison to the elaborate nature of experimental stereological methods.

The recrystallization process in 6xxx series aluminum alloys is usually complicated by the multiplicity of alloying elements which leads to the precipitation of a vast number of phases either during solidification or during the subsequent solutionizing treatments. These phases are known to affect the recrystallization kinetics by influencing the nucleation and growth rates. Large particles serve as preferential sites for nucleation of new grains (PSN) while small particles pin the boundaries of growing grains (Zener drag). In addition, most of these second-phase particles are not in thermodynamic equilibrium and can dissolve or re-precipitate during annealing (Hornbogen and Koster, 1978). This complicates the analytical modeling of the recrystallization processes. As a result, the traditional focus has been on the effects of stable second-phase particles on the recovery and recrystallization processes with only minor attention to the interaction of recrystallization and phase transformations where particles can precipitate, coarsen or dissolve during the recrystallization anneal. In order to capture such interaction, the whole annealing process has to be monitored. Non-isothermal calorimetric experiments permit such observations by offering continuous curves covering the whole temperature

range of the process of interest. This allows for a microscopic-atomic scale analysis of the kinetics of the occurring phase transformations, and at the same time emphasizes areas for further investigation by complementary techniques. In addition, non-isothermal analysis resolves overlaps between occurring phase transformations. This is due to the distinction between the first and final stages of a transformation based on the associated temperatures, while in isothermal analysis intermediate overlapping transformations may be overlooked (Mittemeijer, 1992). Another major advantage of non-isothermal analysis is the broad experimental temperature ranges. Under isothermal conditions, a solid-state process usually has a maximum reaction rate at the beginning of transformation. Consequently, a high experimental temperature may result in disregarding initial transformations that may influence the remaining kinetic analysis (Mittemeijer, 1992; Vyazovkin and Wight, 1997). On the other hand, a low experimental temperature may result in insufficient heat flow and reduced accuracy due to the excessive noise levels (Schonborn and Haessner, 1985). Hence, the use of isothermal analysis requires pre knowledge of the appropriate temperatures for the experiment. This is a drawback in comparison to the blind scan mode in non-isothermal analysis which clearly identifies the complete reaction course. Also, rapid phase transformations may remain unnoticed during isothermal analysis due to transients within the measuring apparatus and the accompanying uncertainty of the reaction start time before establishing the isothermal temperature. Moreover, industrial processes are usually carried out under non-isothermal conditions, thereby increasing the need for an equivalent thermal analysis technique (Henderson, 1979). Finally, the higher heat flows encountered in continuous heating DSC

measurements improves the accuracy over isothermal experiments (Woldt, 1992; Kruger, 1993).

Based on the aforementioned benefits of non-isothermal calorimetry, DSC was selected as the main experimental technique in this study for the investigation of the recrystallization process in a heat-treatable Al–Mg–Si–Cu alloy. This includes assessment of the interactions between precipitation and recrystallization along the heat treatment path.

Following this introduction, Chapter 2 presents the fundamentals of primary recrystallization with an emphasis on recrystallization in supersaturated solid solutions. The chapter also includes reviews of precipitation reactions in Al–Mg–Si alloys and their interaction with recrystallization. Chapter 3 discusses the nature of the dominant intermetallics in the 6xxx alloys together with a thermodynamic assessment of their inherent stability during high temperature annealing. Chapter 4 outlines the phenomenological approaches to modeling recrystallization kinetics as well as recent developments. Chapter 5 summarizes the experimental procedures. Special emphasis is given to the generation and treatment of the calorimetric data in order to extract reliable kinetic information. Chapter 6 outlines the solid-state reaction kinetic theory and the developed kinetic models for non-isothermal recrystallization analysis. Chapter 7 presents the experimental results accompanied by an analysis of the precipitation

reactions and the recrystallization kinetics. Finally, chapter 8 presents the main conclusions drawn from the calorimetric investigation.

CHAPTER 2

Literature Review

This chapter provides an overview of the recrystallization phenomenon and its interaction with precipitation. The chapter begins with a description of recrystallization with special emphasis on recrystallization of supersaturated solid solutions and the effect of stable particles on recrystallization. Focus is then directed towards recrystallization in heat treatable 6xxx series aluminum alloys. Occurring precipitation processes and second phase particles are discussed. Finally, studies pertaining to the interaction between recrystallization and phase transformations in the automotive 6xxx alloys are reviewed.

2.1 Nucleation of Recrystallization

Recrystallization is the process by which new strain free grains nucleate, grow and consume a previously deformed matrix. The process is thermally activated and is driven by the stored energy of deformation in the matrix. The control over recrystallization entitles proper understanding of the nucleation process as the orientation and spatial distributions of the new recrystallized grains are determined by the nucleation events (Humphreys and Hatherly, 1995; Humphreys, 2004). Although several nucleation mechanisms have been proposed, many aspects of the process are still not properly understood. This results from the absence of an experimental technique capable of

providing a 3D in-situ method to resolve dislocations and hence relate the deformed and annealed microstructures (Humphreys, 2004).

Despite the incomplete picture concerning the nucleation process, it is now accepted that the main mechanisms for nucleation involve the growth of subgrains by low angle boundary migration (LAGB) in an orientation gradient or the strain induced grain boundary migration (SIBM). Examples of nucleation within an orientation gradient include areas of inhomogeneities in the deformed microstructure such as transition bands, shear bands and deformation zones around second phase particles (Humphreys and Hatherly, 1995). In commercial aluminum alloys, the later mechanism is considered the most prevailing nucleation mechanism and is known as particle-stimulated nucleation of recrystallization (PSN). The resulting recrystallized grains will have orientations already found in the deformed structure. However, recrystallized grains with orientations different from the deformed structure have been also reported for aluminum alloys without a clear explanation or theory behind this phenomenon. Interfaces with secondary phases have been also shown to induce twinning on annealing resulting in the formation of recrystallization nuclei with orientations not present in the deformed microstructure (Humphreys, 2004). Although twinning in metals with high stacking fault energy as aluminum is infrequent, Lillywhite et al. (2000) have shown that annealing twins can form in aluminum alloys under conditions where fine particle dispersions retard recrystallization. This phenomenon was attributed to the lower interfacial energy of twin boundaries which reduces the effect of Zener pressure. On the other hand, SIBM has been

shown to be the dominant recrystallization mechanism occurring at low strains and after high temperature deformations. It is favored in materials with poor developed dislocation cell structures and significant Zener pinning by second phase particles. It involves the bulging of a part of a pre-existing grain boundary which then migrates due to the difference in stored energies on opposite sides of the boundaries. The migrating boundary may be adjacent to multiple subgrains or only a single large subgrain. The new grains will have the same orientations as the old grains from which they originated (Humphreys, 2004).

2.2 Effect of Particles and Precipitation on Recrystallization

2.2.1 Recrystallization of Supersaturated Solid Solutions

Precipitation and recrystallization are known to exert a mutual influence. In a deformed and supersaturated alloy containing phases not in thermodynamic equilibrium, precipitation of the second phase particles can occur simultaneously with recrystallization during heating. Precipitating particles are known to delay the rearrangement of dislocations to form recrystallization fronts and their subsequent migration. However, the precipitation of particles in the recrystallization front from a supersaturated matrix will provide a driving force for grain-boundary migration known as the driving force due to discontinuous precipitation which increases the velocity of a recrystallization front. By studying the temperature-dependence of the start of both precipitation and

recrystallization reactions, Hornbogen and Koster (1978) distinguished three ranges in the recrystallization behavior as shown in Figure 2.1.

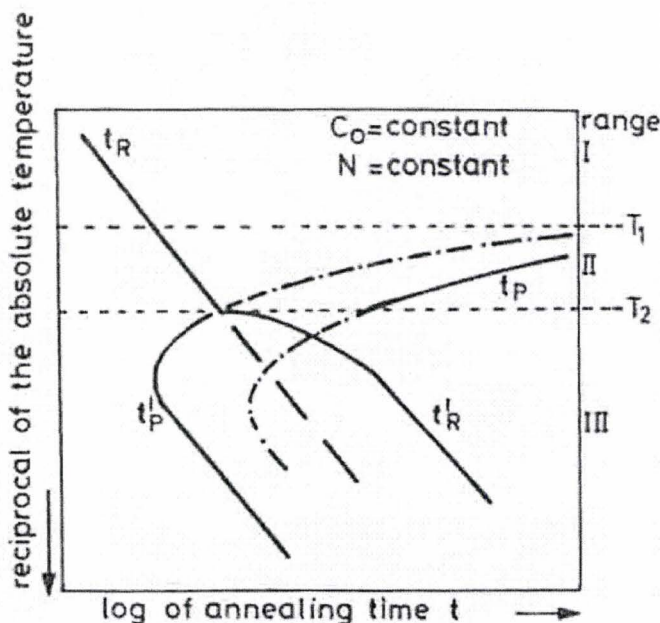


Figure 2.1: Temperature-dependence of the start of precipitation and recrystallization: t_p start of precipitation in an undeformed alloy, t'_p at dislocations, t_r start of recrystallization in a solid solution, t'_r start of recrystallization influenced by precipitating particles. (Hornbogen and Koster, 1978)

The mutual influence between precipitation and recrystallization processes occurs at a specific transition temperature above which recrystallization is only influenced by segregation of the particles and precipitation either does not occur or starts after the completion of recrystallization. Below this specific temperature for the mutual influence, the condition for the migration of a recrystallization front assuming the existence of a grain-boundary capable of migration (i.e. discontinuous recrystallization) is expressed by (Hornbogen and Koster, 1978):

$$F_N + F_C > F_P + F_S \quad (2.1)$$

where F_N is the driving force due to the elimination of dislocations or subgrain boundaries given by:

$$F_N = Gb^2(N_0 - N_1) \quad (2.2)$$

G is the shear modulus, b is the Burgers vector and N_0 and N_1 are the dislocation densities in the deformed and recrystallized regions, respectively. F_C is the driving force due to discontinuous precipitation or due to metastable particles transforming into stable ones and is expressed by:

$$F_C = \frac{1}{V} \Delta g_C - \frac{1}{V} \Delta g_0 \quad (2.3)$$

where V is the molar volume, Δg_C is the difference in free energy of the supersaturated crystal in which decomposition occurred and Δg_0 is the interfacial energy necessary for the particles. F_p is the retarding force due to precipitated stable particles, also known as the Zener pinning pressure, and F_s is the retarding force due to the segregation of foreign atoms from the solid solution, both given by the expressions:

$$F_p = \frac{3f\sigma_b}{2r} \quad (2.4)$$

$$F_s = \lambda v + \frac{\delta c v}{1 + \kappa^2 v^2} \quad (2.5)$$

where f is the volume fraction of the particles, σ_b is the surface energy of the boundary per unit area, r is the radius of the particle, λ is the inverse of the intrinsic mobility, δ and κ are solute drag parameters depending on the nature and type of solute, c is the solute concentration, and v is the boundary velocity (Vandermeer, 1997).

In the case of absence of migrating boundaries, the segregation of impurity atoms or the occurrence of preferential precipitation of particles at dislocations; recrystallization will be controlled by the formation or resolution of the precipitated particles through the process known as continuous recrystallization. In this process as seen in Figure 2.2, subgrain boundaries anneal out by coalescence upon the dissolution of small particles pinning the dislocations and the dislocation networks assume the character of grain boundaries allowing for further growth. The resulting distribution of grain size, particles and texture differs from that of a discontinuously recrystallized structure (Hornbogen and Koster, 1978).

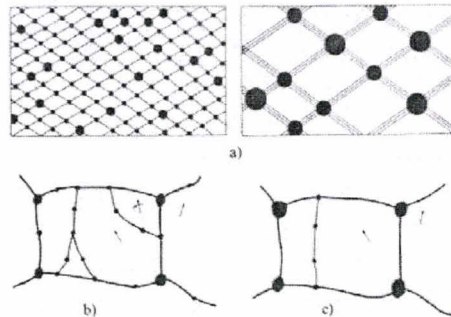


Figure 2.2: Schematic sketch of continuous recrystallization. (Hornbogen and Koster, 1978)

2.2.1.1 Factors Affecting Recrystallization in Supersaturated Solid Solutions

Whenever there is a mutual influence between precipitation and recrystallization processes, the factors affecting such influence can be deduced from the above equations of the driving and retarding forces acting on the grain-boundaries and include: temperature, dislocation density and annealing time. Decreasing temperature will

decrease both the incubation time for precipitation and solubility resulting in a smaller particle size hindering both the rearrangement of dislocations and the migration of grain-boundaries. Dislocation density on the other hand has a more complicated effect. Generally, an increase in the dislocation density will shift recrystallization to shorter time periods on the assumption that dislocations do not affect the start of precipitation. However, with increasing deformation, the incubation period for continuous precipitation is decreased resulting in a decrease in the driving force due to discontinuous precipitation and a simultaneous increase in the retarding force due to the precipitated particles.

A combination of these effects may cease the condition for discontinuous recrystallization and a transition to individual precipitation at dislocations and continuous recrystallization occurs. Increasing the annealing time will also affect the reaction front. Longer time implies a decrease in the driving force for grain-boundary migration coupled with a decrease in the chemical force and an increase in the particles retarding force due to coarsening. The resultant force acting on the reaction front will thus decrease until eventually the condition for discontinuous recrystallization is no longer satisfied (Hornbogen and Koster, 1978).

2.3 The Effect of Stable Particles on Recrystallization

Upon deformation of alloys containing a dispersion of thermodynamically stable particles, three possible effects may occur depending on the size, shape and mechanical properties of the particles. Brittle particles can be sheared by dislocations leading to their mechanical dissolution. The effect is enhanced if many operative slip systems are in

effect and an inhomogeneous supersaturated solid solution is created. The recrystallization behavior of such supersaturated solid solution will follow the same guidelines discussed above. On the other hand, small hard particles which remain stable during plastic deformation will induce a state of microscopic homogeneity of strain. However, large hard incoherent particles will generate dislocations at their interfaces resulting in local inhomogeneities (Hornbogen and Koster, 1978). These second phase particles not only increase the driving force for recrystallization by increasing the dislocation density, but also alter the deformation structure by the creation of local lattice distortions around each particle known as the deformation zone of the particle. Such areas serve as favorable nucleation sites for the recrystallizing grains leading to the effect known as particle-stimulated nucleation. However, experimental investigations have shown that such effect is associated with a minimum particle diameter of about $1\mu\text{m}$ below which the local curvatures of the matrix lattice either do not exist or are insufficient to assist in the formation of potential nucleation sites for the recrystallizing grains (Hornbogen and Koster, 1978; Humphreys and Hatherly, 1995). In such case, small particles will retard recrystallization by exerting a Zener drag pressure on the migrating grain boundaries.

The recrystallization kinetics has been shown to be greatly affected by the interparticle spacing. In the presence of closely spaced particles, recrystallization is retarded or even completely inhibited and the deformed or recovered microstructure can be retained up to high temperatures (Humphreys and Hatherly, 1995). The reason lies in

the absence of a sufficient number of sub-boundaries between the particles for the formation of mobile high-angle grain boundary. The transition from accelerated to retarded recrystallization depends on the volume fraction of the particles, the particle radius and the strain level as shown schematically in Figure 2.3. It has been proposed that an interparticle spacing greater than twice the deformation cell diameter is necessary for accelerating recrystallization (Hornbogen and Koster, 1978).

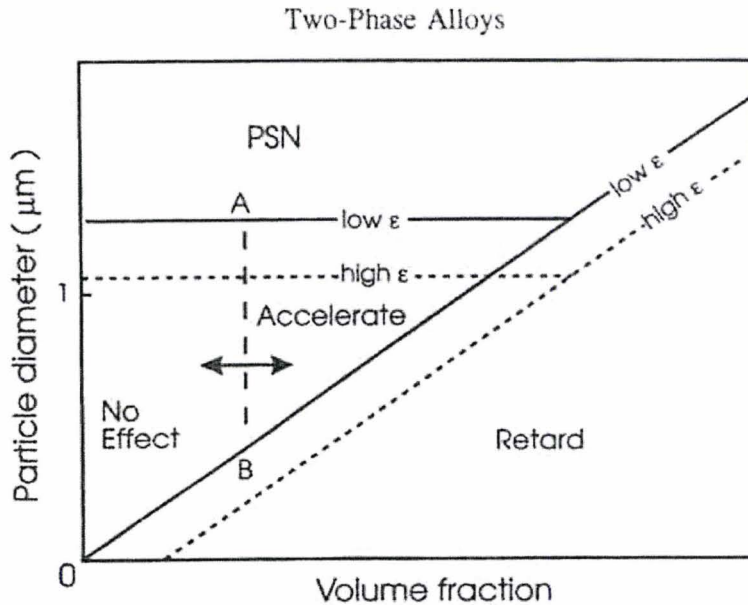


Figure 2.3: Schematic diagram of the effect of particle size, volume fraction and prior strain on recrystallization kinetics and mechanisms. (Humphreys and Hatherly, 1995)

2.4 Interaction Between Recrystallization and Second Phase Particles in Heat-Treatable Aluminum Alloys

As mentioned earlier, most studies dealing with the interaction between recrystallization and second phase particles focused on the Zener pinning effects and

particle-stimulated nucleation associated with stable particles. Only few investigations were directed towards the interaction of recrystallization and phase transformations occurring during the recrystallization anneal. The following section highlights those studies especially ones concerned with automotive 6xxx series alloys; but first a brief description of the second phase particles forming in the alloy is presented.

2.4.1 Second Phase Particles in AA6xxx Series Alloys

The 6xxx series alloys are age hardenable aluminum alloys with medium strength, good weldability and corrosion resistance. The major alloying elements are magnesium and silicon (0.4-1.5% each) which are usually added in balance to form the pseudo-binary Al-Mg₂Si (Mg:Si=1.73) for strengthening by the formation of metastable precursors of the equilibrium phase Mg₂Si. The presence of excess Si in the alloys improves the age hardening response by refining the size of the Mg₂Si particles and by precipitating as Si. Copper additions improve strength and machinability but with a substantial loss of corrosion resistance. Small Cu additions of about 0.25 wt.% slow down natural aging and/or increase the response to artificial aging. Additions of Mn and Cr promote the formation of fine grain size and inhibit recrystallization during solution heat treatment (Tiryakioğlu and Staley, 2003). The alloys are usually aged between 140-185 °C and follow a complex precipitation process involving several metastable transitional phases with crystal structures differing from the equilibrium phase. The order of precipitation typically follows the sequence (Tiryakioğlu and Staley, 2003):

Supersaturated solid solution → independent and co-clusters of Mg and Si

→ GP zones → Si rich phase → β'' → β' → β (Mg_2Si)

The GP zones and β'' precipitates have a needle-like shape and form along the $\langle 100 \rangle$ direction of the aluminum matrix. Due to their small size and coherency with the matrix, they are easily sheared by dislocations leading to strain localization. The β' transition phase has a rod-shaped morphology and a hexagonal crystal structure with the $\{001\}$ planes and $\langle 100 \rangle$ directions parallel to the $\{100\}$ planes and $\langle 011 \rangle$ directions of the aluminum matrix as shown in Figure 2.4. They are non-shearable precipitates and increase strength by Orowan looping. The equilibrium β phase has a face centered cubic structure and forms as non-coherent platelets on the matrix $\{100\}$ planes with minor contributions to the alloy strength (Starke, 1989).

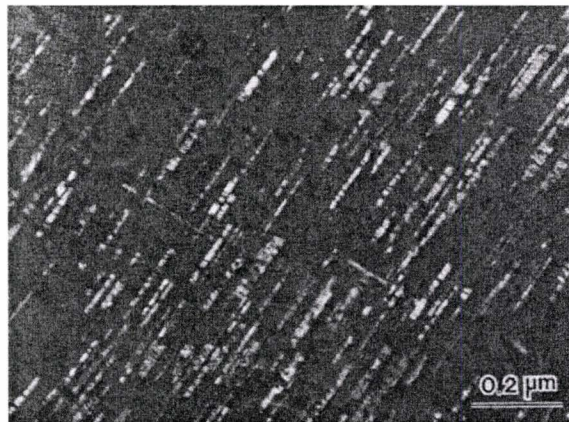
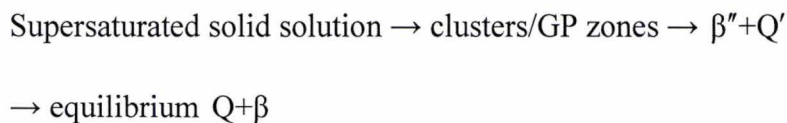


Figure 2.4: Dark field TEM micrograph of non-shearable rod-shaped β' precipitates following 4% tensile strain showing fringes due to Orowan looping. (Starke, 1989)

The as-cast structures of AA6xxx alloys also contain plate-like Mg-Si particles. These particles are either precipitated as β - Mg_2Si on the boundaries of the Fe containing

intermetallics, as isolated particles on the boundaries of the aluminum dendrites or as smaller β' Mg-Si precipitates in the matrix (Kuijpers et al., 2002). The dissolution of the β -Mg₂Si takes place during the homogenization of as-cast structures of AA6xxx alloys, and was found to be indirectly influenced by the concentration of iron in the alloy. Moreover, Kuijpers et al. (2002) have shown that less β'' and β' Mg-Si particles are precipitated with the increase in iron content due to a decrease in the Si solute levels already consumed in the Fe-containing particles.

The addition of copper to the 6xxx series of Al-Mg-Si alloys results in the formation of the Q phase with a complex aging response due to the formation of many intermediate phases. The precipitation sequence in Cu-containing Al-Mg-Si alloys has been extensively studied in recent years and there has been a general consensus that the reaction proceeds according to the following order (Lloyd et al., 2000; Esmaeili et al., 2003):



The major difference in the above sequence from the Cu-free alloys is the presence of the quaternary Q phase and its metastable precursor Q' (Perovic et al., 1999). The Q phase has several reported compositions such as Al₄Cu₂Mg₈Si₇, Al₅Cu₂Mg₈Si₆ and Al₄CuMg₅Si₄ with either an orthorhombic or hexagonal crystal structure (Matsuda et al., 2001). Its precursor phase Q' has a lath morphology that distinguishes it from the β'

precipitates as both phases have their long dimensions parallel to the $\langle 100 \rangle$ directions of the aluminum matrix. Figure 2.5 shows the morphology of the Q' precipitates. Wang et al. (2006) also reported a polygonal-based morphology of the Q phase. Although, the Q' phase is present in peak aged conditions of Al-Mg-Si-Cu alloys, the β'' phase remains the dominant intermediate strengthening phase (Esmaili et al., 2003). However, the Q' phase still has an appreciable strengthening effect due to its fine size and steady increase in volume fraction during aging (Tiryakioğlu and Staley, 2003). Recently, a new fully coherent metastable precursor of the Q phase was identified by Wang et al. (2006). The authors named this phase Q'' and suggested the following modification to the precipitation sequence for the Al-Mg-Si-Cu alloys:

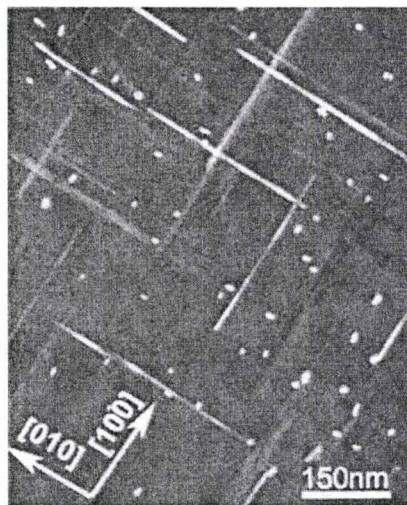
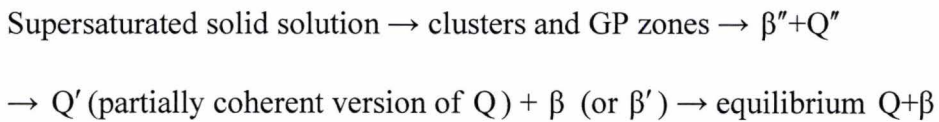


Figure 2.5: Dark field TEM micrographs of Q' precipitates. (Wang et al., 2006)

The precipitation kinetics for the 6xxx alloys was found to be dependent on the level of cold work prior to annealing (Quainoo et al., 2001; Quainoo and Yannacopoulos, 2004). The β'' precipitation shifts to lower temperatures with the increase in prestrain levels. This results from the increased dislocation density which enhances the aging response of the material by rapid nucleation of precipitates. The increased dislocation densities are also responsible for the disappearance of some precipitation events at higher prestrain levels. Enhanced precipitation kinetics of Al-Mg-Si alloys due to increased defect concentrations was also observed by Zhen et al. (1997). The authors attributed such effect to the rapid diffusion of silicon along dislocations in comparison with the bulk diffusion. The precipitation and dissolution events in an AA6111 alloy are also affected by preaging treatments. The activation energies for cluster dissolution and β'' precipitation were higher in preaged material than naturally aged ones (Bryant, 1999). The shifting of β'' precipitation events to higher temperatures was also observed by Esmaili et al. (2003) for naturally aged material. The authors attributed the effect to the slow dissolution of clusters existing from the prior aging treatments and their role in decreasing the rate of nucleation of the β'' precipitates. Miao and Laughlin (2000) reported an increased stability of the clusters or GP zones formed during preaging treatments.

Apart from the major alloying elements Mg and Si, Fe is always present in the 6xxx series alloys either as an impurity or as an alloying addition. Due to the low solubility of iron in aluminum, Fe will bind to the excess silicon or manganese and abundant aluminum to form Fe-containing intermetallics with a typical volume fraction

of one percent. Most of these intermetallics are the monoclinic β -AlFeSi phase with a plate like morphology and an approximate stoichiometry of Al_5FeSi with no presence of Mn (Kuijpers et al., 2002). Such particles are known to form a continuous network along the grain boundaries and are associated with stress fields due to their sharp boundary with the aluminum matrix (Claves et al., 2002). Other small fractions of the cubic α -Al(Fe,Mn)Si phase can also be present in the as-cast structure with a morphology known as the Chinese-script. Such particles have an approximate size of $5\ \mu\text{m}$ and a high Fe/Mn ratio. This phase can also be found as dispersoids having sizes ranging from 50-200 nm formed during the homogenization of alloys with high Mn content. They usually have a low Fe/Mn ratio and a stoichiometry approximately equal to α_c - $\text{Al}_{12}\text{Mn}_3\text{Si}$. Another phase that is rarely encountered in 6xxx series Al alloys is the hexagonal α_h phase with a stoichiometry of $\text{Al}_8\text{Fe}_2\text{Si}$. However, this phase is only encountered with low Mn concentrations (approx 0.01 wt.%) as higher concentrations will lead to the stabilization of the cubic α_c phase. During the homogenization of as-cast Al-Mg-Si alloys, a phase transformation is known to occur upon which the single plate-like β - Al_5FeSi particles are transformed to multiple more rounded coarse α -AlFeMnSi particles with an average size of $1\ \mu\text{m}$ (Kuijpers et al., 2002; Claves et al., 2002). Such transformation is known to enhance the ductility and the surface quality of the final material during aluminum extrusion processes. Table 2.1 shows the most common structural variance of these phases. Such intermetallic particles are considerably stable and do not dissolve during solutionizing or aging treatments.

Table 2.1: Structural variance of common intermetallic phases in 6xxx Al alloys (Claves et al., 2002)

Notation	Stoichiometry	Bravais Lattice	Space Group	Lattice Parameters	Density kg/m ³
β	Al _{4.5} FeSi Al ₅ FeSi	Monoclinic	A 2/a	a = 6.12 Å b = 6.12 Å c = 41.5 Å $\beta = 91^\circ$	3300- 3350
α_h	Al ₈ Fe ₂ Si	Hexagonal	P6 ₃	a = b = 12.3 Å c = 26.2 Å	3580
α_c	Al ₁₂ Fe ₃ Si Al ₁₂₋₁₅ Fe ₃ Si ₁₋₂	Cubic	Im ₃	a = 12.56 Å	3640
	Al ₁₂ (FeMn) ₃ Si Al ₁₅ (FeMn) ₃ Si ₂	Cubic	Im ₃ – Pm ₃	a = 12.56 – 12.68 Å	3630 - 3640
	Al ₁₂ Mn ₃ Si Al ₁₅ Mn ₃ Si ₂ Al ₉ Mn ₂ Si	Cubic	Pm ₃	a = 12.68 Å	3630

2.4.2 Recrystallization Kinetics in Al-Mg-Si Automotive Alloys

During the thermomechanical processing of heat-treatable aluminum alloys, the volume fraction of dispersoids is usually insufficient to prevent recrystallization and a higher pinning pressure on the deformed substructure and the grain boundaries is exerted by the higher volume fraction of the less stable age hardening phases (Lillywhite et al., 2000). Paillard and Humphreys (1996) employed different heat treatments to Al-4%Cu

alloys to obtain different particle distributions in the matrix. The examined particle dispersions included large stable particles, large unstable particles and a bimodal particle distribution. On annealing of these samples at 300 °C, recrystallization originated at the large second phase particles in all the samples and the resulting annealing textures were weak showing that prior heat treatments had no effects on the texture components. However, the recrystallization kinetics and the resulting microstructures were dependent on the prior heat treatments. The recrystallization kinetics for the large stable particles was much faster than the other particle dispersions, and the resulting microstructure had smaller grain sizes. The delay in the recrystallization time for the other unstable and bimodal particle dispersions was attributed to the Zener drag exerted by the small particles precipitating during annealing or preexisting in the matrix.

Burger et al. (1996) examined the development of microstructure and the softening behavior occurring during the recovery and recrystallization stages of an AA6111 sheet alloy. The annealing process was simulated using electrical resistance heating at a rate of 20 °C/s. Their results indicated a start of recrystallization at 390 °C with large Fe-based constituent particles acting as nucleation sites for small recrystallized grains. The recrystallization process occurred rapidly within the temperature interval 400-420 °C with the fully recrystallized structure attained at 430 °C. Evidence of grain boundary pinning by the fine distribution of the Q phase along the boundaries was also shown to occur when comparing the grain structures obtained at 430 °C to that for

material recrystallized in heating at 560 °C where the dissolution of the phase had occurred. The Q phase restrained the development of a stable grain morphology.

The effect of initial precipitation states on the recrystallization kinetics of the same AA6111 alloy during annealing was also investigated by Go et al. (2003). Their emphasis was on the effect of the unstable hardening phases on the process. The samples investigated were aged to the naturally (T4), artificially (T6) and the overaged conditions. They were then cold rolled to a reduction of 40% followed by annealing at 325 °C. The results of tensile tests performed on the samples are shown in Figure 2.6 and reveal a considerable level of softening without any indicative point related to the onset of recrystallization. The microstructures revealed a partially recrystallized grain structure of approximately 20-30% in the T4 and T6 samples, but with a more uniform distribution of grains in the T4 sample over the T6 sample. This retardation of recrystallization was attributed to the presence of the Q' phase especially at the elongated grain boundaries. As the annealing time was increased, coarsening of precipitates took place resulting in a decrease in the yield stress and thus, further softening. On the other hand, the overaged sample showed no signs of recrystallization and the grain structure remained elongated in the rolling direction. This severe retardation effect is due to the presence of the relatively coarse Q' precipitates and their possible fracture during cold work thus, increasing the density of the second phase particles present in the microstructure. Another factor affecting the rate of recrystallization was the reduction in the driving pressure resulting from the large amount of recovery taking place prior to the start of recrystallization. The

authors suggested that the onset of recrystallization during annealing is controlled by the coarsening of precipitates.

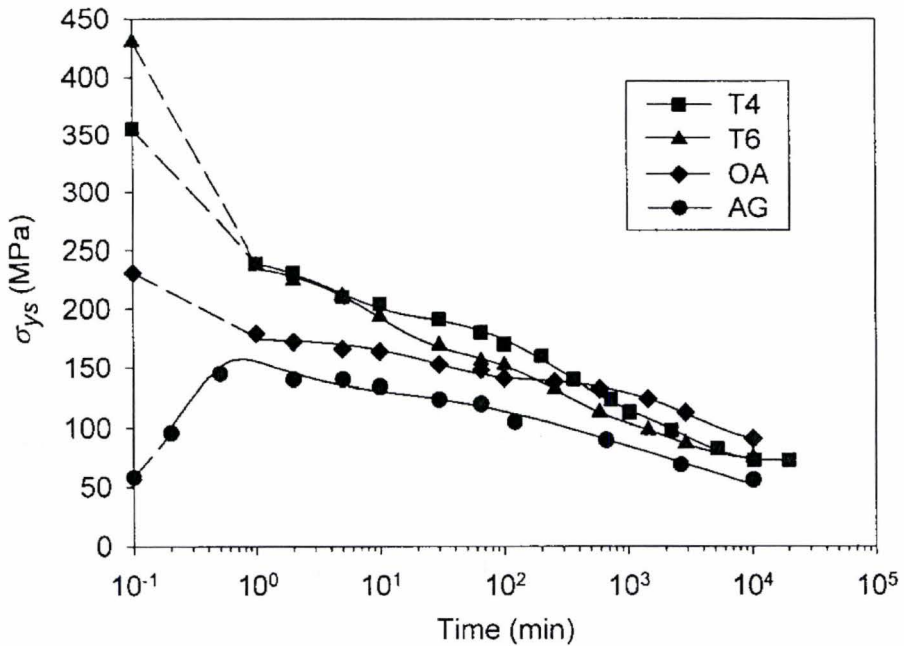


Figure 2.6: Yield stress evolution for the 40% cold rolled AA6111 annealed at 325 °C with different precipitation conditions (T4: naturally aged, T6: peak aged, OA:overaged) and for the solution treated material aged at 325 °C (AG). The data points at a time of 10^{-1} min represent the as-deformed or as solution treated yield stresses. (Go et al., 2003)

Lillywhite et al. (2000) also studied the interactions between precipitation and recrystallization in an Al-0.77Mg-0.5Si-0.2Fe alloy under different starting microstructures. The employed thermal treatments together with the corresponding time for complete recrystallization and the resulting grain size during isothermal anneals at 300 °C are summarized in Table 2.2. Before annealing, the samples were cold rolled to 70% reductions. From the table, it is clear that the recrystallization rate for the furnace cooled sample was quite rapid achieving total completion after 10 min. The initial pre-

deformation microstructure for such sample contained mainly coarse equilibrium Mg_2Si phases ($\approx 20 \mu m$) with a volume fraction of about 1.2% hence, leaving no excess Mg and Si solute to precipitate on annealing. These large spherical β particles only suffered minor break ups during rolling and hence, promoted recrystallization through particle-stimulated nucleation during subsequent annealing. As for the solution treated sample, recrystallization was shown to initiate after 1 h and took about 10 h to reach completion.

Table 2.2: Heat treatments, recrystallization time and the resultant grain sizes for the samples isothermally annealed at 300 °C

Initial heat treatment	Initial particle content	Recrystallization time		Final grain size
		Initiation	Completion	
Solution treated 550 °C (2 h) and water quenched	Supersaturated solid solution	1h	10 h	25 μm
Solution treated 550 °C (2 h), water quenched and annealed before deformation at 300 °C for times ranging from 0.5-50 h	Metastable β' rods (length = 0.5 μm)	>300 h	1600 h	70 μm
Solution treated 550 °C (2 h), furnace cooled to 300 °C and water quenched	Stable β spheres (diameter = 20 μm)	1 min	10 min	30 μm

This slower recrystallization rate in comparison to the furnace cooled sample relates to the initial microstructure. Before the initiation of recrystallization during annealing, high densities of β' rods had already nucleated heterogeneously exerting a pinning pressure on the substructure. Large β particles had also precipitated on the Al(Fe,Si) particles. With the increase in the annealing time, the metastable β' rods start to dissolve resulting in the formation of precipitate free zones around the β particles. Recrystallization then initiates by subgrain coarsening within these precipitate free zones. However, the new grain sizes were restricted to those of the precipitate free zones. Therefore, the recrystallization rate was slower than the case for the furnace cooled samples although both shared a particle-stimulated nucleation mechanism for the initiation of recrystallization. By further increasing the annealing times the new grains grow out of the precipitate free zones as shown in Figure 2.7 due to two opposing pressures; the forward pressure exerted by the subgrain boundaries to consume the recovered microstructure and the pinning pressure exerted by the particles.

On the other hand, the preaged samples showed the slowest recrystallization kinetics. This is attributed to the high density of fine particles present in the grains of the samples before rolling and their subsequent fragmentation during deformation giving rise to a greatly refined distribution of the β precipitates in the early annealing stages. This fine distribution of stable β particles hinders the nuclei formation and results in delayed initiation of recrystallization. However, the nucleation mechanism was still similar to that

for the solution treated samples where it occurred from the growth of coarse subgrains in the precipitate free zones surrounding large β particles. The long recrystallization time results from the increased time required by the stable particles to coarsen and thus decrease the pinning pressure exerted on the recrystallization front. Increasing the preaging time will increase the rate of recrystallization due to the reduction in the particle density and the increased width of the precipitate free zones surrounding the coarse particles.

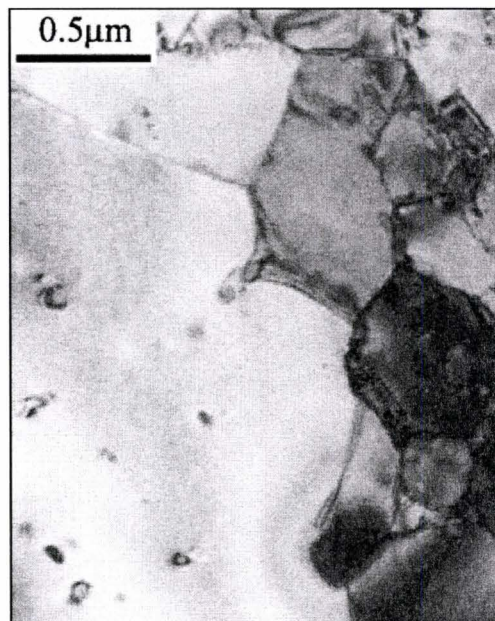


Figure 2.7: TEM micrograph showing the recrystallization front with heterogeneous migration. (Lillywhite et al., 2000)

Lillywhite et al. (2000) proposed two grain boundary migration mechanisms. The first is controlled by the transformation of the metastable β' phase to the equilibrium β phase at the grain boundary and occurs in the solution treated samples. In this

mechanism, the boundary is pinned by the high density of metastable rod shaped β' precipitates as shown in Figure 2.8. However, these precipitates are shorter than the remaining rods ahead of the boundary thus implying that they are dissolving. Hence, an equilibrium β precipitate starts nucleating on the boundary and grows by consuming the metastable β' particles. The pinning pressure is reduced as the precipitate coarsening continues and the boundary migrates until it is pinned again by the next set of β' precipitates. The other boundary migration mechanism is controlled by the coarsening of the equilibrium β particles at the recrystallization front and occurs in the preaged alloys. Particles pinning the boundary will coarsen reducing the pinning pressure and allowing the boundary to move forward until it is stalled by another set of precipitates. This mechanism is much slower than the above phase transformation controlled boundary migration due to the low driving force for coarsening processes.

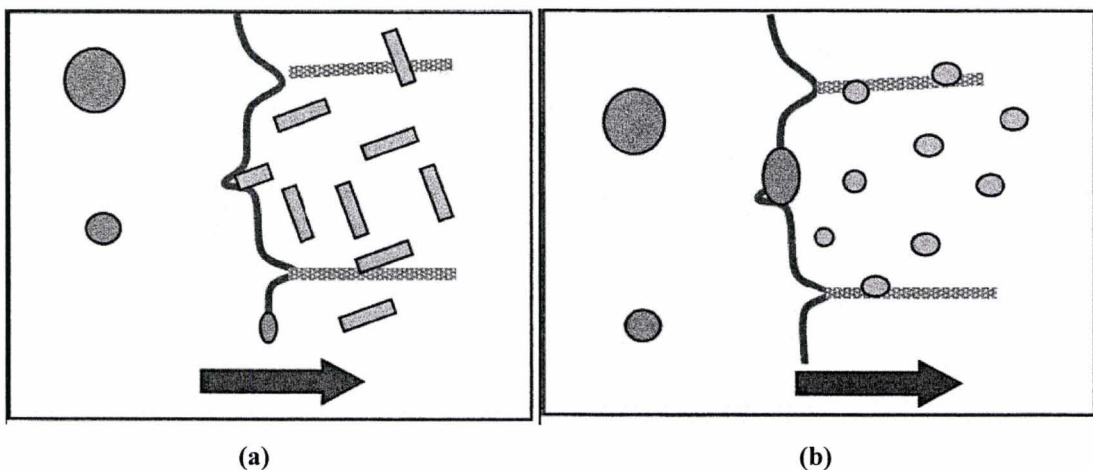


Figure 2.8: Schematic representation of the grain boundary migration mechanisms: a) controlled by the phase transformation of β' to β phase and b) controlled by coarsening of β particles. (Lillywhite et al., 2000)

CHAPTER 3

Phase Equilibria in Al–Mg–Si–Cu Alloys

Second-phase particles present in a majority of aluminum alloys influence both the microstructure and the mechanical properties of final products. Since precipitation hardening is the major strengthening mechanism of heat-treatable aluminum alloys, processes of new phase formation in solutionized and then quenched alloys gained much attention. In addition to phases completely dissolving in the FCC matrix during the solutionizing heat-treatment and forming again in the course of artificial or natural aging, the alloys also include other kind of phases usually containing significant amounts of iron, manganese and silicon. These phases are so thermodynamically stable that their existence is virtually unaffected by the solutionizing treatment (Brooks, 1997).

Although these “everexisting” phases do not contribute to the precipitation hardening, they affect recrystallization of deformed alloys. Due to high dislocation densities generated at the interface of large particles and their associated deformation zones, new grains may nucleate in their vicinity. Small particles, on the other hand, may pin boundaries of growing grains resulting in a finer grain structure and thus in a stronger material (Hornbogen and Köster, 1978; Humphreys and Hatherly, 1995). Therefore, in order to enhance the mechanical properties of heat-treatable aluminum alloys,

considerations regarding the nature of these thermodynamically stable phases, their volume fraction, aspect ratio and size distribution have to be accounted for. For the sake of brevity, these thermodynamically stable phases will be referred as “intermetallics” or “intermetallic phases” through this work. The following investigation is focused on the characterization of intermetallic phases in the Al-Mg-Si-Mn-Fe-Cu system together with an assessment of their thermodynamic characteristics within the framework of the CALPHAD method.

3.1 Thermodynamic Estimations

A sheet of strip-cast AA6111 alloy with a gauge of 16 mm was supplied by Novelis. The composition of the alloy is specified in Table 3.1.

Table 3.1: Chemical composition of the alloy investigated in wt.%

Mg	Fe	Si	Mn	Cu	Al
0.55	0.34	0.56	0.25	0.2	balance

The fabrication of strip-cast alloys is characterized by high cooling rates causing a significant supercooling of the melt. From this angle, it can be anticipated that the processes of phase formation in a solidifying material are not solely governed by thermodynamics. In particular, it can be expected that the as-cast alloy would contain metastable phases whose formation is kinetically favorable. Notwithstanding this general argument, the Scheil formalism (no diffusion in the solid state, no concentration gradients

in the liquid phase, local equilibrium at the solid/liquid interface) was applied to the analysis of solidification. A list of phases existing in the Al-Mg-Fe-Si-Mn-Cu system and their thermodynamic properties were adopted from the Thermochemical database for light metal alloys, which, for brevity, will be referred to as COST-507 database. Results of calculations shown in Figure 3.1 and Figure 3.2 were performed by using ThermoCalc and correspond to the accumulated amounts of intermetallics in the alloy during casting and the variation of the equilibrium amount of phases with temperature, respectively. Sublattice models attributed to the phases in the COST-507 database are shown in Table 3.2.

Table 3.2: Sublattice models of phases

Phase name	Sublattice model
$Al_{13} M_4$	$Al_{0.6275} (Fe, Mn)_{0.235} (Al, Si, Va)_{0.1375}$
$\alpha - AlMnSi$	$Al_{16} Mn_4 Si (Al, Si)_2$
$\alpha - AlFeSi$	$Al_{0.6612} Fe_{0.19} Si_{0.0496} (Al, Si)_{0.0992}$
$\beta - AlFeSi$	$Al_{14} Fe_3 Si_3$

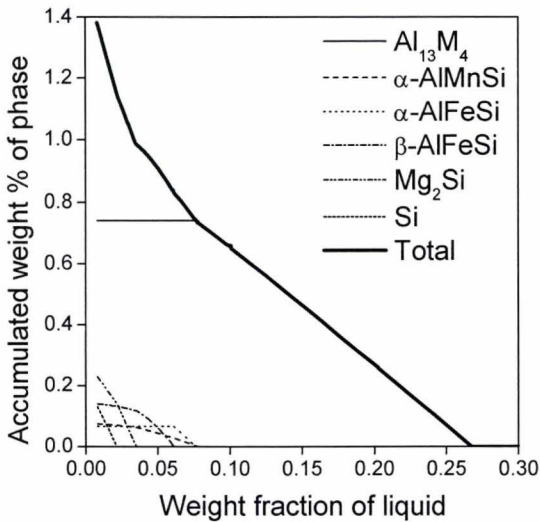


Figure 3.1: Amounts of intermetallics accumulating in the alloy during casting.

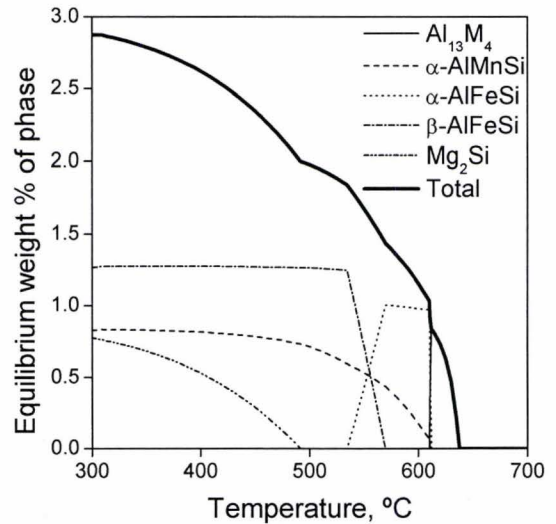


Figure 3.2: Equilibrium amounts of intermetallics.

The calculations offer two conclusions. Firstly, Al_{13}M_4 (sometimes designated as Al_3M) is the dominant intermetallic constituting more than 50% of the total amount of all intermetallic phases. Secondly, the overall amount of intermetallics does not exceed 1.5 wt.%. It is worth noticing that although the alloy investigated contains 0.2 wt.% of copper, there are no Cu-containing phases in Figure 3.1 and Figure 3.2. The reason for this “contradiction” is that during solidification copper is accumulated in the FCC phase. An absence or a presence of Cu-containing intermetallics in the as-cast structure depends on how much copper an alloy contains. A comparison of Figure 3.3 and Figure 3.4 indicates that it is not a mere increase of the copper content in the liquid and FCC phases but the magnitude of this rise, which triggers the formation of Cu-containing phases.

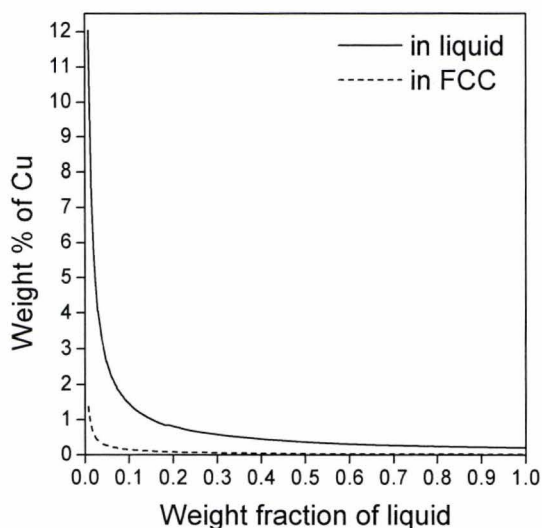


Figure 3.3: Accumulation of Cu in the FCC phase for the alloy with the composition given in Table 3.1.

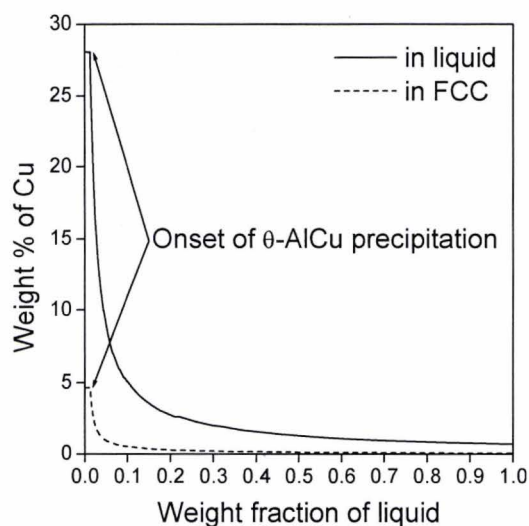


Figure 3.4: Accumulation of Cu in the FCC phase for the alloy in which the Cu content was changed from 0.2 to 0.7 wt.%. Onset of θ -AlCu precipitation

The amounts of different phases at the end of solidification should not be identified with their equilibrium amounts delineated in Figure 3.2. This figure suggests that a total amount of intermetallic phases in the AA6111 alloy strongly depends on temperature, and that temperature has a pronounced effect upon the nature of phases existing in the alloy. In particular, at 450°C, the presence of β -AlFeSi, α -AlMnSi and Mg_2Si is expected; at 600°C, the equilibrium phases are α -AlFeSi and α -AlMnSi. The total amount of intermetallics at 450°C is almost two times greater than that at 600°C.

3.2 Experiment

3.2.1 Materials

In addition to the as-cast alloy with the composition shown in Table 3.1, two heat-treated specimens were fabricated. The first sample was held at 450°C for 1 week; the second sample was annealed at 600°C for 2 days. After that, the specimens were quenched in cold water. The heat-treatment was carried out in a protective Ar atmosphere. An absence of oxidation was verified by weighing the samples before and after the heat-treatment. Temperatures to which the alloy was exposed were prompted by the thermodynamic evaluations summarized in Figure 3.2. Times chosen were significantly longer than that recommended by ASM standards and normally employed in industry. The prolonged heat-treatment was employed for ensuring that the material attained equilibrium.

3.2.2 Phase Characterization

The intermetallic phases were extracted from the alloy by using the boiling phenol technique outlined by Gupta et al. (1996). Phenol dissolves the FCC phase according to the reaction $3\text{C}_6\text{H}_5\text{OH} + 2\text{Al} \rightarrow 2\text{Al}(\text{C}_6\text{H}_5\text{O})_3 + 3\text{H}_2$ without affecting other phases embedded in the matrix. After the dissolution is complete, a mixture of benzylalcohol and toluene is added to the flask where the reaction took place and its content is centrifuged and then decanted. These centrifuging-cleaning cycles are repeated several times. Finally, the particles are rinsed with anhydrous ethanol, centrifuged and dried in air at 120°C. The

final product of these manipulations is a grayish powder composed of small particles whose appearance is illustrated by Figure 3.5. The nature of the powder was then investigated by X-ray powder diffraction (XRD) and inductively coupled plasma mass spectrometry (ICP).

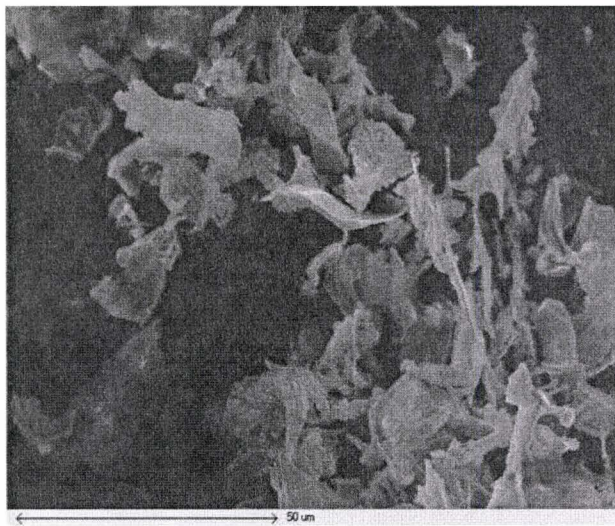
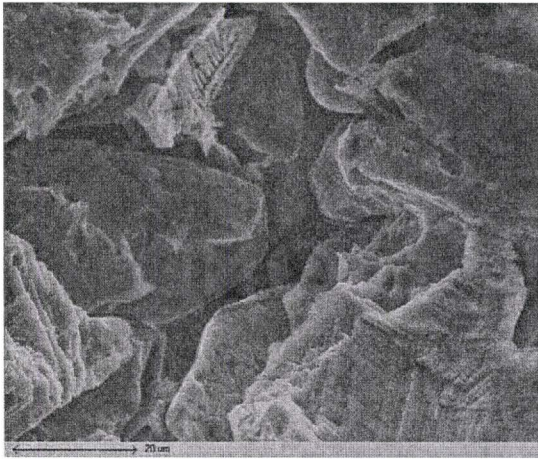


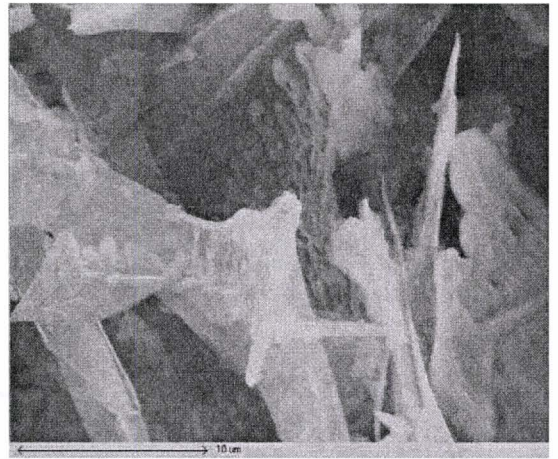
Figure 3.5: Intermetallic particles extracted from the as-cast alloy.

In addition to a complete dissolution of alloys, an incremental dissolution of an as-cast specimen was performed. By placing the sample in boiling phenol for a certain time, it was possible to remove an outer portion of material. After that, the surface was rinsed with a mixture of benzylalcohol and toluene, dried and examined by SEM. By using this technique, which was essentially a deep etching, it was possible to compare appearances and compositions of intermetallics in various locations within the specimen. Although these locations were likely characterized by different cooling rates and supercoolings attained during casting, the differences were not reflected in the shape and

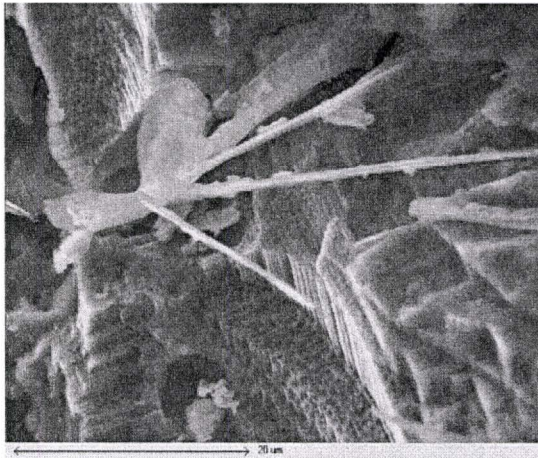
composition of second-phase particles. SEM images of such phases appearing in a deeply etched AA6111 alloy are shown in Figure 3.6.



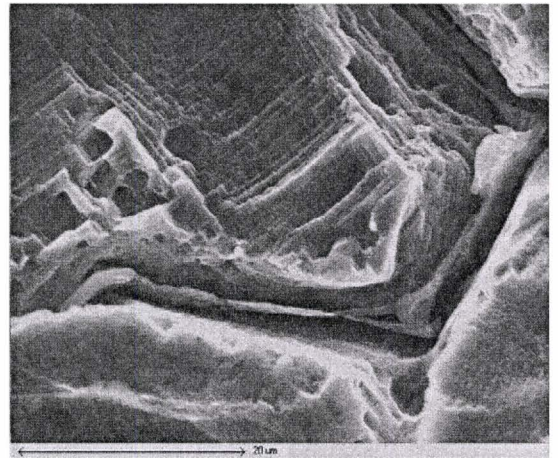
Scripts



Leaves



Rods



Sheets

Figure 3.6: Morphologies of thermodynamically stable phases.

3.3 Results and Discussion

3.3.1 Characterization of Intermetallic Phases

Weight percents of intermetallic phases found in as-cast and heat-treated samples are presented in Table 3.3.

Table 3.3: Experimentally determined weight % of intermetallic phases

Alloy	Measurement	Weight of alloy, g	Weight of intermetallics, g	Weight % of intermetallics
As-cast	1	2.860	0.066	2.3
	2	2.375	0.062	2.6
Heat-treated at 450°C for 1 week	1	3.145	0.086	2.7
	2	2.989	0.068	2.3
Heat-treated at 600°C for 2 days	1	2.771	0.054	1.9
	2	2.983	0.067	2.2

It should be accentuated that the values in the last column of Table 3.3 represent a lower limit of the amounts of intermetallics in the alloys. The reason is self-evident: particles (especially small ones) can only be lost during numerous centrifuging/decanting cycles. For instance, it can be taken for granted that the alloy heat-treated at 450°C for one week contains at least 2.7 weight % of intermetallic phases. By matching this value against the bold curve in Figure 3.2, it can be concluded that the heat-treated alloy contains more intermetallics than that predicted from the thermodynamic estimations. The same can be

said about the alloy subject to heat-treatment at 600°C for 2 days, for which the discrepancy is huge. The minimal amount of intermetallics is pronouncedly greater than 1.4 wt.% which was the maximal quantity suggested by Figure 3.2. This is the first contradiction seen when the experimental observations are compared with the thermodynamic predictions.

The second contradiction was encountered when the nature of the intermetallic phases was examined by means of XRD. It can be seen in Figure 3.7 that the three spectra are similar despite the fact that the intermetallics were extracted from alloys having different thermal histories and – according to Figure 3.1 and Figure 3.2 – different phase portraits.

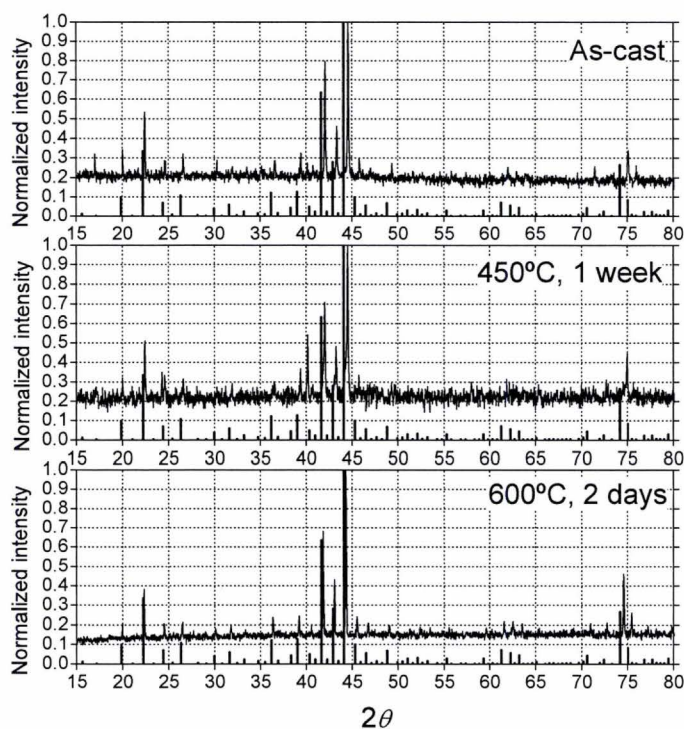


Figure 3.7: XRD spectra of intermetallic particles.

The locations and intensities of the peaks indicate that the dominant phase is the cubic quaternary phase containing aluminum, iron, manganese and silicon. This phase was discovered by Phragmen (1950) who assigned it the formula $\text{Al}_{12}(\text{Fe},\text{Mn})_3\text{Si}$. Barlock and Mondolfo (1975) suggested that the composition of this phase was $\text{Al}_{15}(\text{Fe},\text{Mn})_3\text{Si}_2$ and found that as much as 90% of Mn can be substituted by Fe on the corresponding sublattice. This phase and equilibria it participates in were extensively explored by Zakharov et al. (1988 & 1989) and was assigned the stoichiometry $\text{Al}_{16}(\text{Fe},\text{Mn})_4\text{Si}_3$. Due to this reason, this quaternary phase will be referred to as the ζ -phase from here on.

The phase $\text{Al}_{16}\text{Mn}_4\text{Si}(\text{Al},\text{Si})_2$ included in the COST-507 database and sometimes referred as the “ α -phase” in literature, has the stoichiometry suggesting that the ζ -phase is nothing but a particular case of the α -phase with iron dissolved in the second sublattice and silicon as the only constituent on the last sublattice. It should be highlighted that α and ζ are two different phases having the same structure but noticeably different lattice parameters. Besides, it is a well-established fact that the α -phase is incapable of dissolving significant amounts of iron, *i.e.* that the maximal iron content in the α -phase is much lesser than that experimentally seen in the ζ -phase as indicated by Mondolfo (1975) and Zakharov et al. (1988 & 1989).

The results of the ICP analysis conducted on the residue of intermetallics extracted from the samples heat-treated at 600°C for 2 days confirmed the previous stoichiometry of the ζ -phase as shown in Table 3.4. The higher than expected ratios of Al/(Fe,Mn) and Al/Si could be attributed to the presence of Al-rich phases such as Al_6M and/or Al_{12}M .

Table 3.4: Elemental ratios for intermetallics extracted from the heat-treated alloy

Alloy	Measurement	Al/(Fe,Mn)	Al/Si	(Fe,Mn)/Si	Fe/Mn
Heat-treated at 600°C for 2 days	1	5.53	6.01	1.09	1.87
	2	5.27	5.48	1.04	1.89
	3	4.64	5.53	1.19	1.55

3.3.2 Thermodynamics of the ζ -phase

It can be hoped that the aforementioned contradictions between the thermodynamic predictions and the experimental observations can be settled if the thermodynamic properties of the quaternary ζ -phase are added to the COST-507 database. It can be anticipated that calculations carried out with an amended database will result in diagrams different from those shown in Figure 3.1 and Figure 3.2.

Balitchev et al. (2003) assumed that the ζ -phase is a stoichiometric compound having the formula $Al_{16}Fe_{1.7}Mn_{2.3}Si_3$ and assessed its thermodynamic properties by using data on the temperatures of invariant equilibria and liquidus temperatures reported by Zakharov et al. (1988 & 1989). The following expression was proposed for the Gibbs energy of the ζ -phase:

$${}^0G^\zeta = 16{}^0G_{Al}^{fcc-A1} + 1.7{}^0G_{Fe}^{bcc-A2} + 2.3{}^0G_{Mn}^{hcp-A3} + 3{}^0G_{Si}^{diamond-A2} - 483030.78 + 71.0T \quad (3.1)$$

The results of calculations carried out with the modified COST-507 database are presented in Figure 3.8 and Figure 3.9.

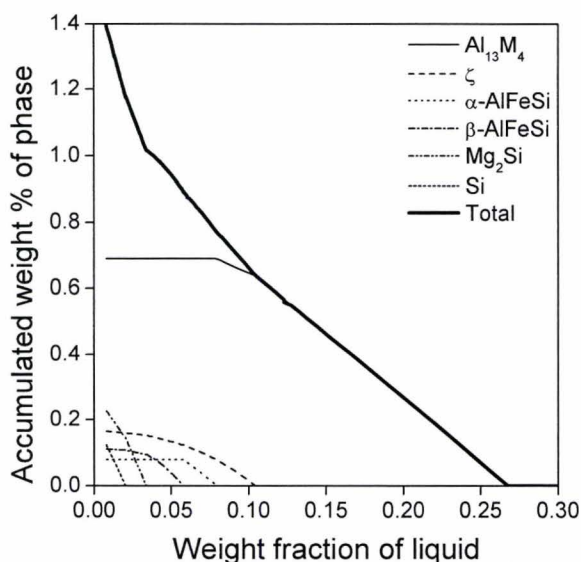


Figure 3.8: Amounts of intermetallics accumulating in the alloy during casting.

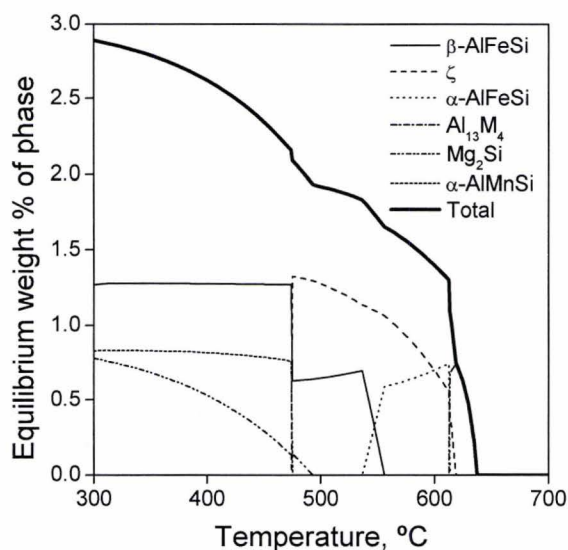


Figure 3.9: Equilibrium amounts of intermetallics.

A comparison of these diagrams with the diagrams shown in Figure 3.1 and Figure 3.2 stipulates that the addition of the ζ -phase to the database brings noticeable changes to the phase portrait of the alloy. For instance, according to Figure 3.8, α -AlMnSi is no longer forming during solidification. It is worth noticing that if the AA6111 alloy is subject to heat-treatment, the ζ -phase is expected to be the dominant phase between 480 and 600°C coexisting with β -AlFeSi and α -AlFeSi. The most important conclusion that can be drawn from Figure 3.8 and Figure 3.9 is that the thermodynamic predictions based on the amended database are still at odds with the experimentally gained evidences that whatever the thermal history of the alloy, the ζ -phase dominates, and that the overall content of intermetallic phases exceeds 2 wt.%. A hypothetical explanation of this contradiction is that the thermodynamic stability of the ζ -phase was underestimated in the

assessment by Balitchev et al. (2003), which was based exclusively on phase diagram related data without invoking any thermodynamic quantities. Hence, an attempt to decrease the Gibbs energy of the ζ -phase and analyze how such an alteration is translated into the amount of intermetallics was carried out. For the sake of determinacy, 5 and 10 kJ per formula unit were subtracted from the Gibbs energy of the ζ -phase. The accumulated amounts of $\text{Al}_{16}\text{Fe}_{1.7}\text{Mn}_{2.3}\text{Si}_3$ as well as all intermetallics computed with these biased Gibbs energies are presented in Figure 3.10.

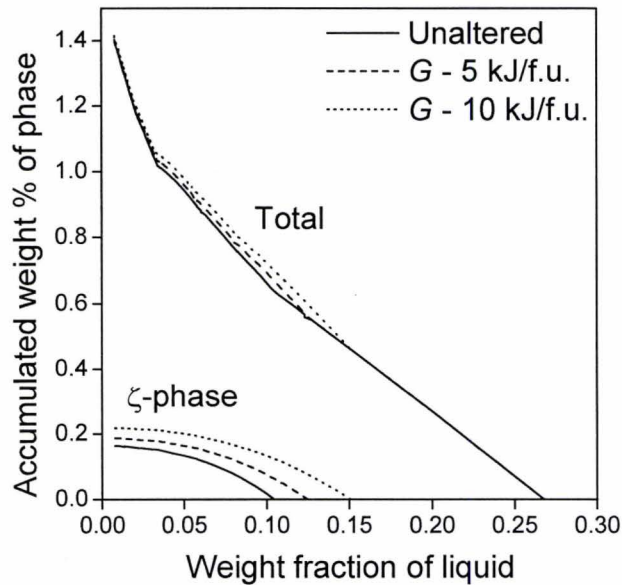


Figure 3.10: Influence of decreased Gibbs energies on the contents of the ζ -phase and all intermetallics.

It can be seen that the artificial stabilization noticeably raises the fraction of the ζ -phase in the as-cast alloy, but the magnitude of the increase still does not conform to experimental findings. Even though the magnitude was sufficiently large, it would be

nothing but a scholastic numerical exercise since, firstly, one is not supposed to arbitrarily bias the Gibbs energy resulting from an optimization procedure. Secondly, a forcefully changed Gibbs energy will likely result in isothermal and isoplethal sections contradicting those reported by Zakharov et al. (1988 & 1989). Therefore, another justifiable way of making the ζ -phase more stable is needed.

It is important to note that Balitchev et al. (2003) treated this phase as a stoichiometric compound $\text{Al}_{16}\text{Fe}_{1.7}\text{Mn}_{2.3}\text{Si}_3$. This stoichiometry corresponds to the average composition of the ζ -phase found by Zakharov et al. (1989) despite the reported varying composition of this quaternary phase. Weight % of iron and manganese varied from 10.4 to 15.3 and from 14.6 to 19.7, correspondingly. The compositional variations are in accordance with the fact that in many intermetallic phases, Fe and Mn easily substitute each other on the same sublattice. It is worth reminding that a very wide homogeneity range in terms of the Fe to Mn ratio was reported by Barlock and Mondolfo (1975), while ratios of Fe/Mn of 1.6 to 1.9 were identified by ICP analysis in this work as shown in Table 3.4. Based on these evidences, the sublattice model $\text{Al}_{16}(\text{Fe}_y, \text{Mn}_{1-y})_4\text{Si}_3$ was chosen for the ζ -phase. In this case, an entropic term $4RT(y \ln y + (1-y) \ln(1-y))$ appears in the analytical description for the Gibbs energy. Quantitatively, the presence of this term for the composition $\text{Al}_{16}(\text{Fe}_{1.7/4}, \text{Mn}_{2.3/4})_4\text{Si}_3$ brings approximately -17.5 and -19.8 kJ per formula unit at 500 and 600°C, correspondingly. It should not be forgotten, however, that the modification of the model adopted for the ζ -phase by Balitchev et al. (2003) requires that at least the terms ${}^0G_{\text{Al:Fe:Si}}$ and ${}^0G_{\text{Al:Mn:Si}}$ are to be assessed. Since the

excess terms ${}^iL_{\text{Al:Fe,Mn:Si}}$ cannot be ruled out, a full-fledged re-determination of the thermodynamic properties of the $\text{Al}_{16}(\text{Fe,Mn})_4\text{Si}_3$ phase is required.

3.4 Re-assessment of the Thermodynamic Properties of the ζ -phase

In addition to the new phase model for the ζ -phase, there is another motive suggesting the re-optimization of the properties of this phase. The motivation is that the analytical description (3.1) proposed by Balitchev et al. (2003) does not always result in a reasonable agreement with the experimental data. The authors illustrated a passable quality of their assessment on several examples. For instance, the experimental isoplethal sections 3 wt.% Fe and 10 wt.% Si were accurately reproduced. However, by inspecting Figure 3.11 and Figure 3.12, in which the experimentally found locations of phase boundaries are confronted with those calculated by using the thermodynamic information from Zakharov et al. (1989). It is clearly seen that for some boundaries, deviations between the measured and computed temperatures are substantial. The discrepancies are especially large for the phase boundary separating Liquid + ζ and Liquid + ζ + α AlMnSi phase regions. The re-optimization was launched with an intention to diminish these digressions.

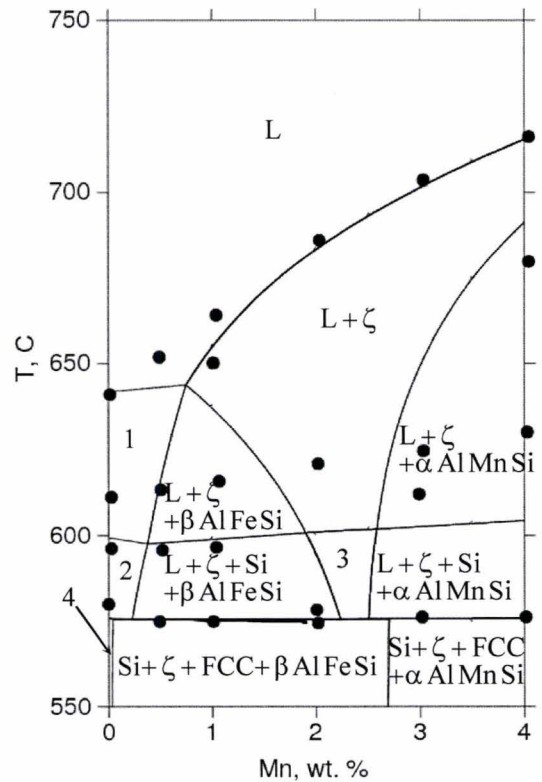
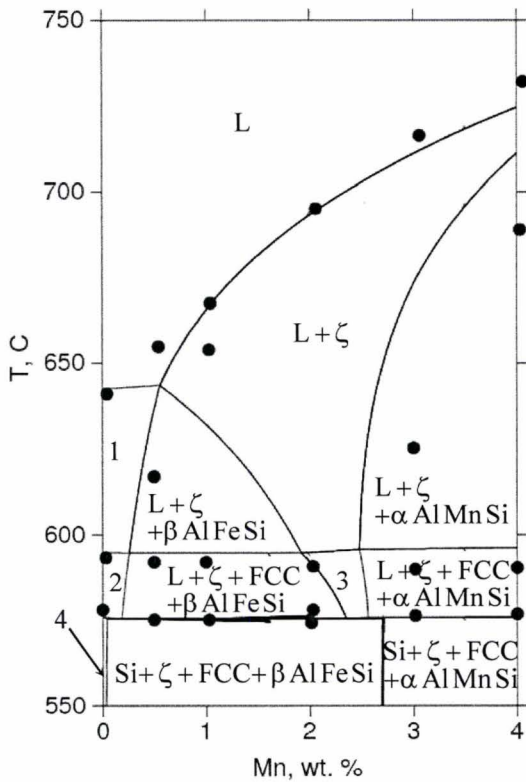


Figure 3.11: Isoplethal section with 2wt. % Fe and 10 wt.% Si (1: L+βAlFeSi, βAlFeSi+FCC+L, 3: FCC+L+ζ and βAlFeSi+Si+FCC). **Figure 3.12: Isoplethal section with 2wt. % Fe and 14 wt.% Si (1: L+βAlFeSi, 2: L+Si+βAlFeSi, 3: Si+L+ζ and 4: βAlFeSi+Si+FCC).**

It should be highlighted that the ζ-phase was the only phase whose thermodynamic properties were evaluated in the course of optimization. In other words, the thermodynamic properties of all other phases seen on isothermal and isoplethal sections reported by Zakharov et al. (1988 & 1989) were taken from the COST-507 database without any alterations. An obvious reason to retain their properties unchanged was that even smallish “adjustments” would jeopardize consistency of this widely used and highly acclaimed database. It is worth emphasizing, however, that there are noteworthy differences between quantities experimentally measured by Zakharov et al. (1988 &

1989) and their computed counterparts even for equilibria in which the ζ -phase does not participate. Examples presented in Table 3.5 demonstrate that the difference in liquidus temperature may exceed twenty degrees. Moreover, there is no conformity between experimental observations and thermodynamic predictions with respect to the nature of the first solid phase forming during solidification. These disparities do not allow for anticipation that a good match between the experimental and computed locations of phase boundaries will result from the assessment.

The assessment was carried out by using PARROT – the Thermo-Calc’s module tailored for this purpose. The optimization was solely based on experimental information reported by Zakharov et al. (1989 & 1989). Uncertainties of compositions and temperatures were assigned after a careful reviewing of experimental procedures employed. In particular, it was concluded that the measurements of liquidus temperatures were more accurate than those corresponding to equilibria involving three or more phases. Drawings of isoplethal and isothermal sections presented by Zakharov et al. (1988 & 1989) were digitized; errors introduced by digitizing were negligible in comparison with experimental inaccuracies.

Since the sublattice model attributed to the ζ -phase is $\text{Al}_{16}(\text{Fe}_y, \text{Mn}_{1-y})_4 \text{Si}_3$, the following expression can be used for representing its Gibbs energy:

$$G^\zeta = y^0 G_{\text{Al:Fe:Si}} + (1-y)^0 G_{\text{Al:Mn:Si}} + 4RT(y \ln y + (1-y) \ln(1-y)) + \sum_{i=0}^n {}^i L_{\text{Al:Fe,Mn:Si}} (1-2y)^i \quad (3.2)$$

Table 3.5: Comparison between experimentally measured and calculated liquidus temperatures (differences are given in parentheses)

Mn, wt. %	Liquidus temperature, °C		Precipitating phase	
	Zakharov <i>et al.</i>	COST-507	Zakharov <i>et al.</i>	COST-507
Isoplethal section with 2 wt.% Fe and 10 wt.% Si				
0	641.2	642.4 (+1.2)	β – AlFeSi	β – AlFeSi
0.5	654.6	643.5 (–11.1)		
Isoplethal section with 2 wt.% Fe and 14 wt.% Si				
0	641.3	641.9 (+0.6)	δ – AlFeSi	β – AlFeSi
0.5	652.2	643.2 (–9.0)		
Isoplethal section with 1 wt.% Fe and 10 wt.% Si				
3	697.4	699.6 (+2.2)	α – AlMnSi	α – AlMnSi
4	719.5	717.8 (–1.7)		
Isoplethal section with 1 wt.% Fe and 14 wt.% Si				
3	691.2	686.4 (–4.8)	α – AlMnSi	α – AlMnSi
4	710.7	704.6 (–6.1)		
Isoplethal section with 3 wt.% Fe and 10 wt.% Si				
0	667.3	667.5 (+0.2)	β – AlFeSi	β – AlFeSi
0.5	678.4	668.5 (–9.9)		
1	686.0	669.4 (–16.6)		
Isoplethal section with 3 wt.% Fe and 14 wt.% Si				
0	682.1	667.4 (–14.7)	δ – AlFeSi	β – AlFeSi
0.5	687.6	668.6 (–19.0)		
1	691.5	669.8 (–21.7)		

In addition to terms related to the thermodynamic properties of pure components, it was assumed that the standard Gibbs energies also contained terms linearly depending on temperature:

$${}^0G_{\text{Al:Fe:Si}} = 16{}^0G_{\text{Al}}^{\text{fcc-A1}} + 4{}^0G_{\text{Fe}}^{\text{bcc-A2}} + 3{}^0G_{\text{Si}}^{\text{diamond-A2}} + V_{11} + V_{12}T \quad (3.3)$$

$${}^0G_{\text{Al:Mn:Si}} = 16{}^0G_{\text{Al}}^{\text{fcc-A1}} + 4{}^0G_{\text{Mn}}^{\text{hcp-A3}} + 3{}^0G_{\text{Si}}^{\text{diamond-A2}} + V_{13} + V_{14}T \quad (3.4)$$

where V_{11}, \dots, V_{14} are model's parameters.

It is impossible to decide on the highest order of interaction, *i.e.* the upper summation limit n in (3.2), needed in the phase's model a priori. It is known, however, that if a sublattice model is reasonably selected, then only few if any excess terms are required. Due to this reason, the following expression was used for the excess Gibbs energy:

$${}^{\text{ex}}G^{\zeta} = y(1-y)(V_{20} + V_{21}T) \quad (3.5)$$

where V_{20} and V_{21} are coefficients whose statistically optimal values are resulted from the optimization procedure.

Following an unanimously adopted rule “the lesser the number of adjustable variables the better”, various scenarios were tried numerically. By using the “trials-and-errors” approach, it was found that the accuracy of fitting had not been noticeably worsened by using lesser than six parameters. More specifically, it was found that V_{21} could be set equal to zero, and that V_{11} and V_{12} could be equated with V_{13} and V_{14} , correspondingly. It is clear from illustrative Figure 3.13 and Figure 3.14 that the difference between the

isopleths calculated with three (solid lines) and six (dashed lines) is insignificant in comparison with the difference between the computed and experimentally determined phase boundaries. The same was observed for all other isoplethal and isothermal section depicted by Zakharov et al. (1988 & 1989).

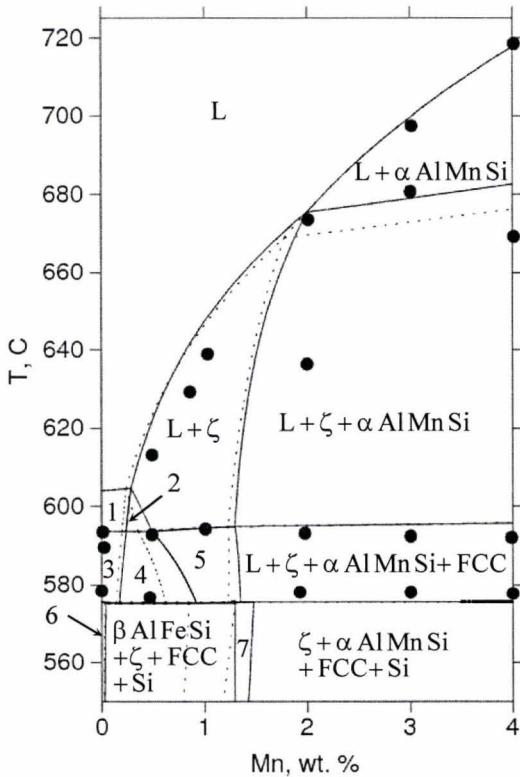


Figure 3.13: Isoplethal section with 1 wt.% Fe and 10 wt.% Si (1: L+βAlFeSi, 2: L+βAlFeSi+ζ, 3: L+βAlFeSi+FCC, 4: L+βAlFeSi+FCC+ζ, 5: FCC+L+ζ, 6: βAlFeSi+Si+FCC and 7: FCC+Si+ζ).

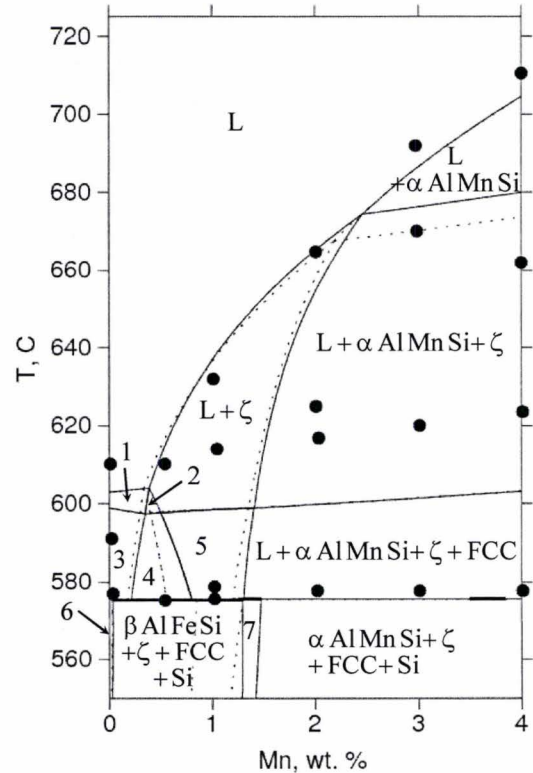


Figure 3.14: Isoplethal section with 1 wt.% Fe and 14 wt.% Si (1: L+βAlFeSi, 2: L+βAlFeSi+ζ, 3: L+βAlFeSi+Si, 4: βAlFeSi+Si+L+ζ, 5: L+Si+ζ, 6: βAlFeSi+Si+FCC and 7: FCC+Si+ζ).

Based on the outcome of the optimization procedure, the following model for the ζ-phase is proposed:

$${}^0G_{Al:Fe:Si} = 16{}^0G_{Al}^{fcc-A1} + 4{}^0G_{Fe}^{bcc-A2} + 3{}^0G_{Si}^{diamond-A2} - 388580 + 98T \quad (3.6)$$

$${}^0G_{\text{Al:Mn:Si}} = 16{}^0G_{\text{Al}}^{\text{fcc-A1}} + 4{}^0G_{\text{Mn}}^{\text{hcp-A3}} + 3{}^0G_{\text{Si}}^{\text{diamond-A2}} - 388580 + 98T \quad (3.7)$$

$${}^0L_{\text{Al:Fe,Mn:Si}} = -409442 \quad (3.8)$$

Isoplethal sections calculated with (3.6)-(3.8) are compared with experimental quantities in Figure 3.15-Figure 3.18.

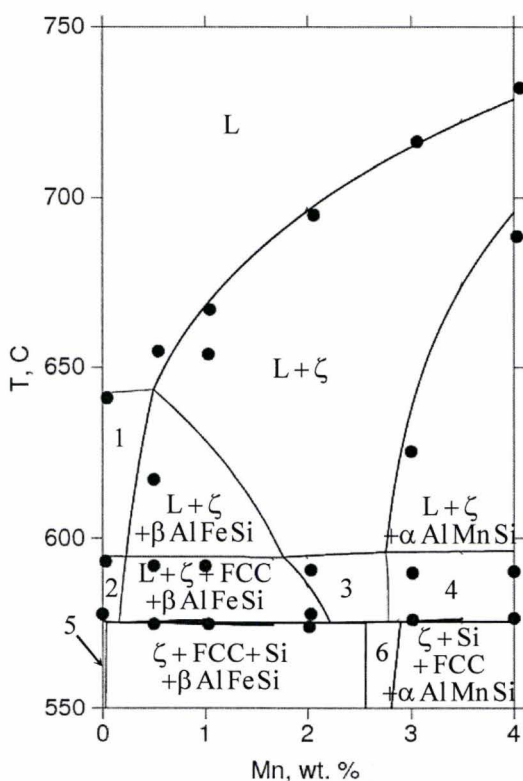


Figure 3.15: Isoplethal section with 2 wt.% Fe and 10 wt.% Si (1: L+βAlFeSi, 2: βAlFeSi+FCC+L, 3: FCC+L+ζ, 4: αAlMnSi+FCC+L+ζ, 5: βAlFeSi+Si+FCC and 6: FCC+Si+ζ).

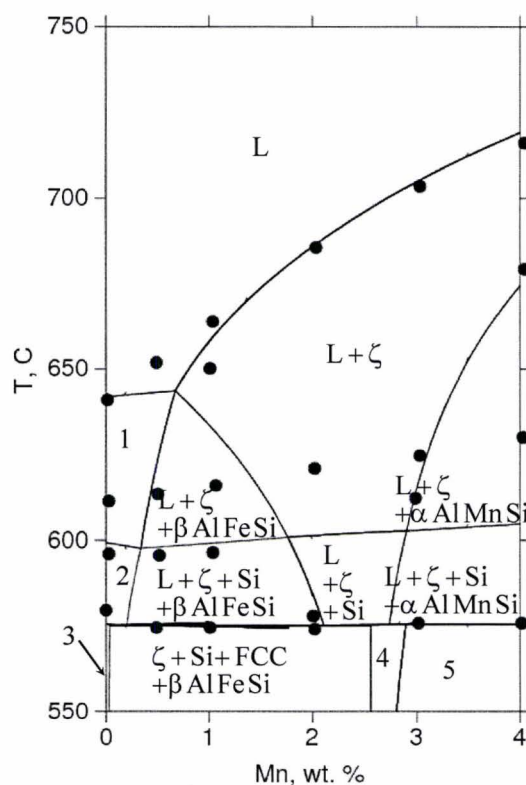


Figure 3.16: Isoplethal section with 2 wt.% Fe and 14 wt.% Si (1: L+βAlFeSi, 2: L+Si+βAlFeSi, 3: βAlFeSi+Si+FCC, 4: FCC+Si+ζ and 5: αAlMnSi+Si+FCC+ζ).

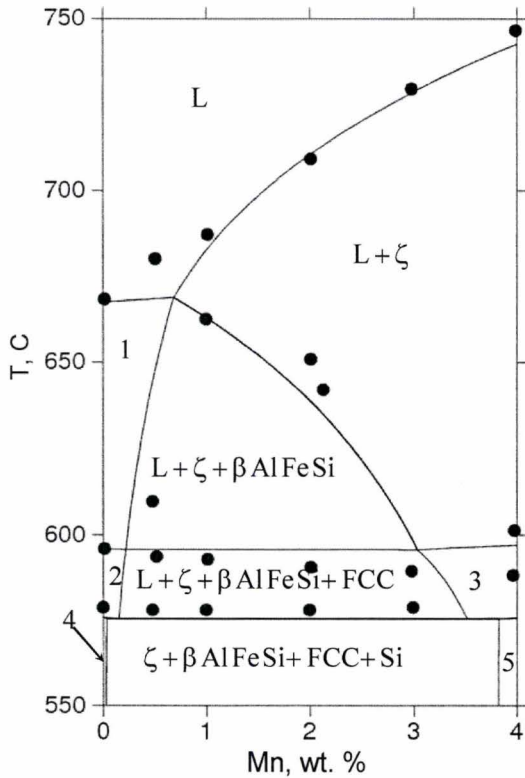


Figure 3.17: Isolethal section with 3 wt.% Fe and 10 wt.% Si (1: L+βAlFeSi, L+FCC+βAlFeSi, 2: L+ζ+βAlFeSi+FCC, 3: FCC+L+ζ, 4: βAlFeSi+Si+FCC and 5: Si+FCC+ζ).

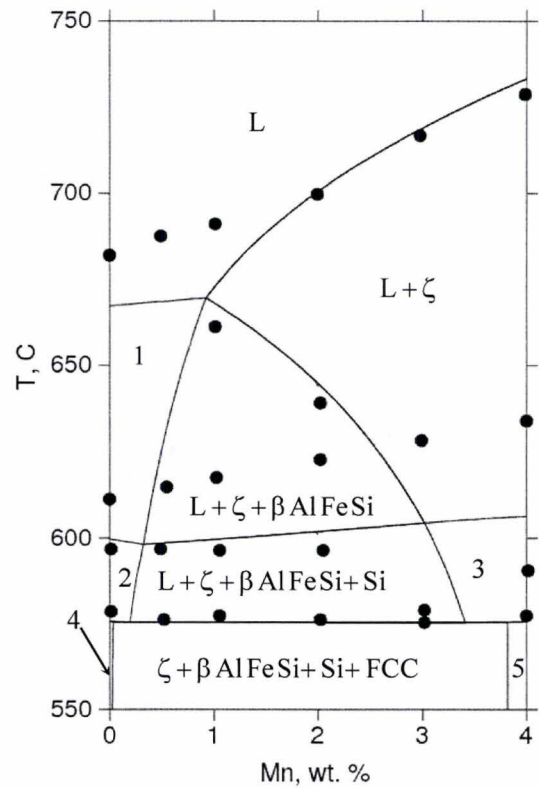


Figure 3.18: Isolethal section with 3 wt.% Fe and 14 wt.% Si (1: L+βAlFeSi, 2: βAlFeSi+Si+L, L+ζ+βAlFeSi+Si, 3: Si+L+ζ, 4: βAlFeSi+Si+FCC and 5: Si+FCC+ζ).

Computed isothermal sections are matched with experimentally determined ones in Figure 3.19-Figure 3.22. At first glance, the deviations are reproachable, but it should be recalled that according to Table 3.5, the discrepancies between Zakharov et al. (1988 & 1989) data and COST-507 predictions are large even for equilibria in which the ζ-phase does not participate. It is worth repeating that the optimization was performed by using information on phase equilibria only. Such quantities as enthalpies of dissolution of the ζ-phase with varying Fe/Mn ratios would be indispensable, indeed. Unfortunately, the thermodynamic properties of the ζ-phase have never been a subject of a direct

experimental investigation. A lack of thermodynamic data is caused in part by tremendous difficulties associated with the synthesis of ζ as an individual phase.

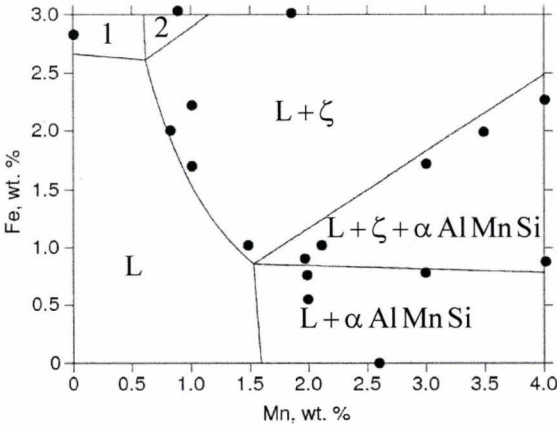


Figure 3.19: Isothermal section at 660°C (933.15 K) with 10 wt.% Si (1: L+ β AlFeSi and 2: L+ β AlFeSi+ ζ).

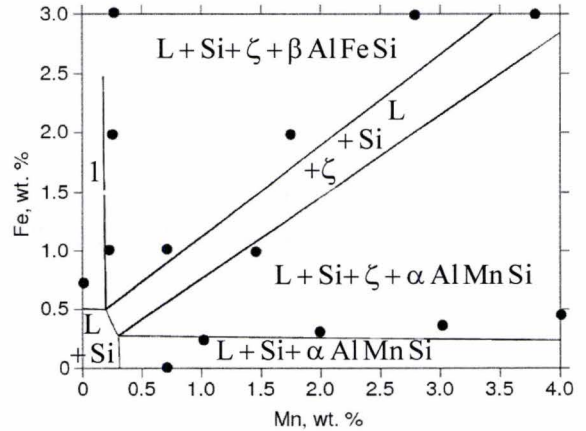


Figure 3.20: Isothermal section at 580°C (853.15 K) with 10 wt.% Si (1: L+Si+ β AlFeSi).

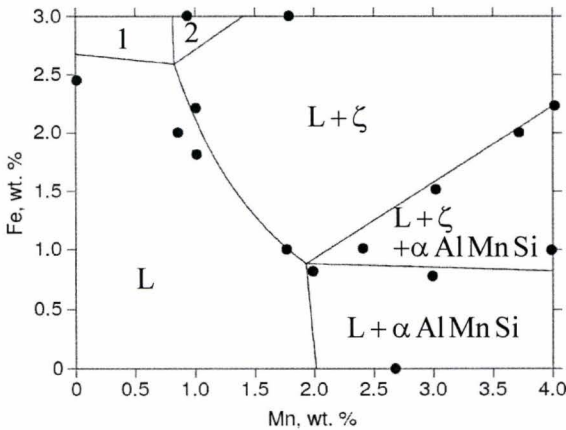


Figure 3.21: Isothermal section at 660°C (933.15 K) with 14 wt.% Si (1: L+ β AlFeSi and 2: L+ β AlFeSi+ ζ).

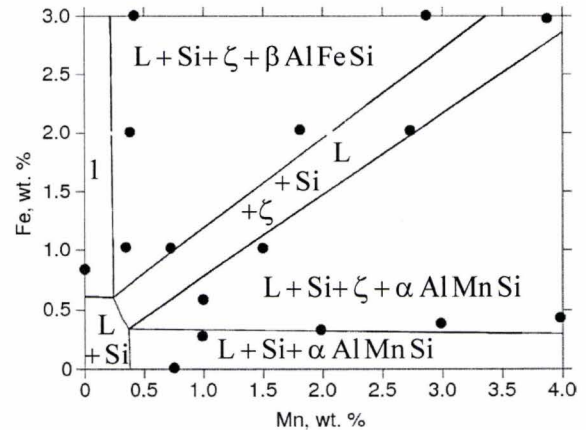


Figure 3.22: Isothermal section at 580°C (853.15 K) with 14 wt.% Si (1: L+Si+ β AlFeSi).

3.5 Conclusions

More than 2 wt.% of intermetallic phases mainly composed of the ζ -phase $\text{Al}_{16}(\text{Fe}, \text{Mn})_4\text{Si}_3$ were detected in as-cast and heat-treated AA6111 aluminum alloys.

Thermodynamic estimations predict that this phase does not dominate in the alloy and that the overall content of intermetallic phases should not be greater than 1.5 wt.%. In an attempt to address this contradiction, a re-evaluation of the thermodynamic properties of the ζ -phase was carried out. Although the refined thermodynamic description of $\text{Al}_{16}(\text{Fe},\text{Mn})_4\text{Si}_3$ presented in this work has its own merit, the conflict between the experimental observations and thermodynamic predictions has not been successfully resolved. It seems that the disparity cannot be eliminated by altering the properties of the ζ -phase only, and that the descriptions of the Gibbs energies of other phases in the quaternary system Al-Fe-Mn-Si deserve revisiting.

A full-fledged re-optimization of this system, however, is not an easy task to perform due to a lack of reliable thermodynamic information on many intermetallic phases including $\text{Al}_{16}(\text{Fe},\text{Mn})_4\text{Si}_3$. From this angle, a recently developed approach combining first-principles calculations and the traditional CALPHAD methodology may turn out to be useful for evaluating phase stabilities in multicomponent aluminum alloys. In particular, Ravi and Wolverton (2005), who thoroughly compared the ThermoTech and CompuTherm databases for Al alloys, computed enthalpies of formation of some phases seen in 3xxx and 6xxx Al alloys. Such type of calculations carried out for the ζ -phase may shed light into the actual nature of phase equilibria in commercially important aluminum alloys including AA6111.

CHAPTER 4

Recrystallization Kinetics

Phenomenologically from a microstructural perspective, the recrystallization process is regarded as a phase transformation whose kinetics can be discussed in terms of its component rates of nucleation and growth. Since the pioneering work on overall transformation kinetics by Kolmogorov, Avrami, Johnson and Mehl, interests in the kinetic modeling of recrystallization has received a lot of attention with a desire for gaining insights into the mechanisms associated with the complexity of the occurring structural change. The following chapter reviews the different modeling techniques that have been developed for recrystallization studies.

4.1 Formal Kinetics of Primary Recrystallization (The Johnson-Mehl-Avrami-Kolmogorov (JMAK) Model)

Primary recrystallization is identified by nucleation of new, strain-free grains in the microstructure and their subsequent growth replacing the deformed material. Hence, recrystallization kinetics is considered similar to solid-state transformations involving nucleation and growth reactions (Christian, 1975; Humphreys and Hatherly, 1995). Such reactions are commonly described by a simple analytical geometrical model referred to as the JMAK model. The model represents the relation between the fraction of the assembly

transformed and time under isothermal conditions. A typical characteristic of such relation is a sigmoidal curve form in which the volume fraction transformed increases slowly at the beginning; is followed by a linear increasing rate and then slows down again due to the reduction in growth rates resulting from the mutual impingement of growing grains. The model assumes a constant nucleation rate \dot{N} and a linear growth rate \dot{G} . If V is the volume of a recrystallizing grain at time t , then the extended volume fraction X_{VEX} is expressed by:

$$X_{VEX} = \int_0^t V \dot{N} dt = f \dot{G}^3 \int_0^t t^3 \dot{N} dt \quad (4.1)$$

where f is a shape factor equal to $4\pi/3$ for spheres.

Such extended volume fraction accounts for impingement by including the phantom nuclei that could have formed in an already recrystallized material volume by continuous nucleation. Thus, it is directly related to the kinetic laws of growth which could be separated from the geometrical problem of impingement (Cumbrera and Sanchez-Bajo, 1995). On the basis of a spatial randomness of the process, the actual fraction of recrystallized material X_V can then be obtained from the extended volume fraction by integrating the relation $dX_V = (1 - X_V) dX_{VEX}$ leading to:

$$X_V = 1 - \exp(-X_{VEX}) \quad (4.2)$$

Substituting (4.1) in (4.2) for a spherical volume and assuming isotropic growth, the volume fraction recrystallized is then expressed as:

$$X_V = 1 - \exp\left(\frac{-\pi \dot{N} \dot{G}^3 t^4}{3}\right) \quad (4.3)$$

Expression (4.3) is generally represented as the so-called JMAK equation:

$$X_V = 1 - \exp(-kt^n) \quad (4.4)$$

or

$$\ln[-\ln(1 - X_V)] = n \ln t + \ln k \quad (4.5)$$

The isothermal transformation rate can then be obtained by differentiating equation (4.4) and eliminating time yielding:

$$\frac{dX_V}{dt} = nk^{1/n} (1 - X_V) \left[\ln(1 - X_V) \right]^{(n-1)/n} \quad (4.6)$$

where n is the JMAK or Avrami exponent reflecting the nucleation rate and/or the growth morphology; and k is a thermally activated rate constant containing all the temperature dependent constants, i.e. nucleation and growth rates. In its simplest form k is assumed to demonstrate an Arrhenius behavior following the expression (Henderson, 1979; Cumbreira and Sanchez-Bajo, 1995):

$$k = k_0 \exp(-E / RT) \quad (4.7)$$

where E is the apparent activation energy including contributions from both nucleation and growth activation energies. By plotting $-\ln(1 - X_V)$ versus $\ln t$ for different temperatures, both n and E can be evaluated from the slope and the intercept of the plot, respectively.

It can be seen from (4.3) that the Avrami exponent equals 4 for the above discussed case of constant nucleation and growth rates, and a random spatial distribution of nucleation

sites. Another case of significant importance especially when dealing with particle containing materials or high deformations is known as site saturated nucleation. For this case all nucleation events are assumed to occur at the onset of recrystallization and an Avrami exponent of 3 results. The JMAK equation also holds for other cases of transformation including decreasing nucleation rate, diffusion controlled growth and random nucleation at specific volumes within the material such as grain boundaries. Table 4.1 lists the values of n for different experimental conditions.

Table 4.1: Values of n in the JMAK kinetic relation (Christian, 1975)

Condition	n
Increasing nucleation rate	>4
Constant nucleation rate	4
Decreasing nucleation rate	3-4
Zero nucleation rate (site saturation)	3
Grain edge nucleation after saturation	2
Grain boundary nucleation after saturation	1

4.1.1 Criticisms to the JMAK Equation

Despite early experimental results which conformed to the JMAK recrystallization model, the kinetics of recrystallization usually deviate in a negative manner from the linear behavior of the Avrami plots. This is reflected experimentally in the form of a non-constant Avrami exponent which may decrease as recrystallization proceeds (Vandermeer, 2001). Moreover, under uniaxial growth conditions, the JMAK

model predicts an exponent greater than or equal to 3. However, experimental reported values are usually around 2 for moderate to heavily deformed materials and even sometimes less than 1 (Furu et al., 1990; Vandermeer, 2001). The magnitude of deviation of the Avrami exponent is also higher in the final stages of recrystallization and at lower annealing temperatures (Vandermeer, 1995). The reasons for such deviations have been attributed to the strict and idealized assumptions of the JMAK theory, mainly the constant interface growth rate. It is now accepted that the growth rate during recrystallization is not constant but tends to decrease with annealing time. Such decreasing migration rate may be due to the microstructural inhomogeneity of the material where a spatial variation in the driving pressure for recrystallization is expected. In addition, the driving pressure may also be reduced by a competing recovery process occurring simultaneously with recrystallization. This leads to a non-constant growth rate in both space and time (Furu et al., 1990). A decrease in boundary mobility with the progress of a recrystallization reaction due to solute-drag effects will also result in a decreasing growth rate (Vandermeer, 2000). Non-constant growth rates depending on local grain environments were also observed during Monte Carlo simulations for single phase grain growth in two and three dimensions. Recrystallization simulations with variable stored energy among grains also confirmed the low and non-constant Avrami exponents (Doherty et al., 1997).

The first attempt to quantify such variation in growth rate with time was performed by English and Backofen on an iron-3.25% silicon alloy using the Cahn-Hagel

analysis for measuring growth rates (Vandermeer and Jensen, 1998). They proposed the relation:

$$\dot{G} = \frac{A}{1 + c_1 t} \quad (4.8)$$

where A and c_1 are empirical constants. However, the above relation failed to account for experimentally observed constant growth rates at long annealing times. To account for such shortcoming, Vandermeer and Jensen (1998) introduced a limiting growth rate value A_1 in the above relation leading to the expression:

$$\dot{G} = \frac{A}{1 + c_1 t} + A_1 \quad (4.9)$$

The variation of growth rate with time during recrystallization has also been the subject of several analytical modeling approaches such as those by Furu et al. (1990) and Doherty et al. (1993). Their models are commonly referred to as the relaxed JMAK models and they retain the JMAK requirement of uniform impingement (Vandermeer, 2001). Furu et al. (1990) based their analytical treatment on an approach where the growth rate is assumed to vary on a small scale compared with the nucleation site spacing (Furu et al., 1989). Such treatment is of significant importance when dealing with particle-stimulated nucleation of recrystallization where local stored energy gradients are expected in the deformation zones around the particles. Consequently, the growth rate will be larger in the vicinity of the particles and decreases on going away from the particles. Their model assumptions were:

- Heterogeneous nucleation from homogeneously distributed sites

- Site saturation transformation kinetics
- An isotropic non-constant growth rate which varies locally within the material volume

In order to quantify the growth rate variation, the deformation zone model developed by Ørsund and Nes (1988) was adopted leading to:

$$\dot{G} = \begin{cases} \dot{G}_M [\kappa^2 + 2(1-\kappa)\dot{G}_M t / \lambda]^{-1/2}, & t < t^* \\ \dot{G}_M, & t \geq t^* \end{cases} \quad (4.10)$$

where \dot{G}_M is the isotropic matrix growth rate, κ is a constant, λ is the width of the deformation zone and $t^* = (1 + \kappa)\lambda / 2\dot{G}_M$.

By considering a site saturation case for spherical particle of equal size, and where one new grain is formed in each deformation zone. The transformation kinetics was expressed by:

$$X_V = 1 - \exp \left[-\frac{4}{3} \pi N \left(\int_0^t \dot{G} dt \right)^3 \right] \quad (4.11)$$

where N is the number of nucleation sites per unit volume.

The authors also applied the small scale approach to growth rate variations resulting from a simultaneous recovery process during recrystallization. They expressed the time dependent growth rate by the relation:

$$\dot{G} = \dot{G}_0 [1 + (t/\tau_1)]^{-b}, \quad 0 \leq b < 1 \quad (4.12)$$

where, τ_1 is a relaxation time parameter and \dot{G}_0 is the initial growth rate. Employing the above relation in (4.11) leads to:

$$X_V = 1 - \exp \left\{ -\frac{4}{3} \pi \left[\frac{\tau_1}{(1-b)\tau_2} \right]^3 \left[\left(1 + \frac{t}{\tau_1} \right)^{1-b} - 1 \right]^3 \right\} \quad (4.13)$$

where $\tau_2 = (N\dot{G}_0^3)^{-1/3}$ is a relaxation time parameter for the recrystallization reaction.

Equation (4.13) can then be rewritten for the limiting cases of $\tau_1/\tau_2 \gg 1$ as:

$$X_V = 1 - \exp \left\{ -\frac{4}{3} \pi \left[\frac{t}{\tau_2} \right]^3 \right\}, \quad X_V \leq 0.95 \quad (4.14)$$

or in the case for $\tau_1/\tau_2 \ll 1$ as:

$$X_V = 1 - \exp \left\{ -\frac{4}{3} \pi \left[\frac{\tau_1}{(1-b)\tau_2} \right]^3 \left(\frac{t}{\tau_1} \right)^{3(1-b)} \right\}, \quad X_V \geq 0.05 \quad (4.15)$$

The authors also analyzed the variation of growth rate within a material due to an inhomogeneous Zener drag pressure. For a stored energy per unit volume (i.e. driving pressure) P_D , a boundary mobility M and a dragging pressure of $2\pi\gamma r^2 \rho_i$, where ρ_i is the density of the particles and γ is the surface tension of the moving grain boundary, the local growth rate \dot{G}_i is expressed by:

$$\dot{G}_i = M (P_D - 2\pi\gamma r^2 \rho_i) \quad (4.16)$$

The mean growth rate can then be expressed by:

$$\bar{G} = M \left(P_D - 2\pi\gamma r^2 \sum_i f(\rho_i) \rho_i \right) \quad (4.17)$$

where $f(\rho_i)$ is the volume fraction of the material for which the dragging particle density is ρ_i . If the spatial variation of ρ_i is on a coarse scale, then it can be assumed

that recrystallization within a particular volume will be unaffected by its neighbours, and the kinetics for the whole material can then be expressed by:

$$X_V = 1 - \sum_i f(\rho_i) \exp\left(-\frac{4}{3}\pi N \dot{G}_i^3 t^3\right) \quad (4.18)$$

The above model was later extended by Myhr et al. (1997) to include the Zener drag pressure P_Z . They proposed the following relation for the growth rate:

$$\dot{G} = \dot{G}_0 \left(\frac{1}{\sqrt{1+(t/\tau_1)}} - A \right) \quad (4.19)$$

where $A = P_Z/P_D^0$, $G_0 = MP_D^0$ and P_D^0 is the stored energy at the start of an annealing treatment.

In an attempt to extend the JMAK model to deal with time-dependent nucleation and growth rates, Doherty et al. (1993) assumed power laws for the nucleation and growth rates following the relations:

$$\dot{G} = \psi \tau^{-g} \quad (4.20)$$

$$\dot{N} = \zeta \tau^m \quad (4.21)$$

where ψ , ζ , g and m are constants. Their derivation which was based on the extended volume concept resulted in a relation of the form:

$$X_V = 1 - \exp\left[-\frac{4}{3}\pi\zeta\psi(1-g)^3 t^{4+m-3g} \{10-6g\}\right] \quad (4.22)$$

The expression is similar to equation (4.4) and yields an Avrami exponent $n = 4 + m - 3g$. However, the use of power law functions to describe growth rates have

been criticized for their physical limitations at very short times where the rates will tend to infinity (Vandermeer and Jensen, 1998).

Another variant of the JMAK model which employed non-constant growth rates was proposed by Woldt (2001). In his derivation, he suggested two major changes to the original JMAK model. First, a nucleation rate related to the size of the recrystallized-deformed interfacial area present and expressed by:

$$\dot{N}(t) = \mu_p \dot{V}_{VEX}(t) \quad (4.23)$$

Where μ_p represents a probability factor for nucleation at the interface and V_{VEX} is the extended volume. The model assumed the existence of a very small number of primary nuclei N_0 which grow spontaneously at the start of the transformation and later trigger further nucleation among their interface. The second change to the JMAK model included an exponentially decreasing growth rate for each grain given by:

$$G(t, \tau) = \bar{R} \exp(-\omega(t-\tau)) \quad (4.24)$$

Where τ represents the nucleation moment of the individual grain, ω is a reciprocal of a time constant relating to the decrease in growth speeds and \bar{R} is an average grain radius. The extended volume was then determined by the integral equation:

$$V_{VEX}(t) = N_0 V(t) - \mu_p \int_0^t V_{VEX}(\tau) \frac{d}{d\tau} V(t-\tau) d\tau \quad (4.25)$$

The model was able to reproduce both the sigmoidal shape of the transformation and the non-linear deviations in the Avrami plots during later stages of transformation. However,

the slope values for some cases nearly approached zero. An effect attributed to the selection of an exponentially decaying growth rate.

Erukhimovitch and Baram (1994 & 1996) also addressed the deviations from linearity in the Avrami plots and the overestimated recrystallization kinetics obtained by the formal JMAK theory. They attributed such deviations to the inclusion of phantom nuclei in the original development by Avrami which leads to inadequate impingement compensation and an overall simplification of the real physical conditions. Instead, the authors suggested exclusion of such “nonexistent” phantom nuclei by only assuming randomness in the untransformed time-dependent volume. They derived an integral equation for the kinetics of nucleation and growth reactions of the form:

$$X_v(T, t) = \frac{4\pi}{3} \dot{G}^3 \dot{N} \int_0^t (t - \tau)^3 [1 - X_v(T, \tau)]^2 d\tau \quad (4.26)$$

The above expression provided a much better agreement over the JMAK equation for the experimental observations at the later stages of recrystallization in iron and copper. However, an assessment by Michaelsen et al. (1996) has shown that the above expression fails to converge on numerical integration except for the case of a fully transformed material at all time. Moreover, Monte-Carlo simulations of recrystallization due to Srolovitz et al. (1986) and Rollet et al. (1992) have shown that the Avrami interpretation of the impingement problem is a fair representation of the real process and could not be held accountable for the deviations from linearity in the Avrami plots.

An alternative treatment of the shortcomings of the JMAK kinetic description of recrystallization was proposed by Kruger and Woldt (1992). In their work on the recrystallization kinetics in copper, the authors attributed deviations in the Avrami plots to the inhomogeneity of deformation in polycrystalline material and the associated local variations in stored energy. Accordingly, an activation energy distribution was proposed to account for such variations by dividing the sample into independent regions with transformation kinetics following the JMAK theory. Each independent region is characterized by a local activation energy and Avrami exponent. The kinetics for the whole sample is then obtained by superimposing these individual JMAK processes with their corresponding activation energies. The expression for the volume fraction recrystallized was expressed by:

$$X_v = \int_0^{\infty} p(E)\Theta(T, E) dE \quad (4.27)$$

$p(E)$ represents a normalized distribution of the activation energies while Θ denotes the standard JMAK kinetics derived under either isothermal or non-isothermal conditions. The above expression could be solved numerically or analytically using Laplace transforms.

4.2 The Microstructural Path Methodology (MPM)

In an attempt to improve the JMAK approach, Vandermeer and Rath (1989a & 1989b) applied the mathematics of Laplace transforms to analyze the experimental evolution of global and local microstructural properties associated with recrystallization.

They utilized additional microstructural parameters in the analysis. This included the interfacial area per unit volume between the recrystallized and unrecrystallized material (S_V) and the extended interfacial area (S_{VEX}). For a random distribution of recrystallized grains, the two quantities are related by the expression:

$$S_{VEX} = S_V / (1 - X_V) \quad (4.28)$$

Following the JMAK approach, the nucleation and growth of independently recrystallizing grains were expressed in integral form as:

$$X_{VEX} = \int_0^t V(t-\tau) \times \dot{N}(\tau) \times d\tau \quad (4.29)$$

$$S_{VEX} = \int_0^t S(t-\tau) \times \dot{N}(\tau) \times d\tau \quad (4.30)$$

where $V(t-\tau)$ and $S(t-\tau)$ are the volume and interfacial area respectively at time t of a recrystallized grain nucleated at time τ . For the case of shape-preserved spheroid grains, the volume and interfacial area could be expressed in terms of the grain radius as:

$$V(t-\tau) = K_V \times a(t-\tau)^3 \quad (4.31)$$

$$S(t-\tau) = K_S \times a(t-\tau)^2 \quad (4.32)$$

where K_V and K_S are shape factors, while $a(t-\tau)$ is a local microstructural property (radius function) representing the major semi-axis of the spheroid. It is related to the interface migration rate $\dot{G}(t)$ by:

$$a(t-\tau) = \int_{\tau}^t \dot{G}(t) \times dt \quad (4.33)$$

The radius function $a(t-\tau)$ could be determined by measuring the largest unimpinged recrystallized grain intercept length d_l on a plane polished surface.

By adopting the mathematical methodology developed by Gokhale and Dehoff (1985) for the estimation of nucleation and growth rates from the time variation of X_V and S_V during phase transformations, and assuming that the local growth rate of a recrystallized grain is independent of the nucleation and growth events of other grains in the system. Equations (4.29) and (4.30) are regarded as convolution integrals whose Laplace transforms are then expressed as:

$$\text{Lpt}\{X_{VEX}\} = \text{Lpt}\{\dot{N}(t)\} \times \text{Lpt}\{V(t)\} \quad (4.34)$$

$$\text{Lpt}\{S_{VEX}\} = \text{Lpt}\{\dot{N}(t)\} \times \text{Lpt}\{S(t)\} \quad (4.35)$$

By rearranging the above equations and performing and inverse Laplace transform, the nucleation frequencies can be determined if X_{Vex} and $V(t)$ or S_{VEX} and $S(t)$ are known following the expression:

$$\dot{N}(t) = \text{Lpt}^{-1}\left[\text{Lpt}\{X_{VEX}\} / \text{Lpt}\{V(t)\}\right] = \text{Lpt}^{-1}\left[\text{Lpt}\{S_{VEX}\} / \text{Lpt}\{S(t)\}\right] \quad (4.36)$$

The radius function $a(t-\tau)$ can then be obtained by combining equations (4.34) and (4.35) to eliminate $\dot{N}(t)$ and applying the convolution theorem resulting in the expression:

$$\int_0^t K_V \times [a(t-\tau)]^3 \times S_{VEX}(\tau) \times dt = \int_0^t K_S \times [a(t-\tau)]^2 \times X_{VEX}(\tau) \times dt \quad (4.37)$$

Assuming power law functions for the time dependence of the microstructural properties (X_{VEX}, S_{VEX}, d_l) and the derived functions ($a(t-\tau), \dot{N}(\tau)$), the authors were able to deduce the nucleation rate, growth rate and size of recrystallizing grains under isothermal conditions for a deformed iron single crystal. They adopted a shape-preserved model for the geometry of the recrystallized grains. The above procedure was termed the Microstructural Path Methodology and was later extended to include more complex geometrical impingement patterns dealing with the clustering of recrystallized grains rather than the uniform requirement outlined in the above analysis (Vandermeer, 1995; Vandermeer and Jensen, 2001 & 2003).

4.3 Network Models

This family of modeling is based on a small microstructural length scale. It includes the cellular automata network representations and the node displacement network models. In the cellular automata models, the deformed state is first divided into an assembly of neighboring cells with predetermined characteristics which are mainly a crystallographic orientation and a scalar stored energy term. Each cell possesses its unique transition rules to decide on its state evolution with time relative to its neighbors. For recrystallization such rule is simple and entitles that any unrecrystallized cell will switch to being recrystallized if one of its neighbors is recrystallized. The whole cell assembly is then updated simultaneously allowing for the determination of the recrystallization behavior of the assembly for each time step. Stored energy heterogeneities and non-

constant growth rates can be incorporated in such simulations (Vandermeer, 1995; Miodownik, 2002). On the other hand, the node displacement network models are based on the assumption that recrystallization is a subgrain growth phenomenon. The deformed state is divided into an assembly of cells where each cell is regarded as a subgrain with specific geometry and crystallographic orientation. The cells are further represented by their vertices in order to minimize the amount of data in the simulation. Forces from boundaries acting at each node point in the structure are evaluated and depending on the resulting driving force, and governing mobility rules; the topological events as node displacements, node dissociation and subgrain disappearance are incorporated (Vandermeer, 1995; Humphreys and Hatherly, 1995).

4.4 Monte Carlo Simulations

In Monte Carlo simulations, a continuum microstructure is mapped onto a discrete lattice. The microstructure is divided into finite elements arranged on a regular lattice with specific orientation attributes. The employed interactions and dynamics of these elements are equivalent to those of continuous systems. Grains are then constructed from elements having the same orientation as shown in Figure 4.1, while those with different values are prescribed as being part of a grain boundary with specified discrete energies. The state transition function in Monte Carlo models is a reduction in the local free energy. Hence, recrystallization modeling proceeds by selecting a random element and reorienting it to another grain orientation. The total energy of the new state is then evaluated and if the change is less than or equal to zero, the new orientation of the

element is accepted. The above procedure is repeated by choosing other random elements continuously until the number of reorientation attempts equals the number of elements in the system, i.e. a Monte Carlo time step has passed. The basic limitations of such models include the small scale volume of the model in comparison to the real structure and the absence of a physically-based description of nucleation (Srolovitz et al., 1986; Vandermeer, 1995; Miodownik, 2002; Humphreys and Hatherly, 1995). The pioneering effort in this area was performed by Srolovitz et al. (1986 & 1988) on isotropic two dimensional microstructures. By varying the degree of stored energy, primary recrystallization was modeled for both cases of homogeneous and heterogeneous nucleation conditions. The simulations were able to reproduce the sigmoidal dependence of the recrystallized volume fraction with Avrami exponents of reasonable agreement with the JMAK recrystallization kinetics.

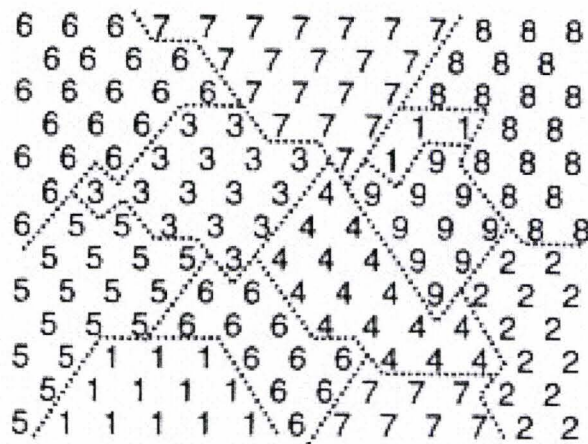


Figure 4.1: The basis of the Monte Carlo simulation method. (Humphreys and Hatherly, 1995)

CHAPTER 5

Experimental Procedure

This chapter describes the experimental procedures employed for the investigation of recrystallization in Al–Mg–Si–Cu alloys. The first part of the chapter presents the fabrication of the alloys and their thermomechanical processing. The second part gives a detailed description of the operational principles of differential scanning calorimetry, the principal characterization technique employed in this study. The procedures utilized in generating and analyzing the thermo-analytical data are also discussed. The final part describes the complementary characterization techniques namely, optical microscopy, microhardness measurements, electron back scatter diffraction microscopy and transmission electron microscopy.

5.1 Materials

Three compositional variants of the Al–Mg–Si–Cu alloy were supplied by Novelis in the form of slabs of 12 mm gauge. The slabs were hot rolled from ingots homogenized for 8 hours at 560 °C. The finish temperature was 364 °C which is hot enough to result in a self-annealed material. The chemical composition of the alloys is specified in Table 5.1. The varying amounts of iron and manganese will allow examining the effects of the intermetallics' population on the recrystallization process. The alloy

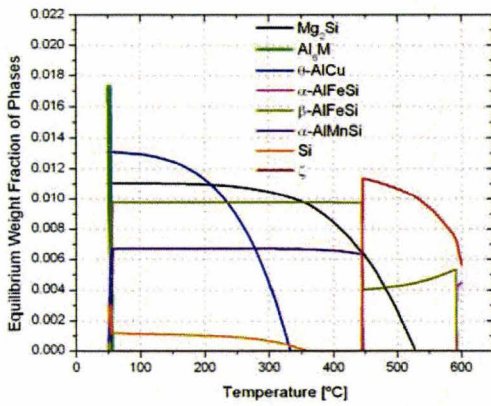
designated 6111-NC has a nominal composition relative to commercial AA6111 alloys. Thus, it was subjected to additional experimental investigations in the course of this study.

Table 5.1: Chemical composition of the investigated alloys in wt.%

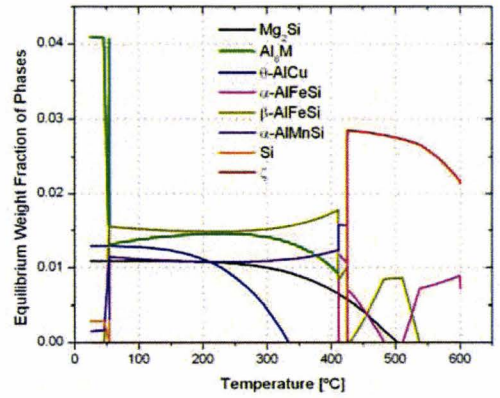
Alloy Designation	Solute Content						
	Si	Fe	Cu	Mn	Mg	Ti	Al
6111-NC	0.71	0.26	0.71	0.2	0.7	0.020	Balance
6111-LC	0.7	0.05	0.68	0.001	0.69	0.022	Balance
6111-HC	0.7	0.61	0.7	0.48	0.69	0.017	Balance

5.2 Cold Rolling

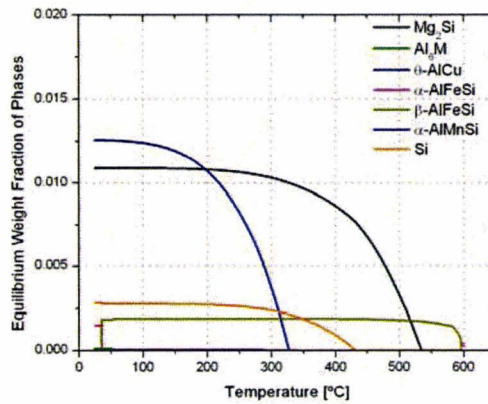
Samples for cold rolling were solution heat treated at 560 °C for two hours in a tube furnace under a dynamic argon atmosphere followed by quenching in water. The time and temperature for heat treatment were based on the ASM guidelines for sheet AA6111 alloys. The heat treatment temperature was also validated by equilibrium property diagrams computed using Thermo-Calc software, and shown in Figure 5.1. The solution treatment was carried out to dissolve the maximum of alloying elements so that a nearly homogeneous solid solution is obtained. The only phases present were the everexisting intermetallics β -AlFeSi, α -AlMnSi and ξ -Al(Fe,Mn)Si.



(a)



(b)



(c)

Figure 5.1: Phase Stability diagrams for: (a) 6111-NC, (b) 6111-HC and (c) 6111-LC.

Rolling was then carried out at room temperature to a reduction in thickness of 90% and 80%, corresponding to true strains of 2.3 and 1.6, respectively. The final thickness was achieved through multiple rolling passes with strain levels ranging from 3% to 7% corresponding to a thickness reduction of 10% to 20%. The slabs were immersed in cold water between passes to avoid dynamic recovery. Their sides were also inverted on alternate passes. All rolling activities were conducted immediately after the solution heat treatment to avoid any room temperature aging. The rolled slabs were stored

at -4 °C until further sample processing. Table 5.2 summarizes the designation of the working samples in this investigation according to their processing routes.

Table 5.2: Processing route and sample designation

Sample Designation	Cold Rolling Reduction [%]	Processing Route
6111-NC-AR	0	As-received from Novelis / No cold rolling
6111-NC-SHT	0	As-received from Novelis / Solution heat treatment Water quenching
6111-NC-90	90	As-received from Novelis / Solution heat treatment Water quenching / Cold rolling
6111-NC-80	80	As-received from Novelis / Solution heat treatment Water quenching / Cold rolling
6111-LC-AR	0	As-received from Novelis / No cold rolling
6111-LC-SHT	0	As-received from Novelis / Solution heat treatment Water quenching
6111-LC-90	90	As-received from Novelis / Solution heat treatment Water quenching / Cold rolling
6111-LC-80	80	As-received from Novelis / Solution heat treatment Water quenching / Cold rolling
6111-HC-AR	0	As-received from Novelis / No cold rolling
6111-HC-SHT	0	As-received from Novelis / Solution heat treatment Water quenching
6111-HC-90	90	As-received from Novelis / Solution heat treatment Water quenching / Cold rolling
6111-HC-80	80	As-received from Novelis / Solution heat treatment Water quenching / Cold rolling

5.3 Differential Power Scanning Calorimetry

5.3.1 Operational Principles

Differential power scanning calorimeters are devices used to measure the amount of energy absorbed or released by a sample when subjected to a defined temperature program. Scanning calorimeters are always based on a twin measuring system design as shown schematically in Figure 5.2.

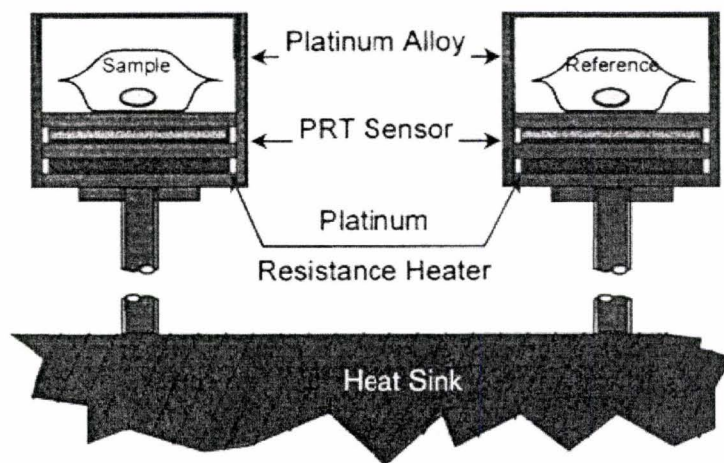


Figure 5.2: Schematic cross-section of a Pyris Diamond power-compensation DSC. (Starink, 2004)

There are two thermally equivalent containers inside a calorimeter. One of them is filled with a reference material, which does not undergo a phase transformation within an investigated temperature region. The other container is filled with a sample, in which a transformation occurs. Both containers are heated with a constant heating rate β in such a manner that their temperatures remain the same at all times. A time-dependent difference $\dot{Q}_S - \dot{Q}_R$ between powers supplied to the sample and to the reference is

measured and recorded. Since the reference does not experience the phase transition, energy provided is exclusively spent for heating. In the case of the sample, a portion of energy supplied is still spent for heating, while the rest of it is used for driving the transformation:

$$\dot{Q}_R dt = c_{pR} \times m_R \times dT \quad (5.1)$$

$$\dot{Q}_S dt = c_{pS} \times m_S \times dT + dH \quad (5.2)$$

where c_{pR} , m_R and c_{pS} , m_S are the specific heat capacities and masses of the reference and sample, respectively. Since the heating rate is constant, temperature increases with time as $T = T_0 + \beta \times t$, where T_0 is temperature at the beginning of the experiment.

Substituting $dT/dt = \beta$ in expressions (5.1) and (5.2) yields:

$$\dot{Q}_R = c_{pR} \times m_R \times \beta \equiv g_R \quad (5.3)$$

$$\dot{Q}_S = c_{pS} \times m_S \times \beta + dH/dt \equiv g_S + dH/dt \quad (5.4)$$

Subtracting (5.3) from (5.4) and rearranging gives:

$$dH/dt = (\dot{Q}_S - \dot{Q}_R) - (g_S - g_R) \equiv \dot{Q} - g \quad (5.5)$$

If the transformation starts at time t_{beg} and is completed at time t_{end} , then the enthalpy of transformation can be calculated as:

$$H = \int_{t_{\text{beg}}}^{t_{\text{end}}} (\dot{Q} - g) d\tau \quad (5.6)$$

The first term on the right hand side, \dot{Q} , represents the heat flow recorded by the machine. In case a phase transition occurs in the sample, it will be reflected as a peak on the heat flow curve with start T_{beg} and finish T_{end} temperatures corresponding to the initial and final deviations of the measured signal from the baseline $g \equiv g_S - g_R$. The baseline is the measured signal by the DSC under steady-state conditions. It reflects the response of the machine to all changes taking place in the sample during linear heating but excluding any heat effects due to a phase transition. Accordingly, it is just the signal resulting from the differences in heat capacities between the sample and reference material. If no phase transition is encountered during the DSC run. Then, the measured curve is simply the baseline. However, if a peak is recorded by the DSC (i.e. a phase transition is taking place), then the baseline in the vicinity of the peak becomes unknown and has to be interpolated between the initial and final baselines (Hemminger and Sarge, 1991). The terms used in describing DSC measured curves are illustrated in Figure 5.3 for a schematic first-order phase transition. The zero line is the measured signal when the instrument is operated without a sample and reference. It indicates the heat capacity differences due to the asymmetry of the measuring system.

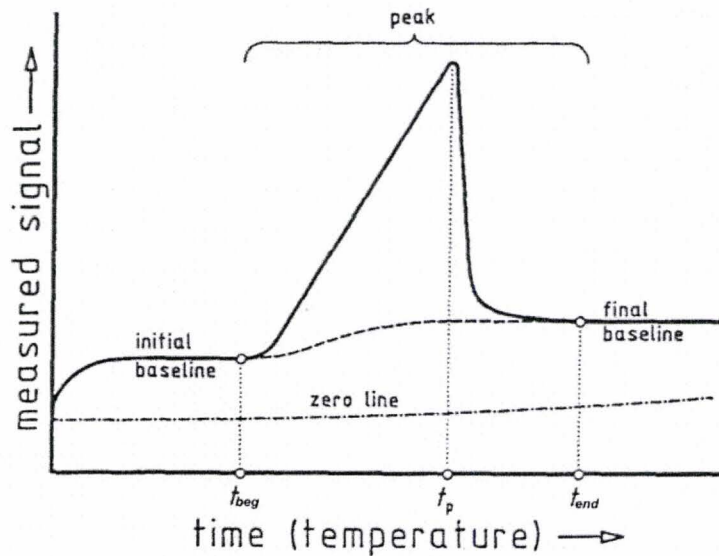


Figure 5.3: Schematic curve for a first-order phase transition. (Hemminger and Sarge, 1991)

5.3.2 The Importance of the Baseline

The enthalpy of transformation can be determined from expression (5.6). This represents the peak area between the measured curve and the baseline. Therefore, a properly drawn baseline is eminent in order to accurately evaluate such area. Nevertheless, expression (5.6) is not easy to apply. Firstly, integration limits are not known exactly (i.e. precise beginning and end points of the peak from the measured curve). Secondly, while heat capacities of many substances (*e.g.* Fe) are known, it cannot be taken for granted that they are known for many other compounds and alloys (*e.g.* steels). Even if temperature dependencies of heat capacities of the sample's states prior to the transformation and after it are known and even though a method of extrapolating them is reliable, nothing is known about fractions of these states during the transformation. Subsequently, the baseline $g \equiv g_S - g_R$ seen in the right-hand-side of

(5.6) is not readily defined. In the past, the amount of heat resulting from the difference in heat capacity of the sample before and after the transition was neglected when compared to the magnitude of heat associated with a phase transition, and errors arising from baseline approximations were considered marginal to the overall experimental error of the instrument (Guttman and Flynn, 1973). However, with the increased sensitivity and precision of modern calorimeters, the proper evaluation of the baseline became a significant contributor to the overall accuracy of a quantitative DSC analysis (Chen et al., 1996). Examples are known where the magnitude of the enthalpy of reaction was altered by approximately 10% by choosing an improper baseline (Dupuy et al., 2000). So how can this elusive baseline be constructed? The answer to this question will be presented in details in the following section.

5.3.3 Methods of Baseline Construction

Several methods have been proposed for baseline construction. They are generally grouped into three categories (Hemminger and Sarge, 1991):

1. Formal methods without physico-chemical justification. A straight line connecting the peak start and peak finish represents the simplest method within this group. Other methods include extrapolating the initial and final heat capacities of the sample to an arbitrary thermodynamic transition temperature and evaluating the area under the curve using these drawn baselines (Guttman and Flynn, 1973). Such procedure

explicitly entails a constant heat capacity of the sample during the transition and a stable and constant baseline.

2. Analytical and numerical methods which impose physico-chemical assumptions regarding the change of the heat capacity during transition. When information is available on the degree of conversion function, the baseline in the peak area is constructed from the shape of the original and final baselines using the relation:

$$g = (1 - \alpha) \underbrace{C_{pI}\beta}_{\text{initial baseline}} + \alpha \underbrace{C_{pF}\beta}_{\text{final baseline}} \quad (5.7)$$

where, C_{pI} and C_{pF} represent the heat capacity of the sample before and after the transition, respectively. When the degree of conversion function is unknown, a straight line is used as a first approximation for the baseline and is then entered into an iterative sequence until no further baseline change occurs. Such method is restricted to situations where changes in heat capacity is a real function of the degree of conversion. Other methods include the use of an exponential function as the interpolated baseline. This is valid for first-order phase transitions where a step change in the sample's heat capacity during a transition is transformed by the measuring system into a function of time (exponential function).

3. Experimental methods which are based on repeating the DSC scan with an inert sample of similar heat capacity as the investigated material. A subtraction of the inert sample curve from the original DSC curve will yield an approximate shape of the

baseline in the vicinity of the peak area. In the case of irreversible reactions as the annealing of deformed metals, the procedure outlined by Andersen and Jensen (1984) allows for reliable isolation of the energy release events. The procedure involves running a first measurement with the deformed sample and using an annealed sample as a reference. The second run is then performed using the same samples. The difference between the two measurements should result in distinguishable thermal events with an approximate baseline shape. However, such procedure suffers from uncertainties relating to the instrument itself. Even with the most modern calorimeters, drifts in the electronic components of the measuring system or heat leaks from or to the surrounding are unavoidable and will occur during repeated scans. Such drifts are very difficult to account for and will introduce errors in the enthalpy determination. An additional approach for constructing an interpolated baseline experimentally may also involve simultaneous measurements of the degree of conversion function by other experiments such as optical, spectroscopic and thermogravimetric methods. In such case, the interpolated baseline in the peak area is a depiction of the degree of conversion function between the initial and final baselines.

Finally, it should be noted that the shape of the baseline does not solely relate to changes in the sample's heat capacity. It is also affected by changes in heat transfer characteristics between the sample and the container or even changes in the radiation

characteristics of the sample. However, such uncertainties are prevalent during solid/liquid transitions rather than solid-state transformations.

5.4 Calorimetric Studies of Recrystallization

5.4.1 DSC Sample Preparation

Samples for the DSC measurements were cut from the cold rolled strips in the form of rectangular sections using a low speed cut-off wheel to minimize the introduction of additional deformation. The samples were of a uniform thickness and flat outer surfaces. This assured a good contact with the aluminum pans and minimized the development of thermal gradients during linear heating. The samples' masses were confined to 45-55 mg depending on their initial thickness and the imposed volume constraint of the aluminum pans. Such small sample size allows for a better temperature resolution by decreasing the response time of the measuring equipment. In order to study the precipitation reactions in the investigated alloys, DSC samples were also prepared from the solution heat treated alloys prior to rolling. The scans for such samples were performed immediately after quenching to avoid any natural ageing effects. For all the calorimetric runs, high purity aluminum samples previously annealed for 2 hours at 430 °C were used as reference material. To maintain the thermal balance between the calorimetric cells, the weights of the reference samples were quite similar to the alloy samples with a maximum variation of $\pm 5\%$.

5.4.2 Procedures

DSC investigations of the solutionised and deformed samples were carried out non-isothermally using a Perkin-Elmer Pyris Diamond DSC with a sensitivity of 0.2 μW . The runs were conducted under a dynamic argon atmosphere at constant heating rates of 40, 45, 50, 55, 60, 70 and 80 $^{\circ}\text{C}/\text{min}$. The employed temperature program for each sample consisted of two heating cycles from 70 to 550 $^{\circ}\text{C}$ at each of the above heating rates with an intermediate cooling cycle at 20 $^{\circ}\text{C}/\text{min}$. It is essential to note that heating rates such as 70 and 80 $^{\circ}\text{C}/\text{min}$ are generally unfavorable in terms of kinetic analysis. Nevertheless, they were employed in order to minimize recovery which is expected to be kinetically limited at such heating rates.

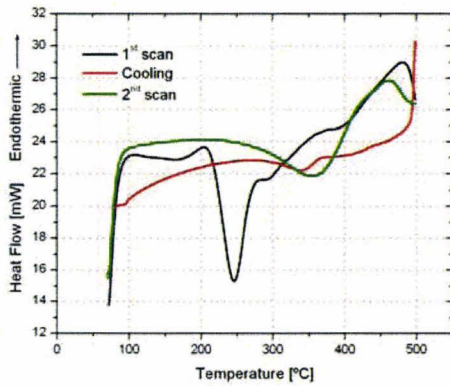
During the DSC scans samples and reference material were placed in previously annealed standard aluminum pans and were covered with platinum lids. The instrument was calibrated for temperature and energy (heat flow) measurements by running a high purity indium sample. Calibration was performed for each employed heating rate and was checked prior to every DSC scan with the onset of melting and the heat of fusion of pure indium and zinc. If the melting point temperature and enthalpy variations exceeded 1% and 5%, respectively, recalibration of the DSC was performed.

5.4.3 Identification of Thermal Events

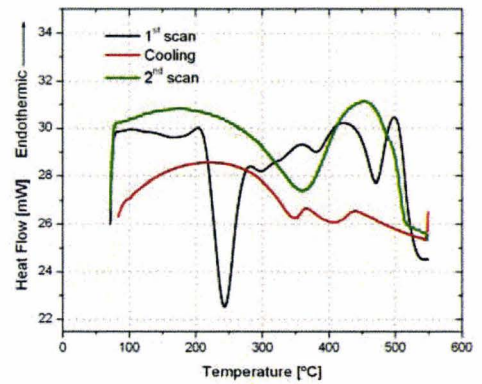
Differential scanning calorimetry is a technique for measuring the power required to establish a nearly zero temperature difference between a sample and a reference material subjected to an identical temperature program (Vyazovkin and Wight, 1997).

The power added or subtracted is a direct measurement of the difference between the heat capacities of both samples. Since, recrystallization is a thermally activated reaction, heat capacity changes in a deformed sample will be reflected on the DSC thermogram as an exothermic peak provided that the reference sample does not undergo the same reaction. It was initially intended to apply canonical methods proposed by Andersen and Jensen (1984) for both the isolation of the energy release events occurring during the anisothermal anneal of the deformed samples and the construction of the baseline (see section 5.3.3). However, the DSC traces for all the investigated alloy compositions showed a sequence of precipitation reactions taking place during the cooling cycle in the calorimeter prior to the second linear heating scan. This is shown in Figure 5.4 for representative samples for the different alloy compositions. It is clear that the signal evolution during the second heating scan is greatly influenced by the thermal events occurring during the cooling cycle.

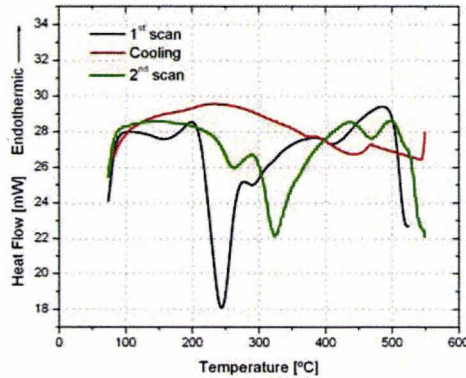
Due to intricate sample removal procedure from the calorimeter, a rapid water quench of the samples at the end of the first heating scan is practically impossible. Consequently, such method is not recommended for heat-treatable aluminum alloys. Alternatively, the DSC scans for cold rolled samples were directly compared to scans for solution heat treated then quenched samples. By correlating the occurring precipitation reactions with available fingerprints from the literature, the recrystallization thermal event (i.e. the recrystallization peak) would be distinguished from other precipitation reactions taking place during the non-isothermal anneal.



(a)



(b)



(c)

Figure 5.4: Successive DSC scans of deformed Al–Mg–Si–Cu samples illustrating the inapplicability of canonical methods to calorimetric recrystallization studies: a) 6111-NC-90, b) 6111-HC-90 and c) 6111-LC-90.

Despite the fact that the first differential power scanning calorimeter with a twin design was developed for the measurement of heat released among annealing plastically deformed copper (Hemminger and Höhne, 1984), and that DSC techniques have been intensively applied in studies of precipitation reactions in aluminum alloys, the use of DSC for the investigation of recrystallization processes has been rather limited. The reason lies in low specific enthalpies, which requires highly sensitive devices. The

calculation of the baseline for recrystallization studies is also a limiting factor towards a quantitative assessment of the reaction. For small detected signals, the use of an experimental baseline becomes misleading. The reproducibility of the scans and the drift of the baseline during the repeat run may lead to spurious effects overlapping with the real transformation signals (Riontino et al., 2005). Therefore, optimization of the baseline is a crucial step for a proper assessment of the recrystallization reaction. For this reason, a new method for baseline construction was developed for this study. The method is explained in detail in section 5.4.4.1.

5.4.4 Quantitative Analysis of the Calorimetric Data

After isolating the portion of the DSC thermogram pertaining to the recrystallization of the deformed alloy from other occurring thermal events, further processing of the calorimetric data in the vicinity of this peak is required in order to obtain necessary information regarding the recrystallization phenomenon. The two quantities of concern are the stored energy of deformation and the degree of recrystallization. In DSC, the heat evolved during linear heating is a direct measurement of the enthalpy of the phase transition. In the case of annealing of deformed metals, this reflects the stored energy of deformation. Hence, by employing equation (5.6) the stored energy can be directly obtained. For experiments conducted at a constant heating rate, the heat evolving from the sample per unit time is assumed proportional to the reaction rate following the Borchardt and Daniels assumption $\frac{dH}{dt} \propto \frac{d\alpha}{dt}$ (Henderson, 1979; García-

Cordovilla and Louis, 1986). Hence, the time dependence of energy release is a direct measurement of the extent of reaction following the expression:

$$\alpha_i = H_i/H \quad (5.8)$$

where, α_i is the fraction of transformation completed at time i , H_i is the partial heat of reaction at time i and H the total heat of reaction. Solution of both these equations entitles a well constructed baseline. The following section describes the details of a novel baseline construction method developed by Malakhov and Abou Khatwa (2007). The same procedures were used for the analysis of the recrystallization peak area in this study.

5.4.4.1 A Novel Baseline

It should firstly be recalled that $dH/dt = 0$ if $t \leq t_{\text{beg}}$, which means that the position of the baseline prior to the transformation coincides with \dot{Q} . If $t \geq t_{\text{end}}$, then $dH/dt = 0$ and the location of the baseline after the transition is indistinguishable from \dot{Q} . Secondly, since an extent of the transformation at any time between t_{beg} and t_{end} is deemed directly proportional to energy consumed for driving the transformation by this time, then contributions from the initial and final states to the baseline can be related to a degree of the transformation (Hemminger and Höhne, 1984):

$$\begin{aligned}
 g(t) &= \left(1 - \frac{\int_{t_{\text{beg}}}^t (\dot{Q}(\tau) - g(\tau)) d\tau}{\int_{t_{\text{beg}}}^{t_{\text{end}}} (\dot{Q}(\tau) - g(\tau)) d\tau} \right) \times g(t_{\text{beg}}) + \frac{\int_{t_{\text{beg}}}^t (\dot{Q}(\tau) - g(\tau)) d\tau}{\int_{t_{\text{beg}}}^{t_{\text{end}}} (\dot{Q}(\tau) - g(\tau)) d\tau} \times g(t_{\text{end}}) \\
 &= g(t_{\text{beg}}) + \frac{g(t_{\text{end}}) - g(t_{\text{beg}})}{\int_{t_{\text{beg}}}^{t_{\text{end}}} (\dot{Q}(\tau) - g(\tau)) d\tau} \times \int_{t_{\text{beg}}}^t (\dot{Q}(\tau) - g(\tau)) d\tau
 \end{aligned} \tag{5.9}$$

However, equation (5.9) cannot be solved with respect to $g(t)$ merely because it is not even clear what class of function the solution should be sought within.

A discrete nature of calorimetric observations should not shade the fact that heat flux and the baseline are smooth functions. Let us accept that they both belong to the $C^2(t_1, t_n)$ class of twice continuously differentiable functions. In this case, the discrete representation of heat flux can easily be converted to an analytical description by constructing an interpolating cubic spline $\dot{Q}(t)$ (Appendix I explains how to calculate the spline). Although the spline can describe the whole array of experimental data points, only its portion corresponding to the thermal event (*i.e.* to the peak) is useful. Similarly, the baseline can be represented by an interpolating cubic spline $g(t)$. While constructing the baseline, one should keep in mind that the spline $g(t)$ must comply with the following conditions:

1. At the beginning of the transformation, the baseline coincides with the flux curve:

$$g(t_{\text{beg}}) = \dot{Q}(t_{\text{beg}}). \text{ Since no drastic deviations of the baseline from } \dot{Q}(t) \text{ are expected}$$

in the very beginning of the transformation, it is assumed that slopes (but not curvatures!) of the two splines are the same: $(dg/dt)_{t=t_{\text{beg}}} = (d\dot{Q}/dt)_{t=t_{\text{beg}}}$.

2. At the very end of the transition, the baseline smoothly approaches the flux curve:

$$g(t_{\text{end}}) = \dot{Q}(t_{\text{end}}), (dg/dt)_{t=t_{\text{end}}} = (d\dot{Q}/dt)_{t=t_{\text{end}}}.$$

3. Expression (5.9) must be satisfied in all experimental points situated between t_{beg} and t_{end} . In other words, if t_{beg} corresponds to the point number i_{beg} , and t_{end} corresponds to point number i_{end} , then (5.9) must be valid in $i_{\text{end}} - i_{\text{beg}} - 1$ points between them:

$$g(t_i) = g(t_{\text{beg}}) + \frac{g(t_{\text{end}}) - g(t_{\text{beg}})}{\int_{t_{\text{beg}}}^{t_{\text{end}}} (\dot{Q}(\tau) - g(\tau)) d\tau} \times \int_{t_{\text{beg}}}^{t_i} (\dot{Q}(\tau) - g(\tau)) d\tau, i = i_{\text{beg}} + 1, \dots, i_{\text{end}} - 1 \quad (5.10)$$

Since modern calorimeters are usually equipped with data acquisition systems capable of registering heat flux frequently (several times per second), expression (5.10), which is much easier to handle computationally, is a virtual twin of (5.9).

Based on the above conditions, an algorithm for constructing the spline $g(t)$ representing the integral baseline is presented below:

1. Choose an experimental point i_{beg} associated with the onset of transformation (if necessary, visualize calorimetric data). Estimate the slope of the flux curve at this point (employ, for instance, a simple linear regression for this purpose). Pick up an experimental point i_{end} corresponding to the end of transition and evaluate the slope at it. These first derivatives of the heat flux with respect to time are always used as

boundary conditions needed for constructing splines. The first step of the algorithm is illustrated in Figure 5.5. It should be accentuated that since a cubic spline is a local interpolant (see Appendix I), there is no need for very accurate estimations of slopes.

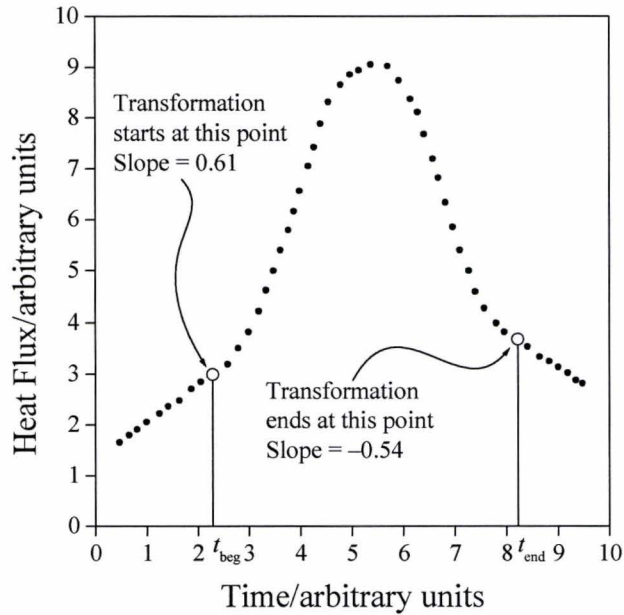


Figure 5.5: Points corresponding to the onset and finish of a transformation and estimated slopes at these points.

2. Use the experimental quantities $t_i, \dot{Q}_i, i = i_{\text{beg}}, \dots, i_{\text{end}}$ along with the boundary conditions for constructing the spline $\dot{Q}(t)$. Once built, this spline remains intact for the rest of calculations. This step is exemplified in Figure 5.6.

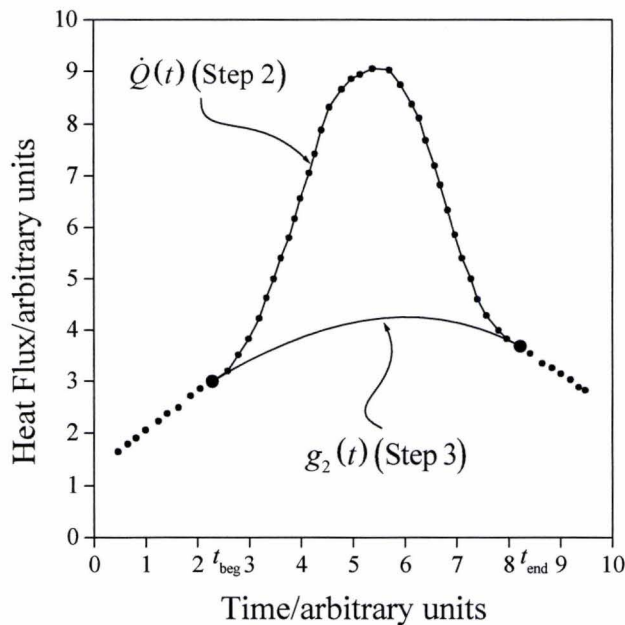


Figure 5.6: Experimental points and the slopes are used for building a spline describing the heat flux curve and a spline $g_2(t)$ connecting the first and last points of the peak.

3. Using the values of heat flux and its first derivatives at the knots $t_{i_{beg}}$ and $t_{i_{end}}$ build the spline $g_2(t)$ ($g_2(t)$ is used instead of $g(t)$ for emphasizing that only two experimental measurements have been used for constructing the spline). Although $g_2(t)$ satisfies the first and second conditions formulated above ($g_2(t)$ and $\dot{Q}(t)$ have the same slopes in the first and last knots), it cannot be guaranteed that condition (5.10) is fulfilled. An example of the $g_2(t)$ spline is presented in Figure 5.6. It is worth highlighting that a function identical to $g_2(t)$ was identified with the baseline by Van der Plaats (1984).

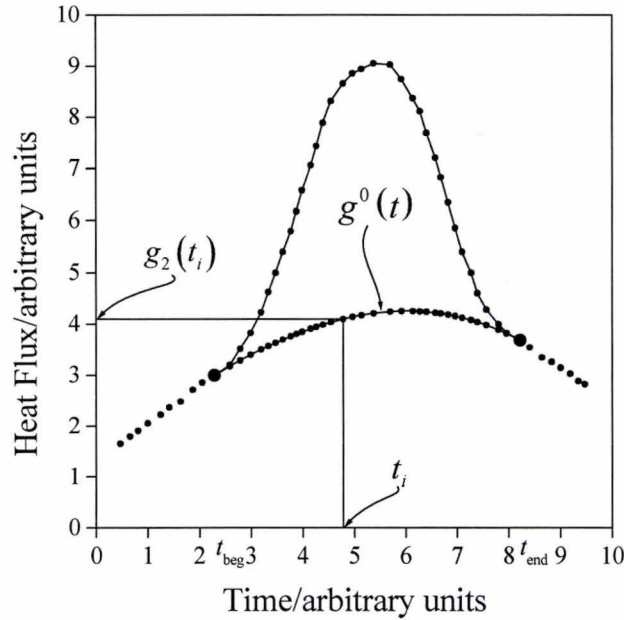


Figure 5.7: Calculated $g_2(t)$ in all peak points are used for building an initial approximation to a baseline.

4. Having the analytical description $g_2(t)$, calculate $g_2(t_i)$, $i = i_{\text{beg}} + 1, \dots, i_{\text{end}} - 1$. After that, use the quantities $t_i, g_2(t_i)$, $i = i_{\text{beg}}, \dots, i_{\text{end}}$ along with the fixed slopes in the first and last knots (these first derivatives, which are fixed once and forever, are always utilized for setting boundary conditions) for building the spline $g^0(t)$. The upper index k in $g^k(t)$ symbolizes the number of iteration undertaken so far for approaching the solution. While $g^0(t)$ is indistinguishable from $g_2(t)$, the former spline has the same number of knots as $\dot{Q}(t)$. The spline $g^0(t)$ is shown in Figure 5.7.

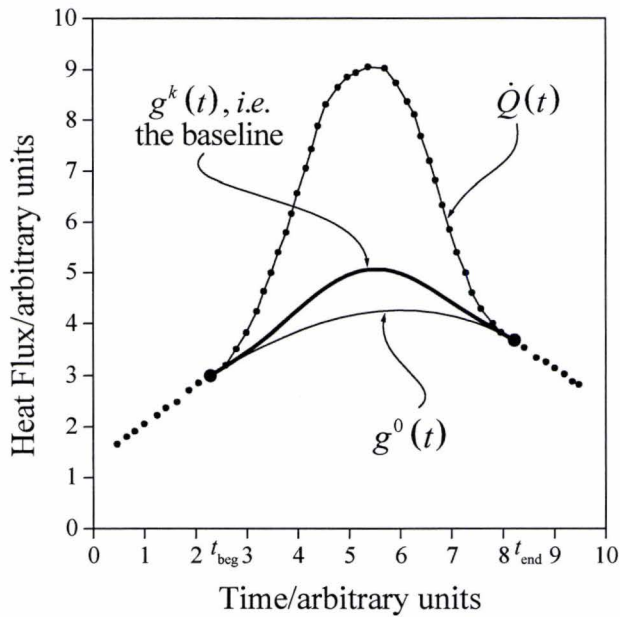


Figure 5.8: Iterations resulting in a self-consistent baseline.

5. Since both $\dot{Q}(t)$ and $g^0(t)$ are pieces of cubic polynomials smoothly glued together in the knots, taking integrals in (5.10) is trivial. Compute all $i_{\text{end}} - i_{\text{beg}} - 1$ left-hand-sides of (5.10) and calculate corresponding entities in right-hand-sides. Use the latter values along with known and fixed boundary conditions for building $g^1(t)$.
6. Continue refining the spline by invoking (5.10) until the following condition is satisfied:

$$\frac{|g^k(t_i) - g^{k-1}(t_i)|}{1 + \min(|g^k(t_i)|, |g^{k-1}(t_i)|)} \leq \varepsilon, \forall i = i_{\text{beg}} + 1, \dots, i_{\text{end}} - 1 \quad (5.11)$$

Once (5.11) is respected, $g^k(t)$ is the baseline (depicted in Figure 5.8) whose determination was the sole objective of all preceding computations. The criterion (5.11) recommended by Gill et al. (1981) bears features of both absolute and relative

accuracies. If the heat flux is small, (5.11) reduces to $|g^k(t_i) - g^{k-1}(t_i)| \leq \varepsilon$, *i.e.* to a criterion based on absolute accuracy. If the heat flux is large, (5.11) becomes

$$\frac{|g^k(t_i) - g^{k-1}(t_i)|}{\min(|g^k(t_i)|, |g^{k-1}(t_i)|)} \leq \varepsilon, \text{ which is a criterion based on relative accuracy.}$$

The above proposed method of constructing a baseline for the case when a degree of transformation is directly proportional to heat consumed or released has three distinctive features. Firstly, it is assumed that both a directly measured calorimetric signal and a corresponding baseline are smooth functions of time. In addition to this assumption, which is not difficult for the calorimetric community to accept, no further simplifications are employed. Moreover, the approach is free from such “numerically fragile” undertakings as extrapolating a polynomial description of heat capacity into the peak range (Van der Plaats, 1981; Hemminger and Sarge, 1991).

Secondly, the iterative procedure described above leads to the integral baseline satisfying condition (5.9). This circumstance along with the fact that the baseline is indistinguishable from a heat flux curve before and after the transformation makes the baseline self-consistent.

Thirdly, the suggested method of constructing the integral baseline is very simple to apply in practice. This straightforwardness stems from utilizing interpolating cubic splines for representing both the peak and baseline. In contrast to a habitual interpolating polynomial, a spline is a local interpolant. Thus it connects experimental points without having aphysical behavior between them. If experimental data are noisy, then

approximating (smoothing) splines can be considered, but a necessity to choose a smoothing parameter makes the approach less universal and more computationally cumbersome. It is worth mentioning that splines describing the peak and baseline are never differentiated, they are only integrated, which ensures a computational robustness of the method.

The above algorithm was implemented in a FORTRAN source code that was used for the analysis of the recrystallization peak. The program evaluates the progress of recrystallization with time and/or temperature and the stored energy of deformation.

5.5 Grain Structure Examination

5.5.1 Optical Microscopy

In order to validate the DSC results, the evolution of the microstructure during annealing was observed by optical microscopy. Longitudinal-Transverse (L-T) sections were cut from the rolled sheets using a precision table top cut-off Accutom 2 machine. The DSC temperature program employing a heating rate of 40 °C/min was simulated using a tube furnace, and samples were quenched from temperatures corresponding to the thermal events reflected by the DSC thermogram. A K-type thermocouple was embedded with the samples to accurately document the temperature by the aid of data acquisition software. Samples were then cold mounted in epoxy resin and were mechanically ground on SiC paper to a grit size of 2400. Polishing was then carried out on a MD Mol cloth with 3 µm diamond suspension and a MD cloth with 1 µm diamond suspension. Final

polishing was then performed on a MD cloth using 0.05 μm colloidal silica solution. After polishing the samples were etched from 5 to 60s in Keller's Reagent (950 ml distilled water + 10 ml HF conc. + 15 ml HCl conc.+ 25 ml HNO₃ conc.) followed by desmutting in a 50% HNO₃ solution for about 15 seconds. The images obtained from such conventional metallurgical techniques were mainly suitable for a qualitative assessment of the grain structure. A better method would have been the use of electrolytic etching and examining the grain structure under polarized light. However, due to the increased Cu content ($> 0.3\%$) of the alloys such method is unsuitable. As an alternative, orientation image maps were employed for the quantitative assessment of the recrystallized microstructures by electron back scatter diffraction.

5.5.2 Electron Back Scatter Diffraction (EBSD)

Specimens for the EBSD investigation were cut from deformed sheets to expose an internal longitudinal (RD/ND) section. They were then annealed in a tube furnace to temperatures corresponding to the end of the recrystallization peak observed on equivalent DSC thermograms. Samples were prepared for electron microscopy by cold mounting in conductive molds (epoxy resin + Ni powder) and subsequently grinding and polishing in similar steps as the optical microscopy investigation. In order to assure a mirror-finished scratch-free surface, final polishing with colloidal silica was executed for 2 hours on a vibratory polisher (Buehler Vibromet). The EBSD investigation was conducted using a Philips XL30 SEM with a field emission gun (FEG) operated at 20kV with a beam step size of 1 μm . Orientation mapping, quantitative metallography and

texture analysis of EBSD data was performed using the VMAP software (Humphreys, 2002).

5.6 Hardness Measurements

The softening behavior of the material was assessed by microhardness measurements conducted using a Leco M-400-HZ digital hardness tester with a Vickers indenter. The hardness values were obtained with a direct load of 100 g applied for 10 seconds. Each reported hardness value represents the average of ten reading equally spaced along the mid section of the samples. Samples for the hardness measurements represented L-T sections from the rolled slabs that were subsequently annealed in the tube furnace. They were cold mounted in an epoxy resin and then ground and polished in a similar manner to the procedure outlined for optical microscopy, but excluding the fine polishing step using colloidal silica.

5.7 Transmission Electron Microscopy

The deformed and annealed microstructures were characterized by TEM. This included monitoring the evolution of precipitates during linear heating. Thin foils for TEM observations were produced from rolled and annealed sheets by electropolishing in a methanol solution containing 30 vol.% nitric acid at a temperature ranging from -35 to -55 °C, and a voltage of 30 V using a TenuPol-5 apparatus. Samples were inspected using

both dark field and bright field imaging modes in a Philips CM 12 transmission electron microscope operating at 120 KeV.

CHAPTER 6

Kinetic Modeling of Recrystallization

As discussed in the previous chapter, there have been tremendous efforts for modeling the recrystallization kinetics. A majority of these efforts has been focused on isothermal experimental conditions due to availability of simple mathematical models allowing a straight forward analysis of experimental results. Despite the criticism directed towards the JMAK treatment of transformation kinetics, this method still remains the center upon which many modeling efforts evolve. The reason lies in the simplicity of the analytical derivation and an ability to give a broad picture of the overall transformation kinetics.

For more than four decades now, the scientific community has been relying on thermal analysis for predicting reaction rates of solid-liquid and solid-solid transformations. Differential scanning calorimetry (DSC) is a core thermoanalytical technique whose continuous advancement over the past years has contributed to an increasing popularity of its use and application to a wide variety of materials and substances. This in turn triggered the development of advanced theories and experimental techniques for a non-isothermal experimental analysis of phase transformations. The aim of this chapter is to describe how thermal analysis has been employed in investigating the

kinetics of recrystallization in the Al–Mg–Si–Cu alloys. The chapter starts with a brief description of the solid-state reaction kinetic theory and commonly used methods for extracting kinetic parameters. The use of the JMAK equation under non-isothermal experimental conditions will then be addressed. Finally, the procedures employed for data treatment and the devised kinetic modeling will be described.

6.1 Solid-State Reaction Kinetics from Thermal Analysis

The first step of a kinetic study is the measurement of a fractional reaction (also called an extent of reaction) α as a function of time at constant temperature (isothermal method), or as a function of temperature (dynamic method). A kinetic analysis is then carried out by relating the experimental results to a rate equation for processes such as nucleation, growth and diffusion. The general rate expression for condensed-state processes derived from different models is described in differential and integral forms by the following expressions (Vyazovkin and Wight, 1997; Brown, 2001; Simon, 2004):

$$d\alpha/dt = k(T)f(\alpha) \quad (6.1)$$

$$g(\alpha) = \int_0^{\alpha} [f(\alpha)]^{-1} d\alpha \quad (6.2)$$

where $f(\alpha)$ and $g(\alpha)$ are the conversion functions pertaining to a specific process model (i.e. reaction model), and k is a rate coefficient which takes into account the effect of temperature through the use of the Arrhenius equation (equation (4.7)). The functions

$k(T)$ and $f(\alpha)$ are assumed to be independent of each other. The rate equation can then be expressed as:

$$d\alpha/dt = k_0 \exp(-E/RT) f(\alpha) \quad (6.3)$$

For dynamic measurements, the explicit time dependence of the rate equation can be eliminated (Vyazovkin and Wight, 1997; Brown, 2001):

$$d\alpha/dT = (d\alpha/dt) \times (dt/dT) = (d\alpha/dt) \times (1/\beta) = (k_0/\beta) \exp(-E/RT) f(\alpha) \quad (6.4)$$

where $\beta \equiv dT/dt$ is the heating rate. Rearranging the variables and integrating the above expression leads to:

$$\int_0^\alpha (1/f(\alpha)) d\alpha = \int_{T_0}^T (k_0/\beta) \exp(-E/RT) dT \quad (6.5)$$

$$g(\alpha) = \int_{T_0}^T (k_0/\beta) \exp(-E/RT) dT = \int_0^T (k_0/\beta) \exp(-E/RT) dT \quad (6.6)$$

Thus, the global reaction kinetics is given via the kinetic triplet: the reaction model $g(\alpha)$ and the Arrhenius parameters k_0 and E . Solving (6.6) requires an evaluation of the

temperature integral, i.e. $\int_0^T \exp(-E/RT) dT$. This integral does not have an exact

analytical solution but can be evaluated by using the exponential integral function. This is done either by expanding the integral in an infinite gamma series or by using approximations with a finite number of terms of the asymptotic expansion (Starink, 2004). Errors introduced from such approximations are usually small in comparison with experimental errors and uncertainties in the kinetic model (Doyle, 1961). As a first step, a

new variable $y = E/RT$ is introduced, which leads to the following expression (Brown, 2001; Starink, 2004):

$$\int_{T_0}^T \exp(-E/RT) dT = (E/R) \int_y^{\infty} (\exp(-y)/y^2) dy = (E/R) p(y) \quad (6.7)$$

If heating starts at a low temperature at which the rates of nucleation and growth are both negligible, the lower limit of the integral T_0 can be replaced with zero, and integration of the right hand side is then performed between y and ∞ (Yinnon and Uhlmann, 1983; Flynn, 1997). A substitution of (6.7) in (6.6) yields:

$$g(\alpha) = (k_0 E/R\beta) p(y) \quad (6.8)$$

Various approaches have been proposed in literature for finding approximations to the integral $p(y)$ and assessing their accuracies (Flynn, 1997; Starink, 2004). An analysis of these approximations is beyond the scope of this research. However, it is worth noting a frequently used Doyle approximation which is also the basis for a widely used Flynn-Wall-Ozawa isoconversional method discussed later in section 6.1.2. In this approximation, the integral in (6.7) is expanded, which leads to the following expression (Doyle, 1961):

$$\int_y^{\infty} (\exp(-y)/y^2) dy = \exp(-y)/y - \int_y^{\infty} (\exp(-y)/y) dy \quad (6.9)$$

The integral in the right hand side is then approximated by the asymptotic series, in which only the first two terms are kept:

$$\int_y^{\infty} (\exp(-y)/y) dy \cong \exp(-y) \left(\frac{1}{y} - \frac{1!}{y^2} + \dots \right) \quad (6.10)$$

Substituting (6.9) and (6.10) in equation (6.8) yields (Brown, 2001; Starink, 2004):

$$g(\alpha) \cong (k_0 E / R \beta) \left(\frac{\exp(-y)}{y^2} \right) \quad (6.11)$$

The unknowns in (6.11), i.e. k_0 , E and the conversion function $g(\alpha)$ or $f(\alpha)$, can be evaluated from isothermal or non-isothermal experimental measurements of α and/or $d\alpha/dt$. A critical assumption employed in the procedure described is that the reaction mechanism does not change. If this assumption is doubtful, then the kinetic analysis has to be modified by introducing functions relating the dependencies of the conversion function and the Arrhenius parameters on α (Brown, 2001). An important and regretful limitation of the technique outlined is its inability to identify and separate elementary reactions of actual physical processes. Thus, only an overall process rate is measurable. Consequently, experimentally evaluated Arrhenius parameters are effective (apparent) quantities. By adopting such effective criterion, concerns pertaining to the applicability of the Arrhenius equation to solid-state reactions are eradicated (Vyazovkin and Wight, 1997).

6.1.1 Isothermal Kinetic Analysis

An isothermal kinetic analysis is based on the assumption that a single rate expression and a single set of Arrhenius parameters are operative within the whole range of α values. Experimental data are then fitted to a set of kinetic model functions until a

statistically satisfactory match is obtained. The activation energy and the preexponential factor are then determined from the Arrhenius plots provided that the form of the conversion function remains the same for a series of isothermal temperatures. The Arrhenius parameters found in such manner are quantities averaged over the whole extent of the reaction, i.e. $0 \leq \alpha \leq 1$ (Tanaka, 1995; Brown, 2001).

The isothermal kinetic analysis can also be used to obtain values for the activation energy at a given fractional conversion for experiments conducted at different temperatures. By combining equations (6.2) and (6.3) for a constant temperature, the following expression is obtained (Tanaka, 1995; Simon, 2004; Starink, 2004):

$$\ln t_{\alpha} = \frac{E_{\alpha}}{RT} + \ln \left[\frac{g(\alpha)}{A} \right] = \frac{E_{\alpha}}{RT} + C \quad (6.12)$$

It is clear from (6.12) that the activation energy could be evaluated from the slope of a plot of $\ln t_{\alpha}$ vs. $1/T$.

6.1.2 Non-Isothermal Kinetic Analysis

Non-isothermal kinetic analysis methods are conventionally classified according to the type of experimental data used. This classification comprises differential methods employing equation (6.4) or integral methods based on equation (6.6). Other alternative classifications are based on the method of calculation of the kinetic parameters and are divided into discrimination methods concerned with the identification of the kinetic model $g(\alpha)$ or $f(\alpha)$ and non-discriminatory methods known also as model-free or

isoconversional methods. The discrimination methods are subject to significant errors in predicting reaction rates outside experimentally investigated temperature ranges and do not offer any insights towards the reaction mechanism (Vyazovkin and Wight, 1997). Moreover, an applicability of the discrimination methods to non-isothermal data is highly questionable. An underlying procedure for such methods involves a determination of $k(T)$ from a selected conversion function $f(\alpha)$. However, information on these two functions cannot be separated under non-isothermal conditions and many selections of $f(\alpha)$ will satisfy fit experimental data through variations in the Arrhenius parameters. Thus, non-unique kinetic parameters will be derived and will compensate for differences between the assumed conversion function $f(\alpha)$ and the true kinetic model (Brown, 2001; Vyazovkin and Wight, 1997). Such effect is known as the kinetic compensation effect and will be discussed later in details. The discrimination methods also result in the evaluation of a single pair of Arrhenius parameters despite the fact that most solid-state reactions are usually combinations of elementary steps and, therefore, variations of the Arrhenius parameters with the extent of conversion is expected (Vyazovkin and Wight, 1997).

On the other hand, the isoconversional methods eliminate the unknowns from the kinetic model $g(\alpha)$ or $f(\alpha)$ by comparing the experimental results for identical values of α obtained at different heating rates or at the maximum rate of conversion (Brown, 2001; Ozawa, 1992). An underlying assumption in such methods is that the rate of the

reaction at a constant extent of conversion is a sole function of temperature following the expression:

$$\left[\frac{d \ln(d\alpha/dt)}{dT^{-1}} \right]_{\alpha} = -E_{\alpha}/R \quad (6.13)$$

Integration of the above equation leads to:

$$\ln(d\alpha/dt)_{\alpha} = -E_{\alpha}/RT + \text{constant} \quad (6.14)$$

An alternative approach is based on integrating equation (6.6) and using an approximation for the temperature integral, which yields:

$$\ln(\beta) = \text{constant} - E_{\alpha}/RT_{\alpha} \quad (6.15)$$

Thus, model-independent estimates of the activation energy are evaluated and the dependence of E_{α} on α is established giving an indication towards the kinetics of the process (Vyazovkin and Wight, 1997).

A major difficulty to determine the activation energy by applying the methods discussed above is a necessity to identify an equivalent stage of the reaction for various heating rates. In his original derivation of a particular isoconversional method, Kissinger assumed that the maximum reaction rate is associated with the temperature of the maximum deflection in differential thermal analysis (Kissinger, 1957). Hence, the stage of the reaction at such temperatures can be considered identical and independent of the heating rate. Later, this consideration was generalized to include any fixed amount of transformation associated with a fixed amount of heat evolution (Ozawa, 1992; Starink, 2004).

Numerous methods invoked for non-isothermal kinetic modeling are usually classified into three main categories according to their reliability: the Flynn-Wall-Ozawa method, the expanded Freidman method and the Kissinger-Akahira-Sunose method. A comprehensive review of their development can be found in the work of Ozawa (1992). An interesting fact about these methods is that they all share common features and can be derived from a common fundamental equation which includes the so-called reduced time. Such common derivation, as outlined below, accounts for both the wide applicability and the increased reliability of these methods (Ozawa, 1992; Tanaka, 1995).

The fundamental equation is:

$$\alpha = F(\theta) \quad (6.16)$$

where α is the fractional reaction and $F(\theta)$ is an eigen-valued function of the reduced time θ , which is defined by:

$$\theta = \int_0^t \exp(-E/RT) dt \quad (6.17)$$

If it assumed that the Arrhenius law holds for solid-state reactions and that the reaction proceeds through a single elementary process, then $F(\theta)$ is constant at a given fractional reaction α . For a constant heating rate β , θ is given by:

$$\theta = \frac{E}{\beta R} p(y) \left(\frac{E}{RT} \right) \quad (6.18)$$

where $p(y)$ is the temperature integral that can be approximated by one of the following expressions (Doyle; 1961):

$$\log p(y) = -2.315 - 0.4567y \text{ for } 20 \leq y \leq 60 \quad (6.19)$$

$$p(y) = \frac{\exp(-y)}{y^2} \text{ for } 20 \leq y \leq 50 \quad (6.20)$$

By using equation (6.19) one arrives at the Flynn-Wall-Ozawa method:

$$\log \beta + 0.4567 \left(\frac{E}{RT} \right) = \text{constant} \quad (6.21)$$

If (6.20) is employed, then the Kissinger-Akahira-Sunose method can be derived:

$$\frac{\ln \beta}{T^2} + \frac{E}{RT} = \text{constant} \quad (6.22)$$

Therefore, the plots of $\log(\beta)$ or $\ln \beta/T^2$ versus the reciprocal absolute temperature should be linear with the slope equal E/RT .

The remaining expanded Friedman method can be derived by differentiation equation (6.16) leading to:

$$\frac{d\alpha}{d\theta} = F'(\theta) \quad (6.23)$$

At a given fractional conversion, $d\alpha/d\theta$ is constant and thus:

$$\frac{d\alpha}{d\theta} = \frac{d\alpha}{dt} \frac{dt}{d\theta} = \frac{d\alpha}{dt} \exp\left(\frac{E}{RT}\right) = \text{constant} \quad (6.24)$$

Therefore, $d\alpha/dt \propto \exp(-E/RT)$ and the plot of $\ln(d\alpha/dt)$ vs. $1/T$ should be linear.

An important advantage of the expanded Friedman method is its applicability to any thermal analysis data regardless of the temperature program. However, since it employs instantaneous rate values, it is badly affected by an experimental noise, which makes the method numerically unstable (non-robust). It was sagaciously concluded that preference

should be given to the integral methods (Brown, 2001; Simon, 2004). It is instructive to note that when the activation energy depends on the degree of conversion, inconsistencies between the differential and integral methods are observed (Budrugeac et al., 2001). It should be admitted that the accuracy of the integral methods depends on the accuracy of various approximations employed to handle the temperature integral. Following the determination of the activation energy by isoconversional methods, complete determination of the kinetic triplet is achieved by selecting a reaction model that fits best the experimental data.

The time-temperature dependence of the degree of conversion α in dynamic experiments, has cast doubts regarding the applicability of the general rate expression (6.1) to the kinetic analysis of non-isothermal data. This led some authors to reject such formalism and to propose an alternative approach to non-isothermal kinetic analysis based on the relation:

$$\alpha = f(t, T(t)) \quad (6.25)$$

According to the rules of chain differentiating, the actual rate in non-isothermal measurement can be expressed as:

$$\frac{d\alpha}{dt} = \left. \frac{\partial \alpha}{\partial t} \right|_T + \left. \frac{\partial \alpha}{\partial T} \right|_t \frac{dT}{dt} \quad (6.26)$$

It was claimed that the first term in the right hand side of (6.26) represents the isothermal kinetic equation. It has been shown that such approach is inapplicable to the cases when the fraction transformed depends on the $T(t)$ relationship, i.e. on the path. Moreover, the

ambiguous physical meaning of the change of the degree of conversion with temperature when time is kept constant has led to a consensus to avoid the use of such approach in kinetic analysis (Kemeny, 1987).

6.2 Applicability of the Johnson-Mehl-Avrami-Kolmogorov (JMAK) Model to Non-Isothermal Kinetic Analysis

The JMAK model was originally developed for isothermal transformations. Hence, its application under non-isothermal conditions entails that the transformation rate should be independent of the thermal history. In addition, the characteristic kinetics of phase change at any temperature should be the same with only a difference in the time scale. These conditions are applicable in the isokinetic range identified by Avrami (1939) where nucleation and growth rates are proportional and independent of temperature (Cahn, 1956; Zhang and Mitchell, 2000; Ruitenberget al., 2001). Single thermally activated processes are said to exhibit an isokinetic relation (related to a single activation energy). However, nucleation and growth reactions generally show an approximate isokinetic behavior (Starink, 2004). In such isokinetic range, the transformation is additive and any stage for a dynamic transformation is obtained by summing a number of time fractions to reach an equivalent stage under isothermal conditions as expressed by the relation (Zhang and Mitchell, 2000):

$$\int_0^t dt/t_a(T) = 1 \quad (6.27)$$

where t is the non-isothermal time to a fixed fraction of transformation α_a , and $t_a(T)$ is the isothermal time to α_a . In addition to the above restrictive limitation of proportionality between the nucleation and growth rates, the non-isothermal JMAK rate equation can still be employed in cases where the transformation is additive regardless of independent variations of nucleation and growth rates with temperature. Cahn (1956) suggested a less restrictive additivity condition. He proposed that transformed fractions are additive for any transformation where the reaction rate depends solely on the state of the assembly regardless of the thermal pass leading to such state. A pertinent example here would be a site-saturated nucleation when the transformation rate depends only on the fraction transformed and temperature (Henderson, 1979; Zhang and Mitchell, 2000). The condition of site-saturation not only addresses the problem of the reaction additivity, it also eliminates doubts that may arise as the result of a habitually assumed Arrhenian temperature dependence of the effective overall reaction rate k . It is argued that such dependence is not expected for both the nucleation and growth rates, but instead is applicable when k depends on the growth rate alone, i.e. negligible nucleation rate (Henderson, 1979; Yinnon and Uhlmann, 1983).

Several methods have been proposed to assess the kinetic parameters under non-isothermal conditions. The pioneering effort by Henderson (1979) was based on a rate equation derived from the differentiation and re-substitution of the isothermal JMAK expression. The resulting relation takes the form (Kemeny and Sestak, 1987):

$$\left[-\ln(1-\alpha)\right]^{1/n} = \int_0^t k[T(t)] dt \quad (6.28)$$

By using an approximation for the exponential integral, the non-isothermal solution was expressed by:

$$\left[\ln(1-\alpha)^{-1}\right]^{1/n} \approx \frac{k_0^{1/n} (T/\beta) \exp(-E/nRT)}{E/nRT + 2} \quad (6.29)$$

Woldt (1992) provided a description for non-isothermal kinetics by expanding the double integral in the general JMAK kinetic equation (6.30), which is valid whatever thermal condition, into a series:

$$X_v = 1 - \exp \left[- \int_0^t f \left[\int_{\tau}^t G \dot{dt}' \right]^m \dot{N} d\tau \right] \quad (6.30)$$

The final expression derived by Woldt was:

$$X_v \approx 1 - \exp \left(K^* \times \left[\frac{T^2}{\beta} \exp \left(-\frac{E}{mRT} \right) \right]^m \right) \quad (6.31)$$

Where K^* represents the pre-exponential factor under non-isothermal conditions while m denotes the growth dimensionality. For continuous nucleation, the Avrami exponent follows from the relation $n = m + 1$, while for site-saturated nucleation n equals m .

Kruger (1993) proposed an alternative method for obtaining non-isothermal kinetics. His approach avoids employing neither a rate equation nor even an approximation for the exponential integral. The method is based on an infinitesimal discretization of continuous time-temperature curves into isothermal steps each of which

obeys the formal JMAK kinetics. The non-isothermal reaction kinetics is then approximated by a superposition of these isothermal steps. It is interesting to notice that the expression derived by Kruger for the non-isothermal transformed fraction was identical to equation (6.28) derived on the basis of a rate equation.

6.3 Activation Energy Determination

Despite numerous investigations focused on the kinetics of solid-state transformations, controversy still surrounds various mathematical models and formalisms used for a kinetic analysis. Usually, a physical meaning of kinetic parameters as well as their interpretation, in general, and their relationship to different reaction mechanisms, in particular, are questioned. In fact, convincing and unambiguous answers to such questions have not been given except for the possible use of the apparent activation energy value and its correlation with established values for thermally activated processes. Therefore, the calculation of a model-independent and effective (apparent) value of the activation energy is considered a crucial step for a proper kinetic analysis. Besides serving as a base value to be compared with results stemming from specific kinetic models, its variation with the degree of conversion may point to operational kinetic processes.

The first step in the present study of the recrystallization kinetics of AA6111 alloys will involve the determination of a model-free estimate of the effective activation energy and its dependence on the degree of conversion. To achieve this goal, the

isoconversion Flynn-Wall-Ozawa method described in section 6.1.2 will be applied to experimental DSC data on the degree of recrystallization. Seven sets of kinetic data obtained at various heating rates ranging from 40 °C/min to 80 °C/min for each alloy will be used. The logarithms of the seven different heating rates will be plotted against the reciprocal temperature for a kinetic interval of conversion ranging from 10% to 90% with incremental steps of 10%. For the different conversion values, straight lines will be fitted by linear regression, after which the activation energy and its dependency on the degree of conversion will be evaluated from the corresponding slopes.

Nowadays, the isoconversion procedures are regarded as the most reliable and robust methods leading to trustworthy kinetic data. A choice of a specific method usually reflects personnel preference of a researcher and particularities of an experimental setup. In this work, the Flynn-Wall-Ozawa method was favored due to the following reasons:

- The Ozawa method is originally derived on the basis of the general kinetic form, while those by Kissinger and Friedman are derived under the assumption of n^{th} order reaction mechanisms and later extended to cover more reaction mechanisms by Ozawa and others (Ozawa, 1984 & 1986).
- The reduced time concept proposed by Ozawa expands the applicability of the isoconversional methods and emphasizes features common to all methods of this family.

- The Flynn-Wall-Ozawa method employs a more accurate approximation of the temperature integral than that used in the Kissinger method.
- The Ozawa method is not limited to single elementary processes. It also holds for nucleation and growth (Ozawa, 1971 & 1984). For crystal growth, equation (6.21) was derived for the case of nucleation from preexisting nuclei, but with negligible concurrent random nucleation. Growth was assumed to occur from impurity or nucleating agents that were independent of the thermal history of the material. A case that resembles site-saturated nucleation of recrystallization.

6.4 Numerical Solution of the Recrystallization Kinetics

6.4.1 Formal JMAK Approach

In order to assess to what extent the JMAK kinetics are applicable to the recrystallization of the alloys of interest, it was decided to start with a numerical solution of the analytical JMAK expression derived for isothermal conditions. By doing so, unnecessary analytical expressions for nucleation and growth rates would be avoided. However, the Arrhenian temperature dependence will still be explicitly assumed as a result of the general additivity rule requirements.

It should be accentuated that a general use of the statistically-best fitting approach to extract kinetic information from non-isothermal experiments is considered erroneous (Vyazovkin and Wight, 1997). This is due to the nature of the non-isothermal experimental data which contains mutual information on both the conversion function

and the temperature dependent rate coefficient $f(\alpha)$ and $k(T)$, respectively. The use of different reaction models to fit the experimental data followed by the evaluation of the reaction rate constant is only valid under isothermal conditions when $k(T)$ is constant. Under non-isothermal conditions, the reaction is controlled by the kinetic mechanisms and the increased thermal activation (Schonborn and Haessner, 1985). As a result, the Arrhenius parameters will tend to change under different experimental conditions and could vary significantly in order to allow for a satisfactory fit of the chosen reaction model. This effect is known as the kinetic compensation effect which manifests itself in the linear relation between the activation energy and the pre-exponential factor (Malek, 1992):

$$\ln k_0 = c_1 E + c_2 \quad (6.32)$$

Consequently, attempts to determine kinetic parameters for a set of identical samples based on individual single DSC scans will lead to potentially aphysical kinetic parameters. Another complication is that under non-isothermal conditions, the volume fraction recrystallized depends on the $T(t)$ path. Therefore, a direct comparison of measurements performed on the same specimens but employing different temperature programs is impossible unless a program-independent kinetic equation is postulated. However, for linear heating experiments, this problem can be circumvented by transforming the known $T(t)$ to a dependence on T . As such, Schonborn and Haessner (1985) proposed the representation of non-isothermal DSC results on the degree of recrystallization for variable heating rates in the form of a function of a continuous

variable and a discontinuous test parameter, i.e., $X_V = X_V(T, \beta)$. The dependency on the temperature program is then eliminated by eliminating the heating rate resulting in a functional relation of the form $\dot{X}_V(X_V, T)$ for the reaction rate. Direct comparison between similar specimens with different heating rates is then possible. A similar manner to manipulate kinetic data was proposed by Kempen et al. (2002). In that paper, it was suggested to fit experimental values of the transformed fraction to the JMAK equation for different temperatures or different heating rates simultaneously. A similar approach is adopted in this thesis. Instead of modeling individual non-isothermal experimental results for each heating rate separately, a pool of experimental data for each alloy system investigated irrespective of the heating rate employed will be treated simultaneously. This means that a corresponding numerical solution will include the combination of time, temperature and the degree of recrystallization from all experimental runs with varying heating rates. An additional benefit of adopting this approach is to avoid inconsistencies that may arise in the evaluated Arrhenius parameters due to their mutual compensation effect. Consequently, uncertainties in the numerical values of a computed kinetic triplet will be reduced and they could be regarded as the true effective constants. For the case of the formal JMAK approach, the procedure employed for the kinetic evaluation can be summarized in the following steps:

- 1) The volume fraction recrystallized determined from DSC experiments will be utilized together with the corresponding instantaneous time and temperature

values. The analysis of the recrystallization kinetics will be based on the formal JMAK expression:

$$x(t, T) = 1 - \exp \left[-k_0 \exp \left(-\frac{E}{RT} \right) t^n \right] \quad (6.33)$$

- 2) For each alloy characterized by its own composition, \bar{C} and strain, ε ; the intention is to find the kinetic triplet k_0 , E and the unknown from the conversion function n . To do so, M calorimetric runs with various heating rates will be performed. During the i -th run, N_i experimental points will be recorded. It is assumed that the accuracy of all measurements is the same, i.e. that all data point have the same statistical weight.
- 3) The model's parameters are then evaluated by the method of non-linear least-squares. A starting point will be minimizing the following objective function:

$$F = \sum_{i=1}^M \sum_{j=1}^{N_i} \left(x_{ji}^{\text{exp}} - x(t_{ji}, T_{ji}) \right)^2 = \sum_{i=1}^M \sum_{j=1}^{N_i} \left(x_{ji}^{\text{exp}} - 1 + \exp \left[-k_0 \exp \left(-\frac{E}{RT_{ji}} \right) t_{ji}^n \right] \right)^2 \quad (6.34)$$

$$\frac{\partial F}{\partial k_0} = -2 \sum_{i=1}^M \sum_{j=1}^{N_i} \alpha_{ji} \times \exp \left[-k_0 \exp \left(-\frac{E}{RT_{ji}} \right) t_{ji}^n \right] \times \exp \left(-\frac{E}{RT_{ji}} \right) t_{ji}^n \quad (6.35)$$

where

$$\alpha_{ji} \equiv x_{ji}^{\text{exp}} - 1 + \exp \left[-K_0 \exp \left(-\frac{E}{RT_{ji}} \right) t_{ji}^n \right] \quad (6.36)$$

$$\frac{\partial F}{\partial E} = +2 \sum_{i=1}^M \sum_{j=1}^{N_i} \alpha_{ji} \times \exp \left[-k_0 \exp \left(-\frac{E}{RT_{ji}} \right) t_{ji}^n \right] \times k_0 t_{ji}^n \exp \left(-\frac{E}{RT_{ji}} \right) \frac{1}{RT} \quad (6.37)$$

$$\frac{\partial F}{\partial n} = -2 \sum_{i=1}^M \sum_{j=1}^{N_i} \alpha_{ji} \exp \left[-k_0 \exp \left(-\frac{E}{RT_{ji}} \right) t_{ji}^n \right] \times k_0 \exp \left(-\frac{E}{RT_{ji}} \right) n t_{ji}^{n-1} \quad (6.38)$$

- 4) Expressions (6.35), (6.37) and (6.38) can directly be used for calculating the Jacobian.
- 5) To start solving the non-linear least-squares problem, a good initial approximation is required. In order to find it, expression (6.33) can be linearized:

$$1 - x(t, T) = \exp \left[-k_0 \exp \left(-\frac{E}{RT} \right) t^n \right] \quad (6.39)$$

$$-\ln(1 - x(t, T)) = k_0 \exp \left(-\frac{E}{RT} \right) t^n \quad (6.40)$$

$$\ln(-\ln(1 - x(t, T))) = \ln k_0 - \frac{E}{RT} + n \ln t \quad (6.41)$$

- 6) The initial approximation can then be found by minimizing the following objective function:

$$F_{\text{lin}} = \sum_{i=1}^M \sum_{j=1}^{N_i} \left(\ln(-\ln(1 - x_{ji}^{\text{exp}})) - \left(\ln k_0 - \frac{E}{RT_{ji}} + n \ln t_{ji} \right) \right)^2 \quad (6.42)$$

- 7) A Fortran code will then be developed in which problem (6.42) can easily be solved through using the subroutine LSQRR/DLSQRR from IMSL.
- 8) After the initial approximation is found, the problem (6.34) can be solved through using either UNLSF/DUNLSF¹ or, better, UNLSJ/DUNLSJ² from IMSL.

¹ A finite-difference Jacobian is used.

² An analytical user-supplied Jacobian is used.

6.4.2 Path Variable Approach for Non-isothermal Transformations

The main debatable point concerning a kinetic analysis under non-isothermal conditions is the dependence of the transformation rate on the thermal history of the specimen and a misuse of rate expressions valid for isothermal experiments for non-isothermal cases. Although the isokinetic hypothesis offers flexibility in the kinetic analysis by allowing a direct usage of the general rate equation and corresponding mathematical models. The validation and the limited reactions exhibiting such behavior remain a restrictive factor towards a generalization of the kinetic analysis procedure to any reaction type. In an attempt to present a general framework for the analysis of the kinetics of recrystallization under non-isothermal conditions, the path variable approach originated by Mittemeijer (1992) will be employed. It allows the determination of the kinetic parameters regardless of the time-temperature program employed.

The problem with non-isothermal conducted experiments is the dependence of the boundary values, i.e. the starting and final values of the physical property measured on the employed time-temperature program or, in other words, the thermal history of the specimen. This is illustrated schematically in Figure 6.1 where a thermally-activated phase transformation from state 1 (t_1, T_1) to state 2 (t_2, T_2) may occur along two different paths (a) or (b) . While the time for both trajectories remains the same, higher temperatures encountered along the path (b) will lead to a greater degree of transformation at the state

2. Hence, time and temperature cannot be considered as state variables for the extent of transformation.

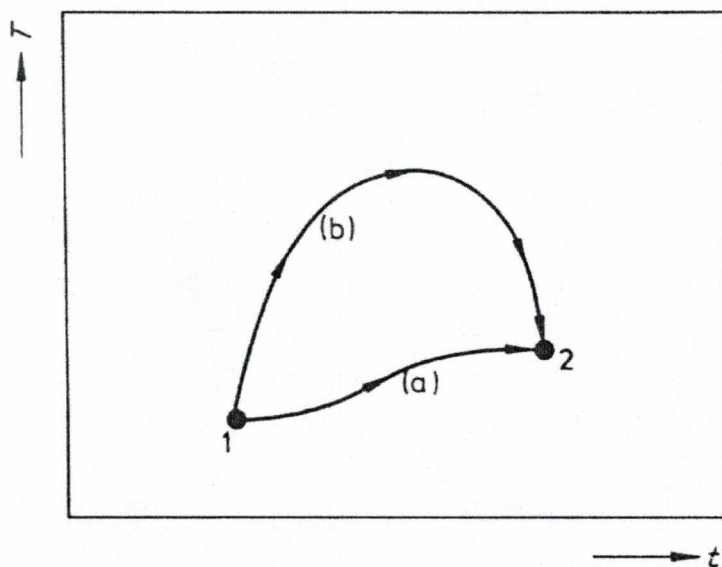


Figure 6.1: Schematic representation of the dependence of the stage of transformation on the thermal history for a thermally activated transformation. (Mittemeijer, 1992)

To overcome such limitation, Mittemeijer proposed the introduction of a path variable Φ which is fully determined by the time-temperature program employed, and which depends on the thermal history of the material. The degree of transformation can then be described in terms of the new state variable as (Mittemeijer, 1992; Kempen et al., 2002):

$$\alpha = F(\Phi) \tag{6.43}$$

This expression does not assume any specific relation between α and Φ . If the transformation mechanism remains unchanged in the time-temperature region considered; it is pertinent to express Φ as proportional to the number of atomic jumps where

temperature determines the mobility while time specifies the duration. For such case and under non-isothermal annealing conditions, the dependence of Φ on the thermal history can be expressed as:

$$\Phi = \int k(T(t))dt \quad (6.44)$$

Such dependence reduces for isothermal annealing conditions to the simple relation:

$$\Phi = k(T)t \quad (6.45)$$

The above representation of the path variable is compatible with the additivity rule and generates kinetic parameters which are independent of the thermal history as long as the course of the transformation remains unaffected by the annealing conditions. For instance, if equation (6.45) is to be employed for non-isothermal transformations on the basis of an infinitesimal lapse of time, i.e. if $d\Phi = kdt$, then this will lead to results conforming with expression (6.44). Therefore, based on the path variable introduction, the transformation rate for both isothermal and non-isothermal conditions will have the similar form:

$$\frac{d\alpha}{dt} = \frac{dF(\Phi)}{d\Phi} \frac{d\Phi}{dt} = k(T) \frac{dF(\Phi)}{d\Phi} \quad (6.46)$$

Since the temperature-time program for isochronal annealing is described by the relation:

$$T(t) = T_0 + \beta t \quad (6.47)$$

Adopting an Arrhenius dependence of the rate constant and employing equation (6.47), the path variable reduces to:

$$\Phi = k_0 \int \exp(-E/R(T_0 + \beta t)) dt \quad (6.48)$$

For experiments with a constant heating rate, the time integral can be replaced by a temperature integral. Kempen et al. (2002) proposed a procedure for the approximation of the temperature integral by first introducing a new time parameter $t' = t + T_0/\beta$, where $dt = dt'$ and $T_0 + \beta t = \beta t' = T(t')$. The integration limits can then be taken as T_0/β and t'_e . If T_0 is small, then on heating $\Phi(T < T_0) \approx 0$, and the time scale $t' = T_0/\beta$ can be shifted to $t' = 0$ without grossly affecting the integral, thus:

$$\Phi = k_0 \int_{T_0/\beta}^{t'_e} \exp(-E/R\beta t') dt' \approx k_0 \int_0^{t'_e} \exp(-E/R\beta t') dt' \quad (6.49)$$

By employing a series expansion of the exponential integral of the form:

$$\int_1^{\infty} \frac{e^{-xt}}{t^n} dt = \frac{e^{-x}}{x} \left[1 - \frac{n}{x} + \frac{n(n+1)}{x^2} + \dots \right] \quad (6.50)$$

By using (6.50) in (6.49), the path variable can be approximated:

$$\Phi \approx k_0 \int_0^{t'_e} \exp(-E/R\beta t') dt' \approx \frac{k_0 \beta R t'^2}{E} \exp(-E/R\beta t') \left[1 - 2 \frac{R\beta t'}{E} + 6 \left(\frac{R\beta t'}{E} \right)^2 - \dots \right]_{t'_e}^0 \quad (6.51)$$

Substituting $t' = T(t')/\beta$, and knowing that for solid-state transformations, $RT/E \ll 1$ and $R\beta t' \ll E$, a final approximation of the path variable formula is obtained:

$$\Phi \approx \frac{k_0 RT^2}{\beta E} \exp\left(-\frac{E}{RT}\right) \quad (6.52)$$

By combining equations (6.43) and (6.52), the degree of transformation becomes uniquely described by the state variable Φ regardless of the time-temperature program. Moreover, such description is compatible with both homogeneous and heterogeneous reactions. For example, if it assumed that the JMAK kinetics holds for the

recrystallization process, the prescription of α in terms of the path variable Φ can then be expressed as:

$$\alpha = 1 - \exp(-\Phi^n) \quad (6.53)$$

$$\alpha = 1 - \exp\left(-\left(\frac{k_0 RT^2}{\beta E} \exp\left(-\frac{E}{RT}\right)\right)^n\right) \quad (6.54)$$

Therefore, the path variable approach provides a more realistic description of the kinetics of non-isothermal transitions. Furthermore, its compatibility with the JMAK kinetics allows for a permissible assessment of the JMAK expression for the description of non-isothermal recrystallization of AA6111 alloys regardless of the employed temperature program. Nevertheless, it should be noted that the use of a JMAK-like functional form for the path variable implicitly entails that all the assumptions related to the development of the JMAK analytical description still hold.

Evaluation of the recrystallization kinetics will then be based on (6.54). The model parameters will be evaluated by the method of non-linear least-squares. In this case the objective function to be minimized will be of the form:

$$F = \sum_{i=1}^M \sum_{j=1}^{N_i} \left(x_{ji}^{\text{exp}} - x(t_{ji}, T_{ji}) \right)^2 = \sum_{i=1}^M \sum_{j=1}^{N_i} \left(x_{ji}^{\text{exp}} - 1 + \exp\left[-\left(\left(\frac{k_0 RT_{ji}^2}{\beta E}\right) \exp\left(-\frac{E}{RT_{ji}}\right)\right)^n\right] \right)^2 \quad (6.55)$$

For each alloy, the experimental results from DSC scans carried out at different heating rates will be modeled simultaneously in a similar manner to the formal JMAK kinetic

procedure outlined in the previous section. However, the fitting data in this case will contain the volume fraction recrystallized, the temperature and the heating rate.

CHAPTER 7

Results and Discussion

7.1 Thermal Events

7.1.1 Effect of Solute Content

The precipitation sequence in the solution treated (i.e. as-quenched) samples of the AA6111 alloys was investigated using DSC. The scans were performed within a two hour limit following quenching. This represented the necessary time for DSC sample preparation from the heat treated alloy blocks. The DSC curves recorded at two different heating rates for the 6111-NC-SHT alloy are shown in Figure 7.1. Five total enthalpic effects were observed in the temperature range from 70 °C to 500 °C, which are referred to as peaks A through E. Comparing the location of these events with previously reported sequences of precipitation of Al–Mg–Si–Cu alloys summarized in section 2.4.1, the following peak associations could be drawn. The first broad exothermic event A taking place in the temperature range of about 80-200 °C is associated with clustering of the Mg and Si atoms and the subsequent GP zones formation. The small endothermic bump B occurring just before the exothermic peak C is attributed to the dissolution of some of the GP zones as reported by Miao and Laughlin (2000). The two prominent adjacent exothermic peaks C and D represent the precipitation of the β'' phase and the Q'' phase,

respectively. The two peaks were centered at 260 °C and 300 °C for the 20 °C/min heating rate and shifted slightly to higher temperatures with the increase in the heating rate. Earlier studies usually associate peak D with the precipitation of β' and/or Q' phases (Miao and Laughlin; 2000). However, recent results by Wang et al. (2006) on the precipitation sequence in a similar AA6111 evidenced the formation of a fully coherent precursor to the Q' phase which they identified as Q'' . Nevertheless, the authors did not exclude the possibility of the formation of β' in the precipitation sequence. The existence of lath-shaped precursors to Q' was also observed in peak aged Al–Mg–Si–Cu alloys and in balanced Al–Mg–Si alloys with copper additions (Chakrabarti and Laughlin, 2004). Finally, the very weak exothermic effect E expanding over a temperature range of about 330–370 °C was suggested by Wang et al. (2006) to correspond to the formation of Q' and Q phases. Earlier studies by Esmaeili et al. (2003) associated such peak to the equilibrium Q phase alone. Both associations are plausible considering the fact that the transition from the metastable precursor Q' to the Q phase involves insignificant energy changes as both phases have the same crystal structure and lattice parameters.

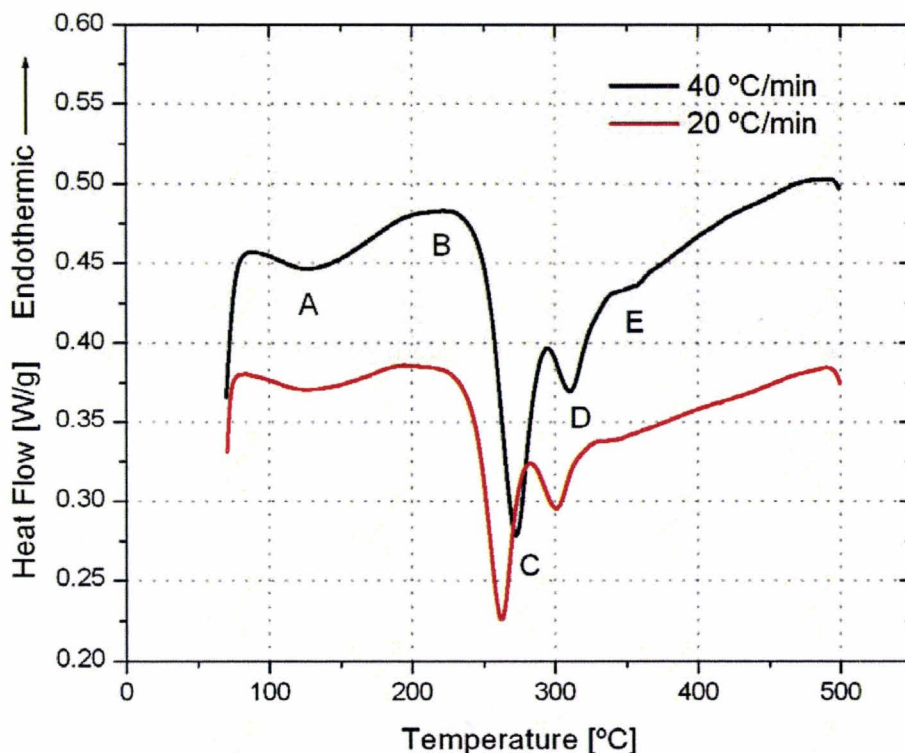


Figure 7.1: DSC thermogram for 6111-NC-SHT alloy at scan rates of 20 and 40 °C/min.

A similar sequence of precipitation events with only slight differences in the temperature ranges was observed for the alloys with the high and low Fe and Mn contents as shown in Figure 7.2. The major distinct difference in the aging response was the size of the exothermic peak C associated with the β'' precipitation. For the alloy with the negligible Fe and Mn contents 6111-LC-SHT, the exothermic signal was much more pronounced compared to that of the 6111-HC-SHT alloy with the high Fe and Mn levels. This indicates that the amount of β'' precipitation decreases with increasing the Fe and Mn contents. Similar results were reported by Kuijpers et al. (2002) in as-cast AA6xxx

alloys. Increasing the Fe and Mn levels will increase the amounts of Al-Fe-Si and Al-Fe-Mn-Si second-phase particles. As a result, the Si atoms will be consumed by the formation of these particles and their concentration levels in the matrix will decrease. This reduces the driving force for the nucleation of the β'' phase and results in a reduced precipitation rate. Such effect of Fe and Mn levels is also evident from the clusters and GP zones formation peak A. The magnitude of the peak decreased with the increase in the Fe and Mn levels.

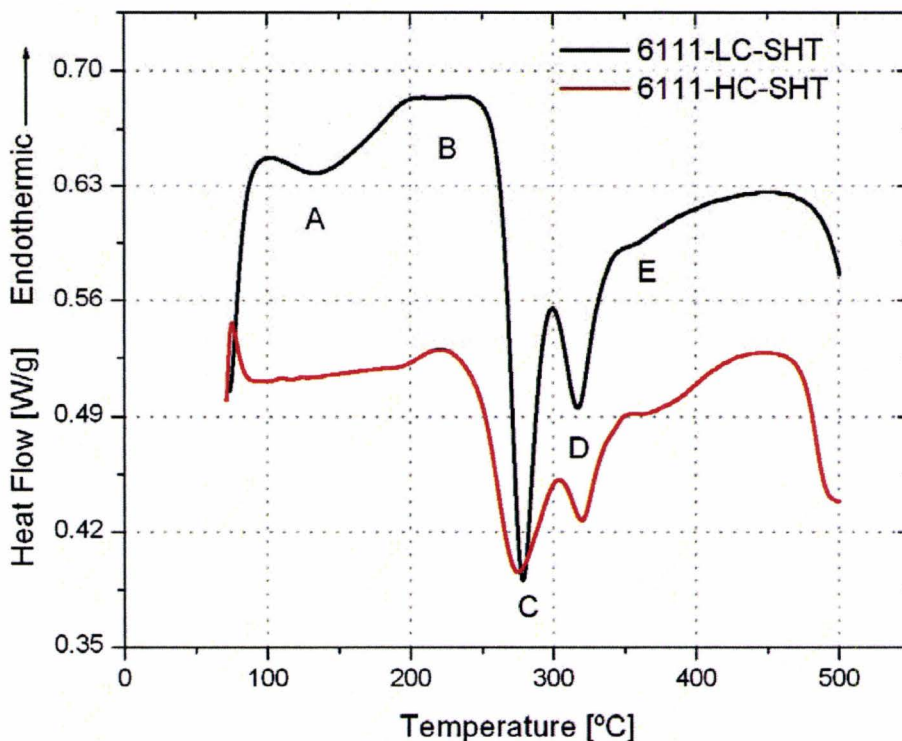


Figure 7.2: DSC thermograms for 6111-LC-SHT and 6111-HC-SHT at a scan rate of 40 °C/min.

7.1.2 Effect of Cold Rolling

On the contrary to the extensive literature available on the precipitation sequence of supersaturated solid solutions of undeformed Al–Mg–Si alloys, only few studies have addressed the effect of predeformation on the aging response. As this research involves severely cold rolled samples, the decomposition kinetics from the deformed state was investigated by DSC and TEM. Figure 7.3 shows the DSC thermograms recorded at a heating rate of 40 °C/min for both the cold rolled and undeformed AA6111 specimens with the nominal composition. Cold rolling was performed immediately after the solution heat treatment to a true strain of 2.3 and 1.6.

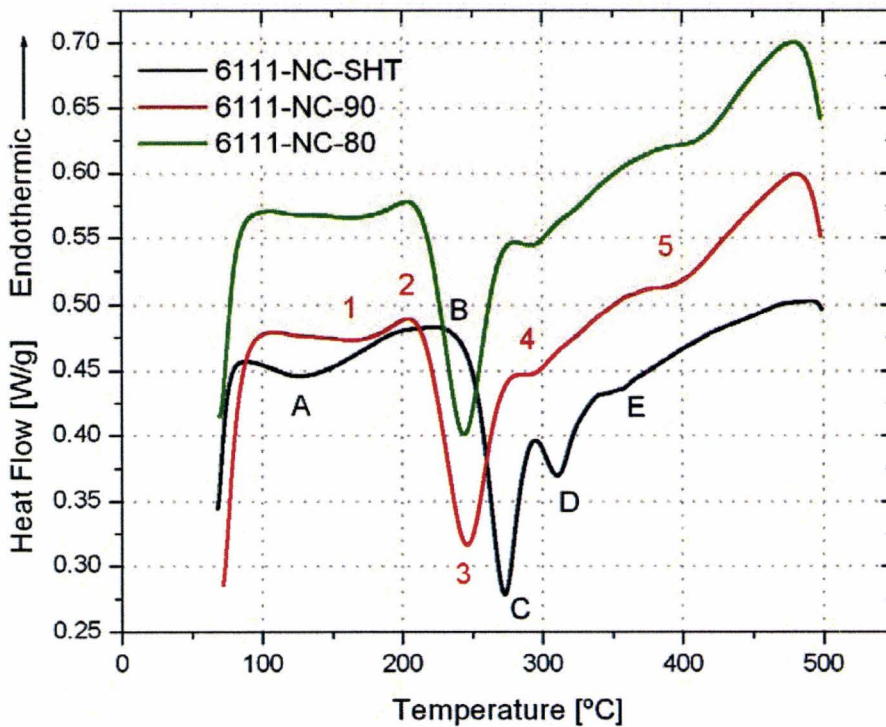


Figure 7.3: DSC thermograms for undeformed and cold rolled 6111-NC alloys at a scan rate of 40 °C/min.

Five total thermal events were identified in the DSC trace for the deformed samples in the temperature range of 70-500 °C, and are labeled by numbers along the curve. The first exothermic effect (peak 1) coincides with peak A previously attributed to the clusters and GP zones formation in the undeformed samples. However, the enthalpy of formation of the peak (i.e. the peak area) has decreased substantially in comparison to the undeformed sample. Clusters and zones formation are directly related to the population of quenched-in vacancies in the supersaturated solid solution (Birol, 2006). Dislocations act as vacancy sinks and their introduction in the material reduces the vacancy population (Deschamps et al., 1999). This explains the reduced kinetics of clusters and GP zones formation as reflected by the small size of peak 1 in the deformed sample compared to the corresponding peak in the undeformed material (effect A). Similar results for the suppression of clusters and GP zones formation during DSC heating of solutionised then deformed Al–Mg–Si alloys were reported by Yassar et. al (2005) for experiments on cold rolled AA6022 alloys and Birol (2006) in his study of the effect of deformation induced by punching operations on the aging response of AA6082 alloys. Despite the observed slow kinetics of clusters and GP zones formation in the deformed samples, their stability is expected to increase with the level of cold work. Deformation tends to accelerate the transformation from clusters to zones resulting in a decrease in their numbers and sizes together with an increased internal vacancy concentration within the individual clusters. This in turn leads to an increased binding energy between the zones and vacancies (Quainoo and Yannacopoulos, 2004). Therefore, the zones will be more resistant to reversion at higher temperatures and subsequently grow to become stable nuclei for the

β'' phase. This explains the decrease in the size of the second endothermic peak (effect 2) in the DSC trace for the deformed material in comparison to its corresponding GP zones reversion peak B in the as-quenched sample. Following the GP zones reversion process, two adjacent exothermic peaks were observed on the DSC trace of the deformed sample. These peaks were obtained in the temperature range of 200 to 305 °C (effects 3 and 4) and differ from their corresponding events in the undeformed material in two main features. Firstly, the peak reaction temperatures were shifted to lower temperature by about 28 °C and 15 °C for effects 3 and 4, respectively. Secondly, the magnitude of the exothermic peak 4 decreased significantly in comparison to effect E for the undeformed sample. These two peaks were previously attributed to the precipitation of β'' and Q'' in the undeformed material. Figure 7.4 shows the TEM bright field image (BF), dark field image (DF) and the selected area diffraction pattern (SADP) of the deformed sample heated up to 330 °C. This temperature corresponds to the steady state conditions recorded by the DSC following the end of peak 4. Two different types of precipitates were present in the microstructure. The needle-shaped precipitates appearing as dots with a circular-cross sectional area when viewed end-on and the lath-shaped precipitates with a rectangular cross-sectional area. The morphologies of these phases and the streaks on the SADP are in agreement with β'' and Q' phases. This indicates that peaks 3 and 4 in the deformed samples are mainly associated with the precipitation of β'' and Q' , respectively.

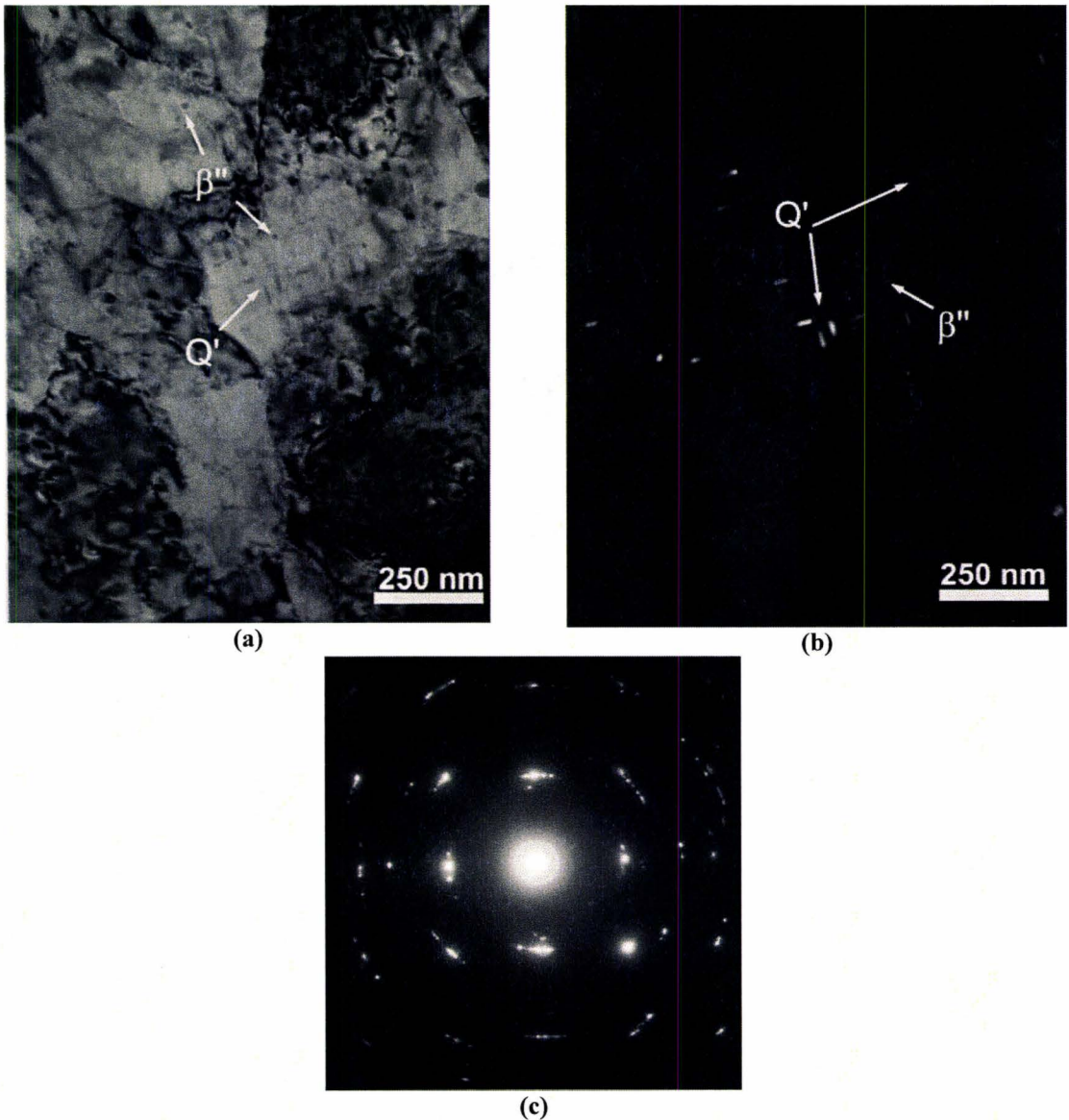


Figure 7.4: TEM micrographs of a 6111-NC-90 sample heated up to 330 °C at a rate of 40 °C/min: a) BF image, b) DF image and c) the corresponding [001]_{Al} SADP.

As such, it is clear that the deformation has altered both the kinetics and sequence of the metastable phases in the AA6111 alloys. Faster rates of formation for both β'' and Q' were observed in the deformed sample as reflected by the decrease in their peak reaction temperatures compared to the undeformed sample. A similar shift in the precipitation

events of β'' to lower temperature after predeformation was reported by Quainoo and Yannacopoulos (2004) for AA6111 and Yassar et al. (2005) for AA6022. The decrease in the precipitation temperatures of β'' and β phases due to dislocations was also reported by Zhen and Fei (1997) for Al–Mg–Si alloys even when cold rolling was performed before the solution heat treatment.

In addition to the enhanced precipitation kinetics, the deformation has favored the precipitation of the more stable Q' instead of Q'' . This explains why effect D associated with Q'' formation in the DSC trace of the undeformed sample is entirely missing for the deformed case. The role of dislocations in promoting the precipitation of the more stable phases has been previously reported for both 6xxx and 7xxx series aluminum alloys. For example, Yassar et al. (2005) indicated the precipitation of β' and Q' instead of β'' during aging of solutionised then deformed AA6022, while Birol (2005 & 2006) showed an enhancement in the transformation of β'' to β' during aging of deformed AA6016 and AA6082. The author suggested that in the presence of high dislocation densities, the β'' phase may lose coherency and transform to β' as soon as it precipitates with a transformation rate dependant on the level of prestraining. Similarly, for Al–Zn–Mg alloys the presence of dislocations has been shown to favor the precipitation of the equilibrium η phase instead of its metastable version (Deschamps et al., 1999).

The above changes in the aging response of heat-treatable aluminum alloys due to the induced deformation can be explained in terms of heterogeneous precipitation on

dislocations. Dislocations are favorable nucleation sites for precipitates and act as short-circuit diffusion paths for solutes leading to faster and coarser precipitation on dislocation. Silicon diffusion, for example, has an activation energy of 0.85 eV along dislocations in comparison to 1.3-1.6 eV in the bulk (Zhen and Fei, 1997). This results in a global acceleration of precipitation kinetics in heat-treatable aluminum alloys and promotes the formation of the more stable phases (Yassar et al., 2005; Deschamps et al., 1999).

The small exothermic peak (effect 5) was only observed in the DSC scans of the cold rolled samples. Increasing the level of cold work shifted the peak to lower temperatures and slightly increased its magnitude as shown in Figure 7.3. The microstructural changes occurring in the 6111-NC-90 samples along peak 5 were investigated by TEM. Figure 7.5 shows the TEM bright field image of a sample quenched before the peak (≈ 330 °C). Deformation bands and elongated grains with high dislocation tangles were observed together with few fine subgrains. This indicates the activation of very weak recovery processes. A small strain free grain is also visible in the microstructure evidencing the onset of the recrystallization process. The TEM bright field image of a sample quenched from the mid peak section (≈ 400 °C) is shown in Figure 7.6. A majority of lath-shaped Q' precipitates which coarsened substantially are observed in the microstructure together with broken up dispersoids. Figure 7.7 shows the microstructure of a sample quenched after the peak (≈ 460 °C). The lath-shaped precipitates were homogeneously distributed in the matrix and the grains were free from

dislocations. The above results clearly indicate that the peak is related to the release of stored energy in the deformed material.

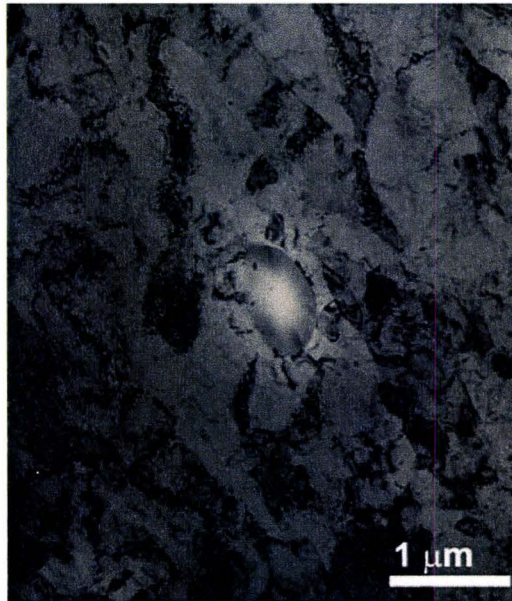


Figure 7.5: TEM micrograph of a 6111-NC-90 sample heated up to 330 °C at a rate of 40 °C/min illustrating the deformation microstructure as well as recovery and recrystallization effects.



Figure 7.6: TEM micrograph of a 6111-NC-90 sample heated up to 400 °C at a rate of 40 °C/min.



Figure 7.7: TEM micrograph of a 6111-NC-90 sample heated up to 460 °C at a rate of 40 °C/min.

The effect of varying the solute content on the aging response of the cold rolled AA6111 was also investigated. Figure 7.8 shows the DSC traces obtained at a heating rate of 40 °C/min for samples with high and low Fe and Mn levels. While the peaks arrangement for the low Fe and Mn alloy 6111-LC-90 were identical to those observed in the nominal composition alloy 6111-NC-90, the DSC trace for the 6111-HC-90 alloy showed an additional exothermic event following the recrystallization peak. The microstructure of a 6111-HC-90 sample quenched just above this new thermal event is illustrated in Figure 7.9. Two different precipitate morphologies were observed, a uniform distribution of fine square-based plate-shaped precipitates and large irregularly shaped particles. The EDS analysis of the fine precipitates revealed Al and Si peaks as shown in the spectrum in Figure 7.10, while the spectrum from the large particles indicated that they are insoluble intermetallics with an Al(Fe,Mn)Si composition as

illustrated in Figure 7.11. Therefore, this exothermic peak is ascribed to the formation of Mg_2Si precipitates.

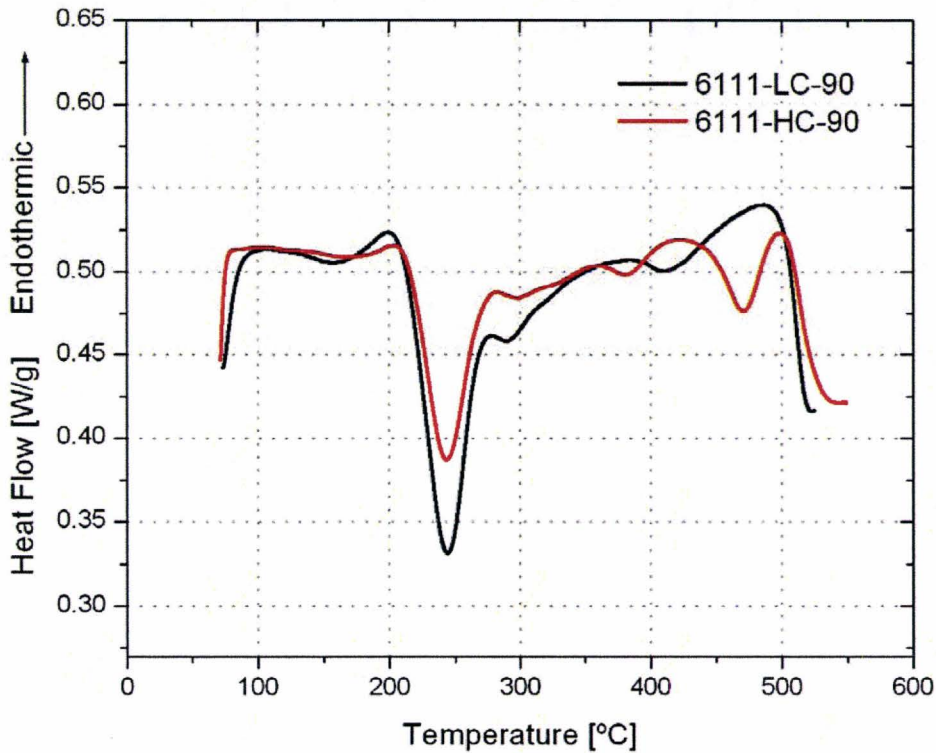


Figure 7.8: DSC thermograms for 6111-LC-90 and 6111-HC-90 at a scan rate of 40 °C/min.

In addition to the appearance of the new β formation peak, the location and magnitude of the recrystallization peak varied considerably with the change in solute content. Increasing the levels of Fe and Mn shifted the peak to lower temperatures and increased its magnitude, while the opposite was true for the low Fe and Mn levels. This could be attributed to the increased population of second-phase particles and their role in

the particle-stimulated nucleation of recrystallization. The effect of solute content on the recrystallization kinetics is further discussed in section 7.6.1.

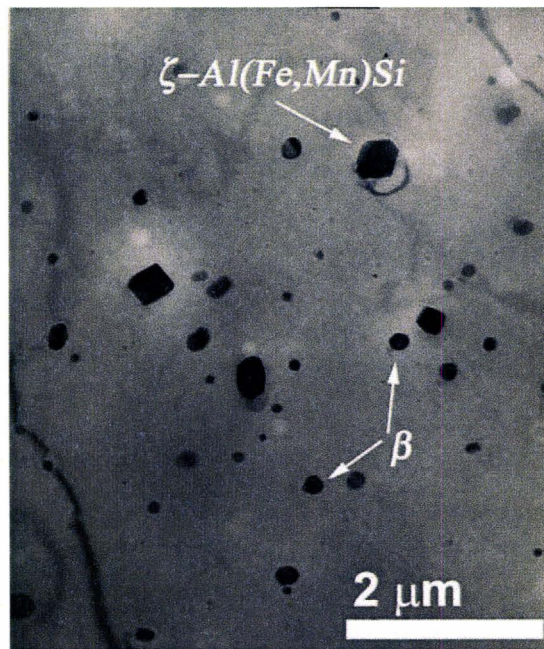


Figure 7.9: TEM micrograph of a 6111-HC-90 sample heated up to 500 °C at a rate of 40 °/min, illustrating the formation of equilibrium Mg_2Si precipitates.

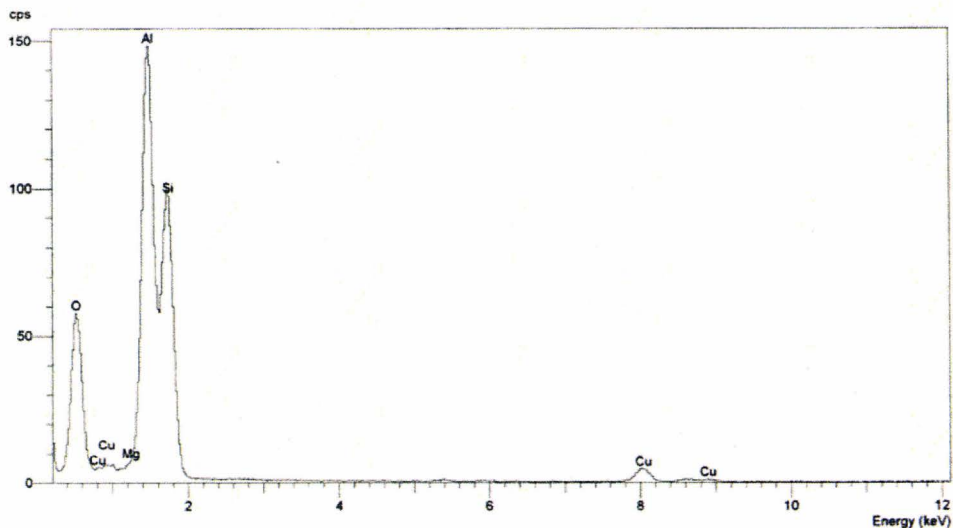


Figure 7.10: EDS spectrum from the fine Mg_2Si precipitates.

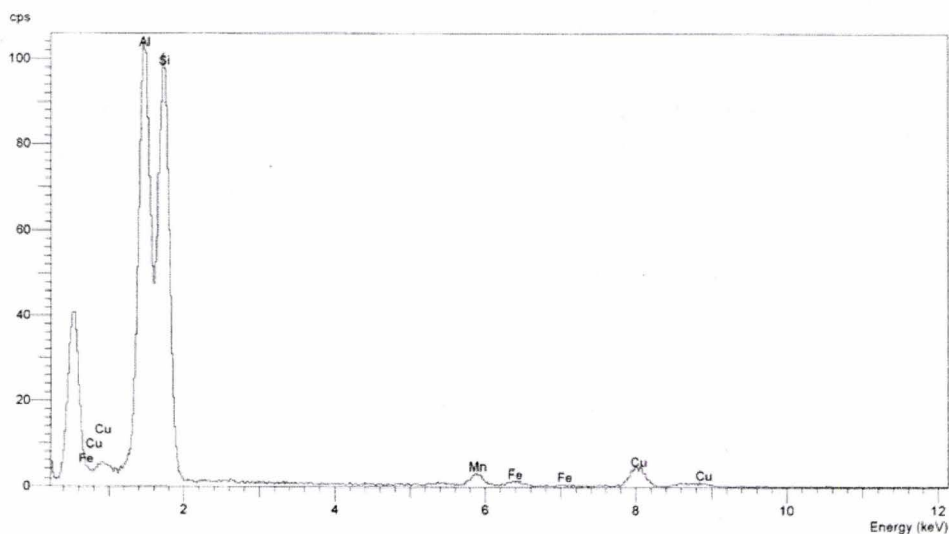


Figure 7.11: EDS spectrum from the large intermetallic particles.

7.2 The Deformed State

The dislocation structure following a 90% thickness reduction was investigated by TEM and the bright field image is shown in Figure 7.12. The dislocations were arranged in loosely defined cellular structure with planar channels and very diffuse boundaries. Very few subgrains were also visible but their boundaries were not sharp and consisted of high dislocation densities. Figure 7.13 shows a dislocations structure from another local area in the same sample where high densities of tangled dislocations were almost homogeneously distributed in the Al matrix without the development of a significant cellular structure. The above results indicate very slow rates of dynamic recovery that may be attributed to the solute content, especially Mg, and their role in lowering the stacking fault energy of aluminum alloys and therefore hindering cross slip of dislocations (Verdier et al., 1999; Janeček et al., 2004).

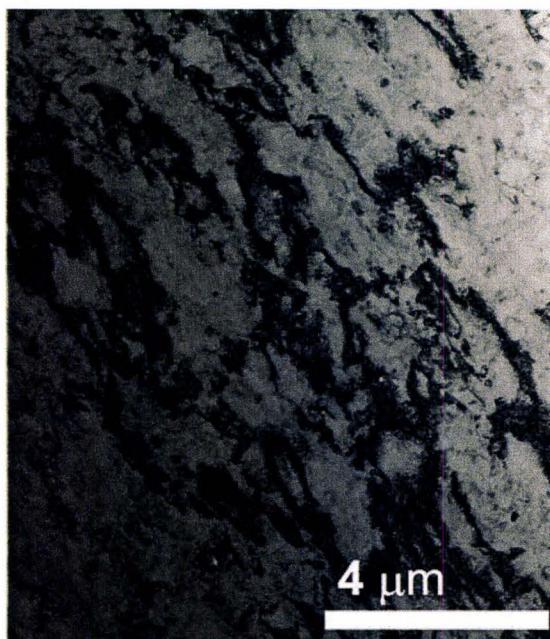


Figure 7.12: TEM micrograph of as-rolled 6111-HC-90.

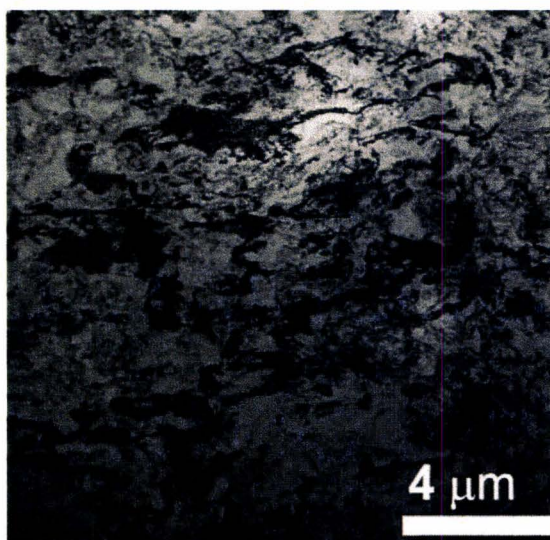


Figure 7.13: TEM micrograph of as-rolled 6111-HC-90 illustrating an almost uniform distribution of dislocations.

7.3 Optical Microscopy

The microstructural development during the course of linear heating of the three AA6111 alloys was investigated by optical microscopy. The temperature program employed in the DSC scans was simulated using a tube furnace, and samples were quenched from temperatures corresponding to the thermal events reflected by the DSC thermograms. Figure 7.14 illustrates the evolution of the microstructure of the 6111-NC-90 samples. No obvious changes in the grain structures were observed between the cold-rolled material and those annealed to 340 °C. The microstructures consisted of parallel bands of highly elongated pancake-shaped grains in the rolling direction with a uniform distribution of broken up intermetallic constituents both in the bulk and along the grain boundaries. The first change from the deformation microstructure appeared in samples annealed to 390 °C. A very low volume fraction of small recrystallized grains was observed indicating the onset of the recrystallization process as seen in Figure 7.14(c). This temperature lies within the exothermic peak that was previously assigned to the recrystallization process. The microstructure of samples annealed to 430 °C showed a fully recrystallized grain structure with highly ragged boundaries. Increasing the annealing temperature up to 470 °C did not reflect any significant changes in the recrystallization microstructure nor the grain-boundary character. This indicates that the recrystallization process reached completion through the temperature interval 350-430 °C without the development of an equilibrium grain structure. A similar behavior has been previously observed by Burger et al.(1996), and was contributed to fine dispersions of the

Q phase which effectively retard the motion of grain boundaries. Stable grain morphologies were only attainable after the Q phase dissolution at higher temperatures.

The microstructural developments during the non-isothermal anneal of the 6111-LC-90 and the 6111-HC-90 alloys were also investigated and the optical observations are shown in Figure 7.15 and Figure 7.16, respectively. For samples quenched from temperatures coinciding with the end of the thermal event previously associated with the release of stored energy of deformation; a fully recrystallized grain structure with highly ragged grain boundaries was observed for both alloys. However, the degree of irregularity of the grain boundaries was much more pronounced in the alloy with the high Fe and Mn levels, and remained without noticeable changes even after annealing to 500 °C. This is due to the increased volume fraction of intermetallics in these alloys and their subsequent break up during rolling operations. This results in a fine distribution of Fe-bearing constituents that will exert an additional retarding pressure on the grain boundaries. For the low Fe and Mn alloy 6111-LC-90, samples quenched from temperatures just after the onset of the recrystallization peak (≈ 410 °C) did not reveal any obvious signs of recrystallization as seen in Figure 7.15(a) on the contrary to the 6111-NC-90 samples seen in Figure 7.14(c). This suggests a relative dependency of the recrystallization kinetics on the alloy composition with faster rates achieved by increasing the Fe and Mn levels.

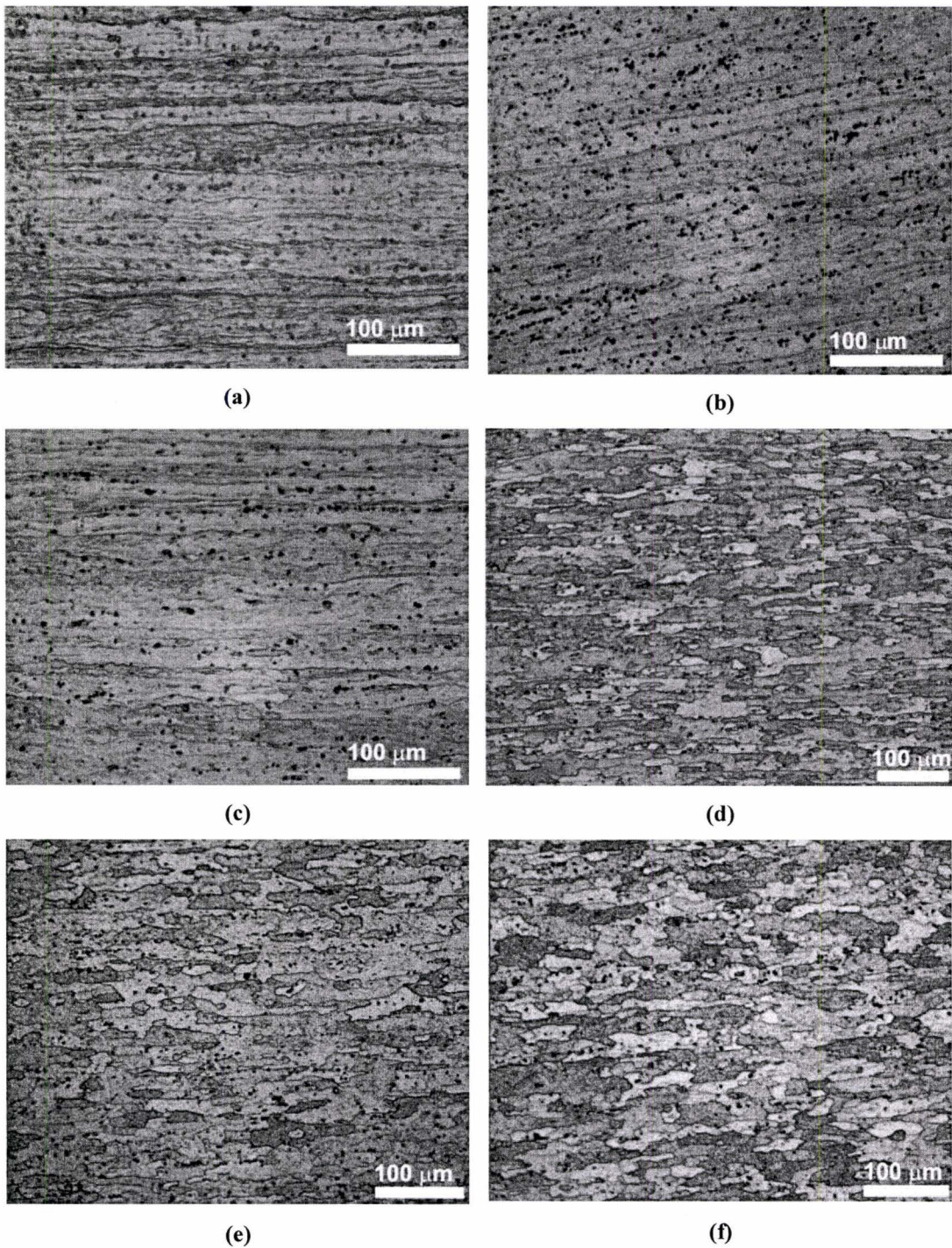
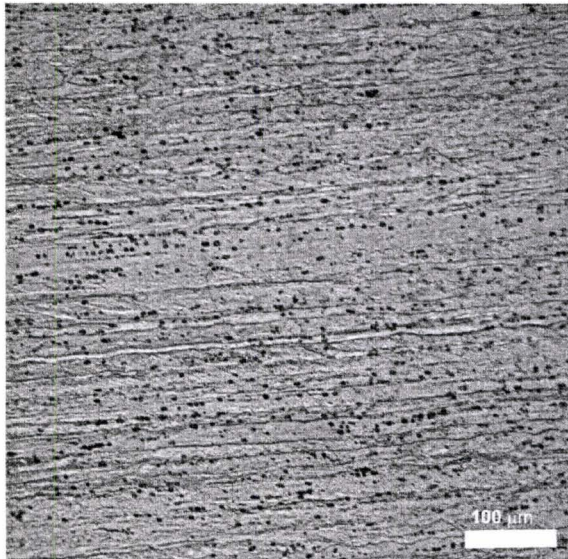
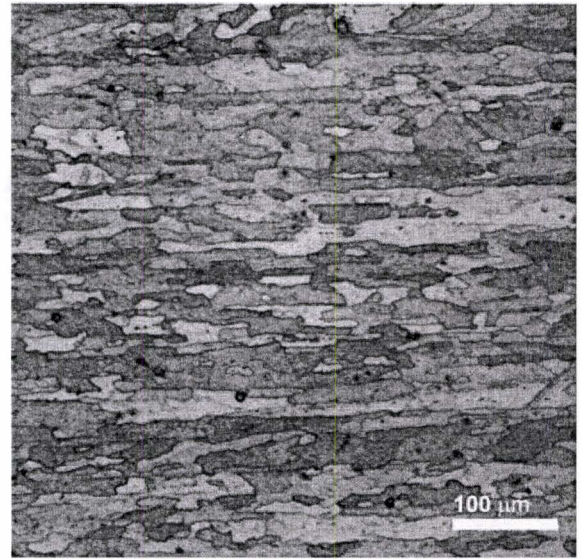


Figure 7.14: Development of microstructure in 6111-NC-90 during linear heating at a rate of 40 °C/min: a) as-deformed, b) 340 °C quench, c) 390 °C quench, d) 430 °C quench, e) 450 °C quench and f) 470 °C quench.

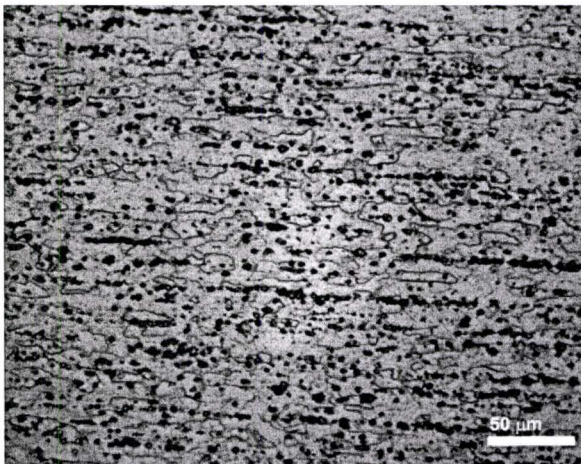


(a)

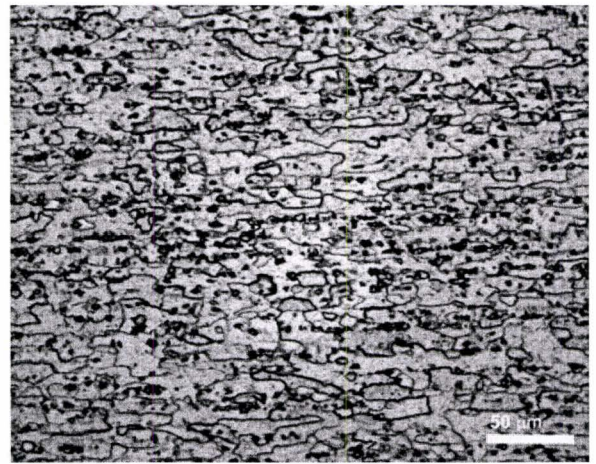


(b)

Figure 7.15: Development of microstructure in 6111-LC-90 during linear heating at a rate of 40 °C/min: a) 410 °C quench and b) 480 °C quench.



(a)



(b)

Figure 7.16: Development of microstructure in 6111-HC-90 during linear heating at a rate of 40 °C/min: a) 450 °C quench and b) 500 °C quench.

7.4 Softening Behavior

In support of the previous identification of the recrystallization peak, the softening behavior of AA6111 along the DSC heating schedule was investigated. The change in hardness with linear heating at a rate of 40 °C/min for quench-interrupted 6111-NC-90 samples together with the corresponding DSC trace are shown in Figure 7.17. An abrupt decrease in hardness was observed over the temperature range 300-430 °C. This coincides with the temperature interval of the recrystallization peak with a minimum hardness value of 51.56 VHN directly related to the fully recrystallized structure observed at 430 °C. A minor drop in hardness of about 3.3 % was observed on annealing of the cold rolled material to 300 °C despite the precipitation of the strengthening β'' and Q' phases. A similar trend was reported by Gutierrez-Urrutia et al. (2005) and Cerri and Leo (2005) during aging of 6082 aluminum alloys severely deformed by equal channel angular pressing. Thus, it is believed that strengthening in severely deformed Al–Mg–Si alloys is mainly due to work hardening as contributions owing to precipitation hardening are counteracted by recovery processes occurring over the same temperature range. The TEM micrographs of samples quenched from 330 °C revealed the presence of few fine subgrains. This confirms the occurrence of minor recovery of the deformation substructure during aging and explains the nearly constant or slightly decreasing trends in the hardness values prior to recrystallization. The softening behavior of the remaining alloy compositions followed the same previous trend as shown in Figure 7.18 and Figure 7.19, where the hardness drop overlapped with the recrystallization peaks.

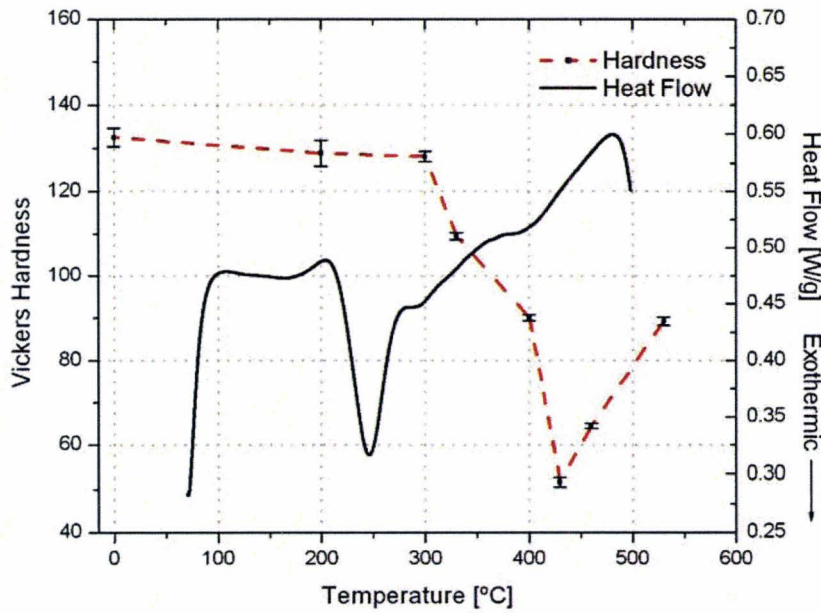


Figure 7.17: Variation of Vickers hardness with temperature during annealing of 6111-NC-90 (heating rate=40 °C/min).

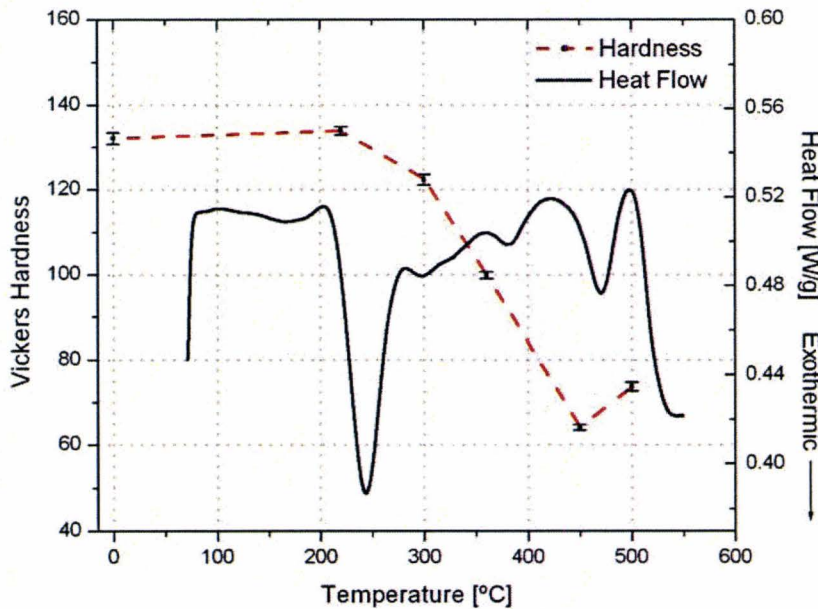


Figure 7.18: Variation of Vickers hardness with temperature during annealing of 6111-HC-90 (heating rate=40 °C/min).

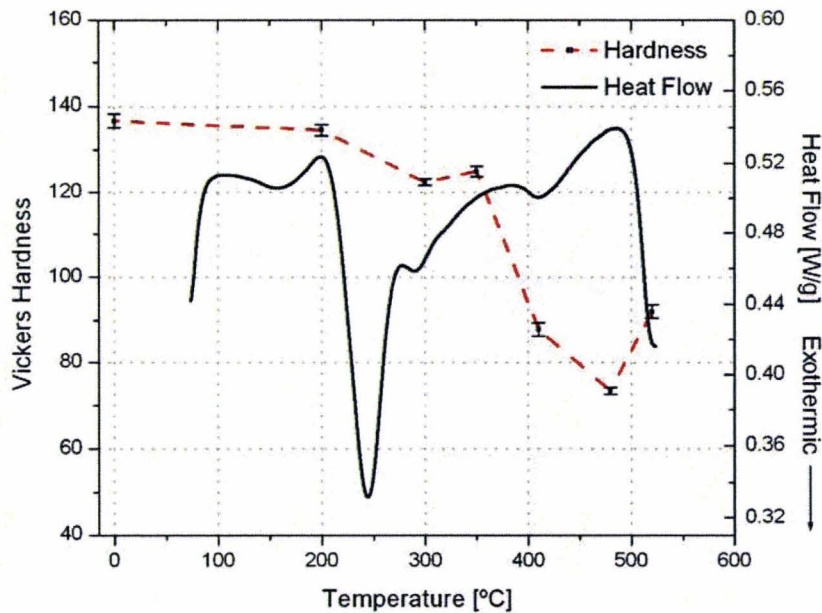


Figure 7.19: Variation of Vickers hardness with temperature during annealing of 6111-LC-90 (heating rate=40 °C/min).

Following the end of the recrystallization peak, the hardness values for the three alloy compositions were found to increase with temperature. The increase in hardness following recrystallization in AA6111 was previously observed by Burger et al. (1996) whom attributed the effect to the dissolution of Q and β phases at temperature above 430 °C. However, the DSC trace did not reflect any dissolution events and the TEM micrograph of 6111-NC-90 samples quenched from 460 °C revealed the presence of a high density of Q phase and a very few number of Mg_2Si particles as illustrated in Figure 7.7. In addition, a separate β phase formation peak was observed in the 6111-HC-90 samples in the same temperature range reflecting the hardness increase. Accordingly, the hardness increase must be related to the interaction between the recrystallizing interfaces

and the dispersed Q' precipitates present before the onset of recrystallization. Such interaction may take several forms. The precipitates may dissolve on contact with the moving high angle grain boundaries and then reprecipitate either discontinuously on the migrating boundaries or continuously in the recrystallized grains. In case the boundaries were effectively pinned by the precipitates then an enhanced coarsening of the precipitates would take place (Bee et al., 1981; Doherty, 1982). Both processes will lead to a solute redistribution and an increase in the matrix saturation levels especially locally around the precipitates. Therefore, the hardness increase following recrystallization could be interpreted in terms of solid solution hardening or the precipitation of hardening phases as a result of the resupersaturation of the matrix. The first effect was evident from the coarsening of the Q' and its transformation to the more stable Q phase in the course of the recrystallization process as shown in the TEM micrographs in Figure 7.6 and Figure 7.7 for the nominal composition 6111 alloy, while the second effect was exemplified by the Mg_2Si precipitation in the alloy with the high Fe and Mn levels and the disappearance of the Q phase as shown in Figure 7.9.

7.5 Electron Back Scatter Diffraction

7.5.1 Recrystallization Microstructures and Textures

Samples for the EBSD investigation were cut from sheets rolled to 90% thickness reduction. They were then annealed at a heating rate of 40 °C/min in a tube furnace followed by water quenching from temperatures following the end of the recrystallization

peak highlighted by corresponding DSC scans. The orientation maps are presented in Euler contrast. The level of strength of the red, green and blue colours is proportional to the three Euler angles and defines the orientation of each individual grain. The high angle grain boundaries with misorientations greater than 15° are indicated by black interfaces. Measurements of grain size and recrystallized volume fraction were based on mean linear intercepts. Figure 7.20 shows the orientation map for the nominal composition alloy 6111-NC-90 after quenching from 460°C . It is clear that recrystallization nucleated heterogeneously consuming most of the deformed substructure. The sample was 89% recrystallized with a mean recrystallized grain size of $8.34\ \mu\text{m}$. The large sized grains were slightly elongated in the rolling direction while the smaller grains were irregularly shaped. The grain aspect ratio obtained from the intercept lengths of the high angle grain boundaries in both rolling and normal directions was 1.9. The grain boundaries were highly jagged indicating that the fine Q' precipitates present before recrystallization, and their subsequent coarsening and transformation to the Q phase during recrystallization exerted a pinning pressure on the boundaries preventing their movement and grain growth.

The formation of small recrystallized grains is usually a consequence of grains originating by particle-stimulated nucleation of recrystallization (PSN) at large second-phase particles (Humphreys and Hatherly, 1995). The observed clustering of small grains with well defined boundaries in the vicinity of these particles as shown in Figure 7.21, and the dominance of small sizes in the grain size distribution as shown in Figure 7.22 point out to PSN as a potent recrystallization mechanism in this alloy.



Figure 7.20: Orientation map of 6111-NC-90 quenched from 460 °C. The RD is vertical and the ND is horizontal.

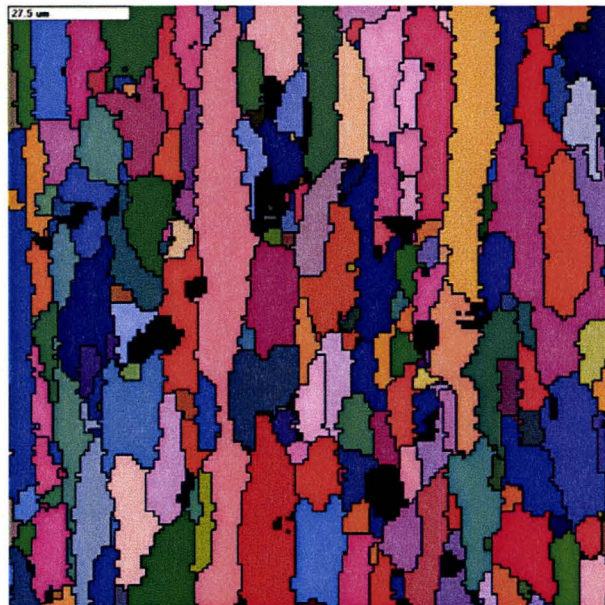


Figure 7.21: Orientation map of 6111-NC-90 quenched from 460 °C illustrating the clustering of small recrystallized grains in the vicinity of large second-phase particles. The RD is vertical and the ND is horizontal.

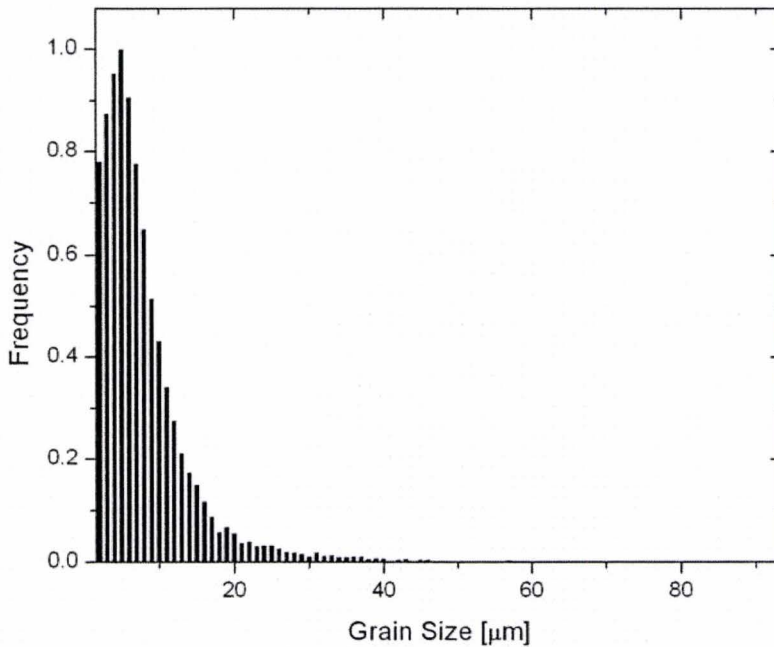


Figure 7.22: Histogram of grain size distribution in 6111-NC-90 quenched from 460 °C.

Previous TEM observation of the recrystallized microstructure (see Figure 7.7) has shown that the Q phase is uniformly distributed in the Al matrix. Consequently, in terms of both the uniform distribution of the Fe-constituents necessary for PSN and the uniform Zener drag pressure by the Q precipitates, a homogeneous recrystallization microstructure was expected for such alloy composition. However, this was not the case and bands of large grains were observed as seen in the center of Figure 7.20. This indicates that PSN is not the only operating nucleation mechanism. The inherited banded arrangement in the recrystallized microstructure points out to the preferential nucleation of new grains in Cube or Goss bands. This is further supported by the non-random spatial distribution of the Cube and Goss texture components in the recrystallized sample as seen

from Figure 7.23. Both orientations were aligned in the rolling direction. This proves that the efficiency of PSN was not sufficient to break up the textural alignment and that some nucleation events occurred preferentially in the bands and are responsible for the observed wide grain size distribution. However, judging from the weakness of the texture components and their shortened alignment distances in the rolling direction, PSN was the dominant nucleation mechanism.

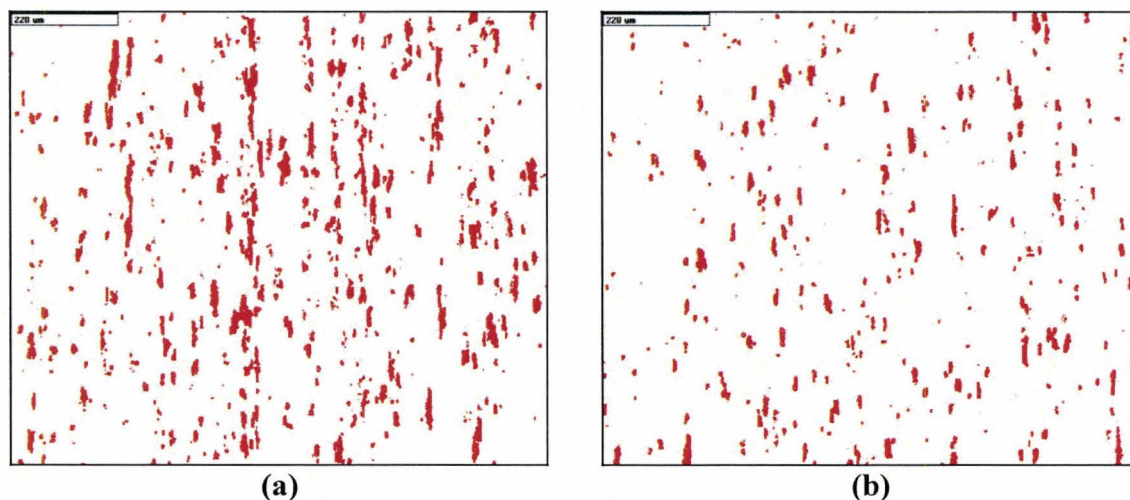


Figure 7.23: Orientation maps showing the spatial distribution of the Cube texture (a) and the Goss texture (b) for a 6111-NC-90 sample quenched from 460 °C. The RD is vertical and the ND is horizontal.

7.5.2 Effect of Fe and Mn Contents

The effect of increasing Fe and Mn contents on the recrystallization microstructure and texture was also investigated. Figure 7.24 shows the orientation map for the high Fe and Mn alloy 6111-HC-90 after quenching from 500 °C. This temperature corresponds to the end of the Mg_2Si precipitation peak that immediately followed the recrystallization peak on the DSC thermograms. It is clear that recrystallization was

complete and proceeded by the formation of small grains with a mean size of 8.5 μm . The grains were relatively equiaxed with an aspect ratio of 1.4. The volume fraction recrystallized was 79.3%. Similar to the nominal composition alloy, the grains boundaries were highly jagged illustrating the strong interaction of the boundaries with the dispersed Q phase.

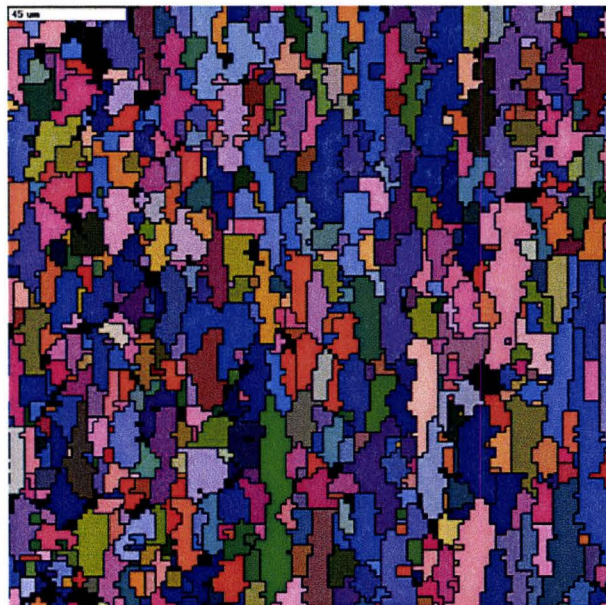


Figure 7.24: Orientation map of 6111-HC-90 quenched from 500 °C. The RD is vertical and the ND is horizontal.

Although the mean grain size was similar to the nominal composition alloy, the recrystallized microstructure was more homogeneous with a narrower grain size distribution as seen in Figure 7.25. This homogeneous nature of the microstructure is due to two factors, the higher volume fraction of the constituent particles (size $>1\mu\text{m}$) and their associated role in increasing PSN and refining the grain structure, and the additional pinning pressure on the moving boundaries exerted by the Mg_2Si precipitates as

illustrated by the TEM micrograph in Figure 7.26. It is clear from the micrograph that Mg_2Si particles precipitated preferentially on the recrystallized grain boundaries. Consequently, their pinning pressures will be greater than randomly distributed particles (Humphreys and Hatherly, 1995). This explains the lower recrystallized volume fraction in this alloy in comparison to the nominal composition variant. It is likely that a minor overlap may occur between the beginning of the Mg_2Si precipitation and the end of the recrystallization process causing its retardation.

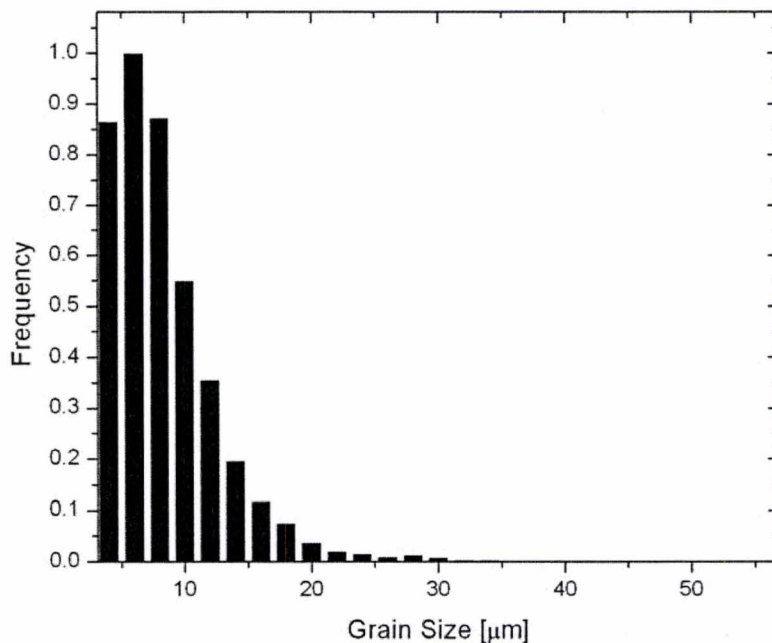


Figure 7.25: Histogram of grain size distribution in 6111-HC-90 quenched from 500 °C.

Increasing the Fe and Mn levels resulted in an increased efficiency of PSN in randomizing the recrystallization texture in the sample as seen in Figure 7.27. The banding of the cube and Goss texture components was less prevalent and with shorter

lengths in the rolling direction after recrystallization. This agrees with the results of Jin and Lloyd (2005) in AA6111 alloys where increasing Fe levels weakened the Cube texture in the recrystallized microstructures. Consequently, the inherited banded structure disappeared from the recrystallized microstructure. The above results clearly indicate that with the increased Fe and Mn contents, PSN becomes the dominant nucleation mechanism for recrystallization in AA6111 alloys and favors the competition among nucleation from Cube and/or Goss bands.

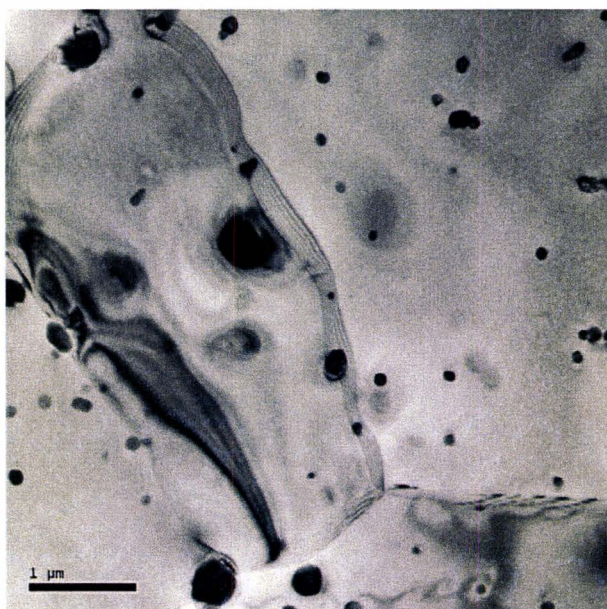


Figure 7.26: TEM micrograph of 6111-HC-90 quenched from 500 °C illustrating additional boundary pinning by Mg₂Si precipitates.

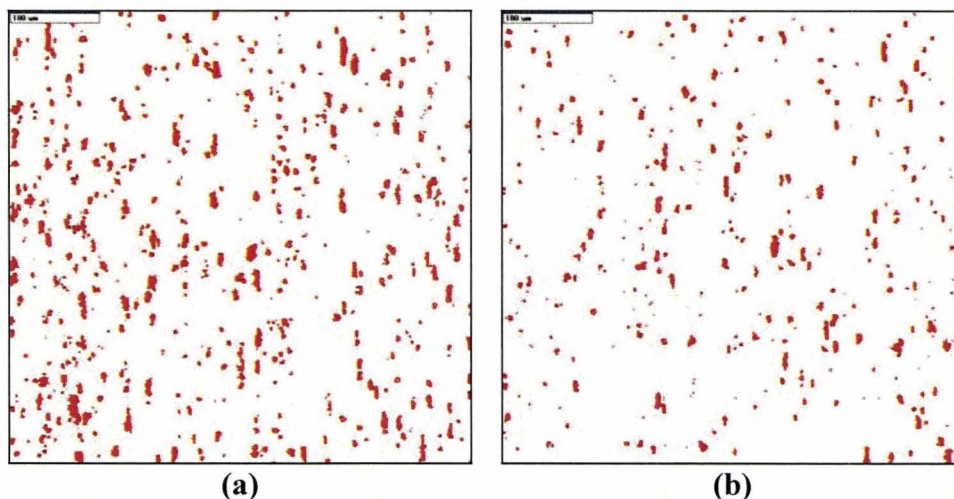


Figure 7.27: Orientation maps showing the spatial distribution of the Cube texture (a) and the Goss texture (b) for the 6111-HC-90 sample quenched from 500 °C. The RD is vertical and the ND is horizontal.

The recrystallized microstructure of the alloy with the negligible Fe and Mn contents was also investigated and the grain structure is shown in Figure 7.28. Recrystallization evolved heterogeneously with the formation of coarser grains in comparison to the previous two cases. The mean grain size was 13.11 μm and the grains were elongated in bands along the rolling direction. The recrystallized volume fraction was 65%. Similar to the nominal composition alloy, the grain size distribution was inhomogeneous and occurred over a wide range as seen in Figure 7.29. In the absence of a large volume fraction of constituent particles, nucleation of new grains is expected to occur along the existing high angle grain boundaries and preferentially from the Cube and/or Goss bands. Both nucleation mechanisms will result in heterogeneous microstructures. As for the inherited banded structure, it is obvious that it resulted from the retained Cube and Goss orientations in the recrystallized microstructure as shown in Figure 7.30.

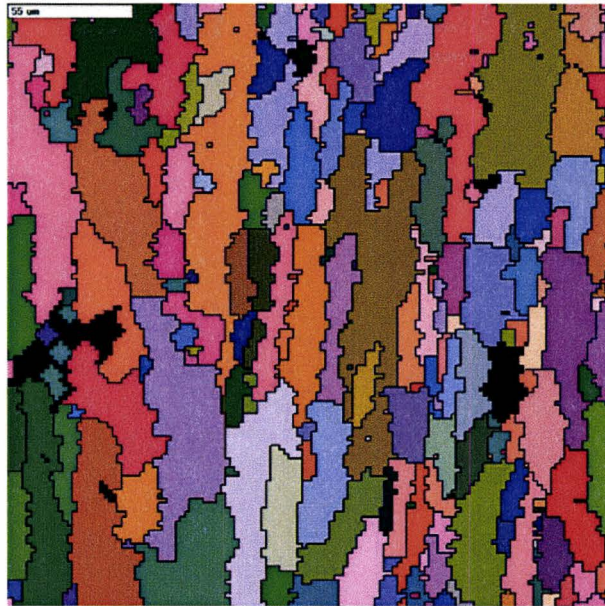


Figure 7.28: Orientation map of 6111-LC-90 quenched from 480 °C. The RD is vertical and the ND is horizontal.

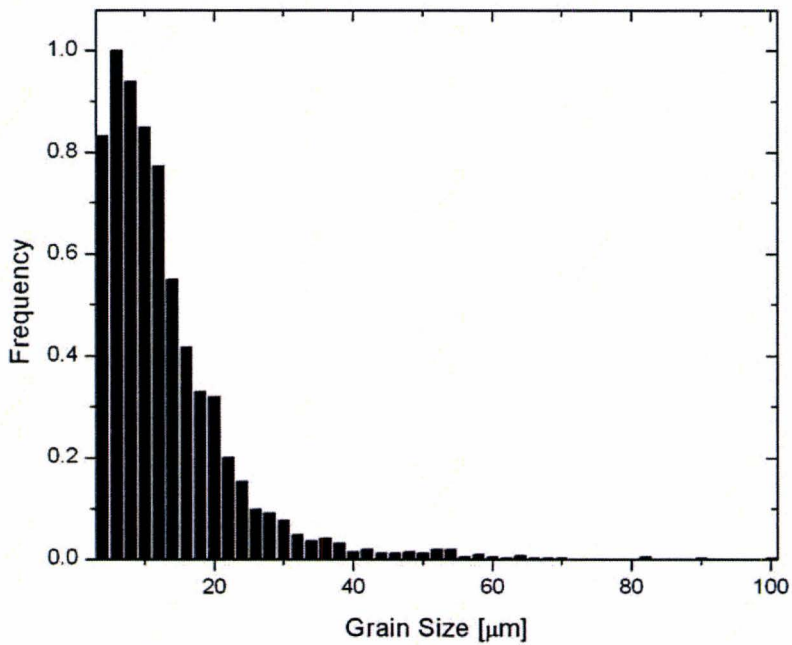


Figure 7.29: Histogram of grain size distribution in 6111-LC-90 quenched from 480 °C.

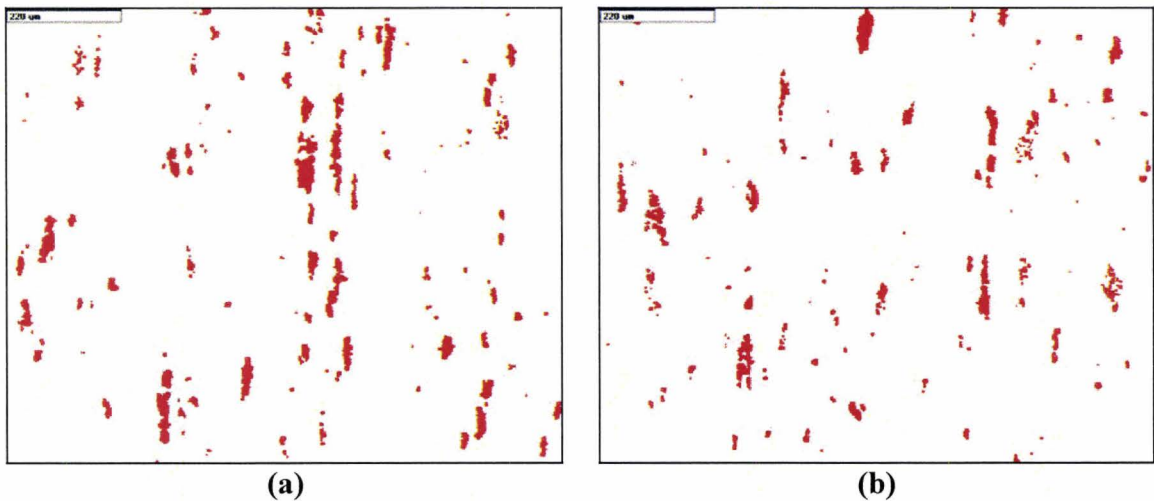


Figure 7.30: Orientation maps showing the spatial distribution of the Cube texture (a) and the Goss texture (b) for the 6111-LC-90 sample quenched from 480 °C. The RD is vertical and the ND is horizontal.

7.6 Thermo-Analytical Analysis of Calorimetric Data

Following the previous identification of the portion of the DSC heat flow curve (i.e. the peak) related to the release of stored energy in the deformed alloys. A thermo-analytical assessment of the heat flow data was performed using the procedure outlined in section 5.4.4. The starting point in the procedure includes a visual selection of a beginning and end point for the peak corresponding to the onset and end temperature of the recrystallization process, respectively. The fortran code is then invoked in constructing a baseline by cubic splines between these two chosen temperature limits. Integration of the heat flux data is then performed within the selected temperature limits yielding the stored energy of deformation from expression (5.6). The extent of the reaction (i.e. the degree of recrystallization) is then obtained from expression (5.8). The above procedure was repeated for all the investigated cold-rolled materials and for the

differently employed heating rates. Representative illustrations of the baseline construction procedure for the different alloy compositions are shown in Figure 7.31. The alloys were cold-rolled to 90% reduction and the DSC scans were performed at 40 °C/min. The figures also show a traditionally constructed baseline employing expression (5.7) as discussed in section 5.3.3.

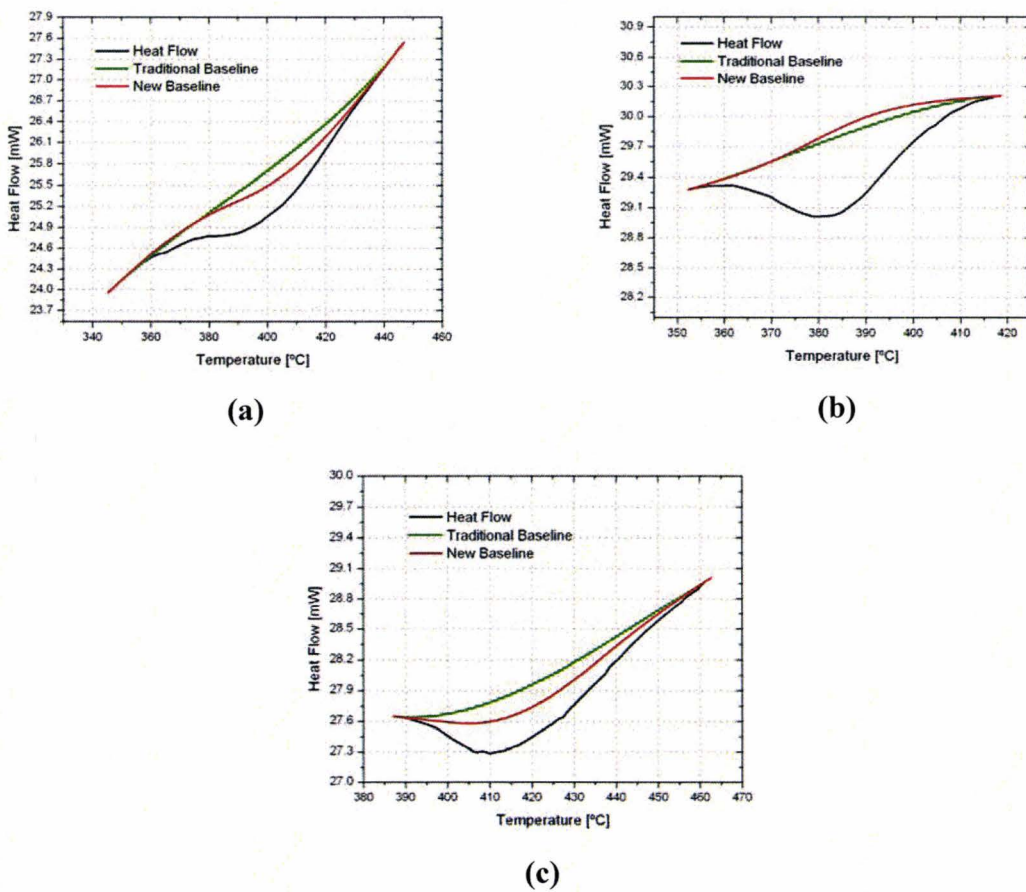


Figure 7.31: Samples of isolated recrystallization peaks with the constructed baselines for DSC scans recorded at a rate of 40 °C/min: a) 6111-NC-90, b) 6111-HC-90 and c) 6111-LC-90.

7.6.1 Recrystallization Temperature Range

The start and end temperatures of the recrystallization reaction were visually determined from the generated DSC heat flow curves. Tangents were drawn to the steady state portions of the heat flow curves in the vicinity of the recrystallization peak. The first visible deviations from the steady state conditions were then selected as an estimate of the start and end temperatures of recrystallization. Figure 7.32 shows the recorded temperature ranges for the nominal composition 6111-NC alloy as a function of heating rate and degree of deformation. Both the start and end temperature were found to increase almost linearly with the heating rate. This effect indicates rapid kinetics of the recrystallization process in the AA6111 alloys that was not kinetically limited by the fast heating rates. Similar trends were reported by Howe (1986) for the recrystallization behavior of Al–Mn alloys but the heating rates were limited to a maximum of 20 °C/min. The recrystallization reaction reached completion over a range of approximately 95 °C and the temperature range of the reaction was independent of the heating rate and the degree of deformation. However, increasing the degree of deformation shifted the onset temperature of recrystallization to lower values. This effect is attributed to the increase in the driving force for recrystallization as a result of the increased cold rolling reduction.

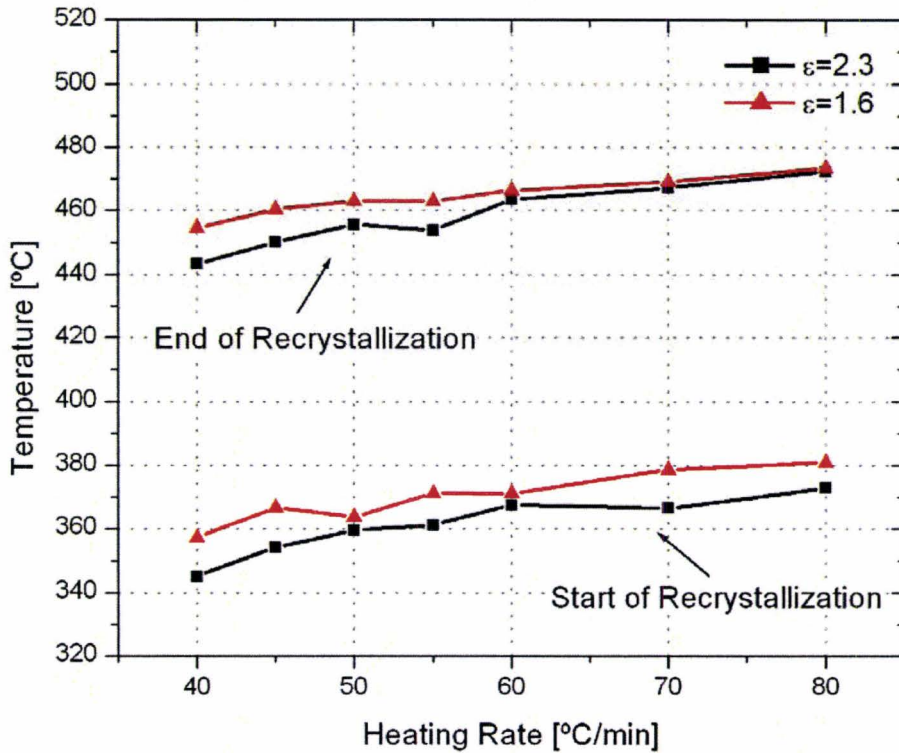


Figure 7.32: Recrystallization temperature ranges for the 6111-NC alloy as a function of heating rate and degree of deformation.

The variation of the recrystallization start and end temperatures with the heating rate and the degree of deformation for the alloys with the high and negligible Fe and Mn content followed the same trends as the nominal composition alloy as shown in Figure 7.33 and Figure 7.34, respectively. The temperature range for the recrystallization reaction was approximately 70 °C for the 6111-HC alloy and 77.5 °C for the 6111-LC alloy. Despite the close agreement between the recorded ranges for the recrystallization reaction in the three alloys, the actual volume fraction recrystallized varied between the three alloy compositions as revealed by the EBSD investigation in section 7.5. While a

fully recrystallized microstructure was observed for both the nominal composition and the high Fe and Mn content alloys, the alloy with the negligible Fe and Mn contents was only partially recrystallized. This effect indicates a strong influence of Fe and Mn additions on the recrystallization process and is summarized in Figure 7.35 which shows the dependence of the recrystallization temperature on the Fe and Mn contents and the degree of deformation. The recrystallization temperature represents the mean of the maximum rate temperatures of recrystallization (i.e. the peak temperature) recorded at different heating rates for each alloy.

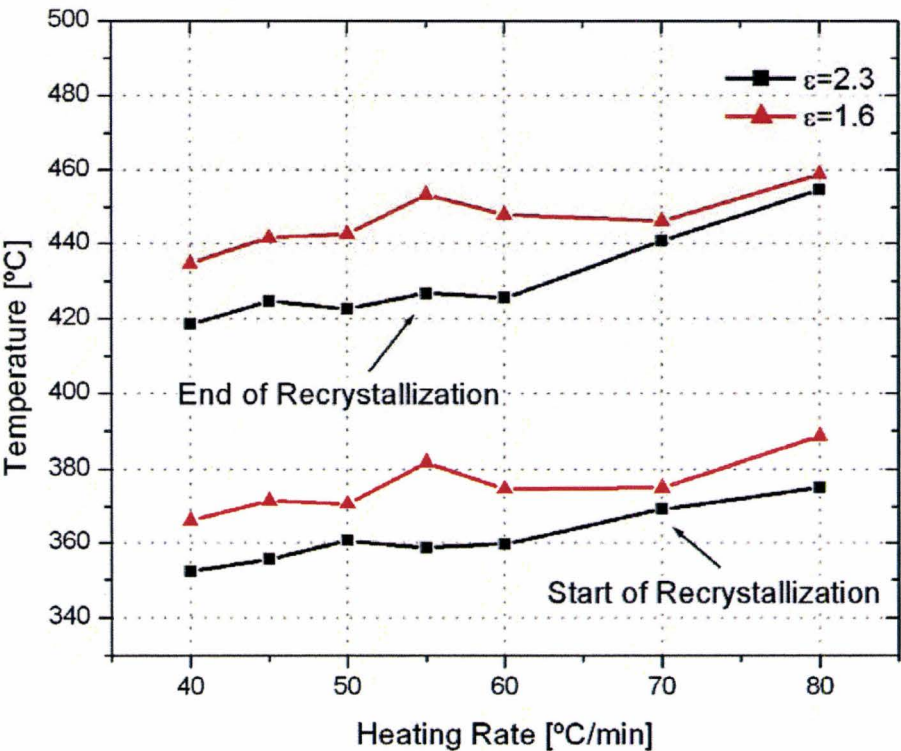


Figure 7.33: Recrystallization temperature ranges for the 6111-HC alloy as a function of heating rate and degree of deformation.

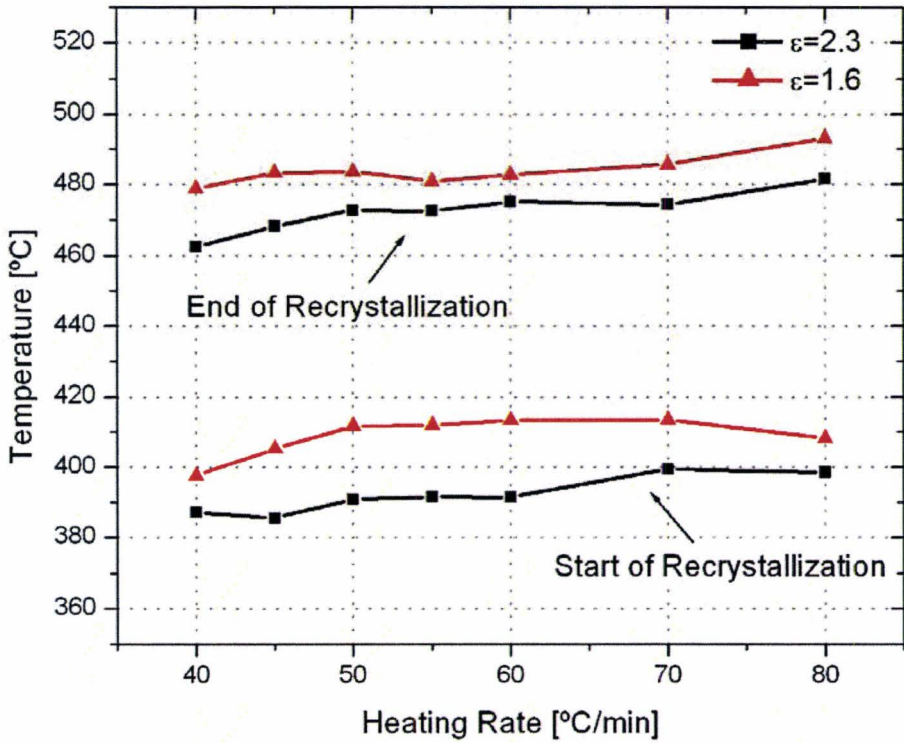


Figure 7.34: Recrystallization temperature ranges for the 6111-LC alloy as a function of heating rate and degree of deformation.

It is clear from Figure 7.35 that the recrystallization temperature shifts to lower values with the increase in the Fe and Mn levels. As indicated in section 7.5.2, both the frequency and efficiency of PSN in promoting recrystallization increases with the increase of the volume fraction of the large (>1 μm) intermetallics. Accordingly, enhanced kinetics of recrystallization is expected due to the higher density of particles acting as recrystallization nuclei especially at the early stages of recrystallization. This explains the observed variations in the onset of recrystallization (≈ 40 °C) between the

alloys with the higher Fe and Mn contents 6111-NC and 6111-HC, and the alloy with the negligible Fe and Mn contents 6111-LC as shown in Figures 7.32-7.34.

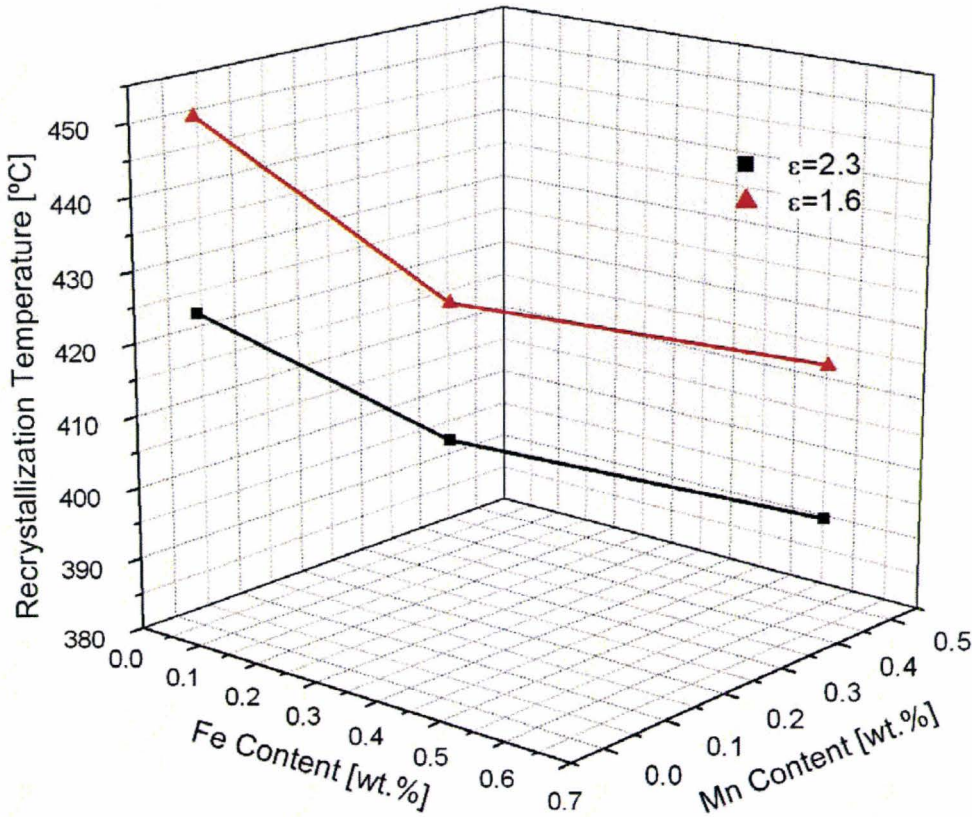


Figure 7.35: Effect of solute content and degree of deformation on the recrystallization temperature.

7.7 The Stored Energy of Deformation

The stored energy in the deformed samples was determined by integrating the heat flow curve over the whole recrystallization peak. Figure 7.36 shows the variation of stored energy with heating rate for the nominal composition alloy 6111-NC. It is evident that the stored energy is independent of the heating rate. This means that recovery activities prior to recrystallization, although not completely eliminated as observed from

the TEM micrographs and hardness measurement, were at least minimized by the employed high heating rates. Otherwise, an increase in heating rate would have resulted in an increase in the stored energy values determined from the recrystallization peak.

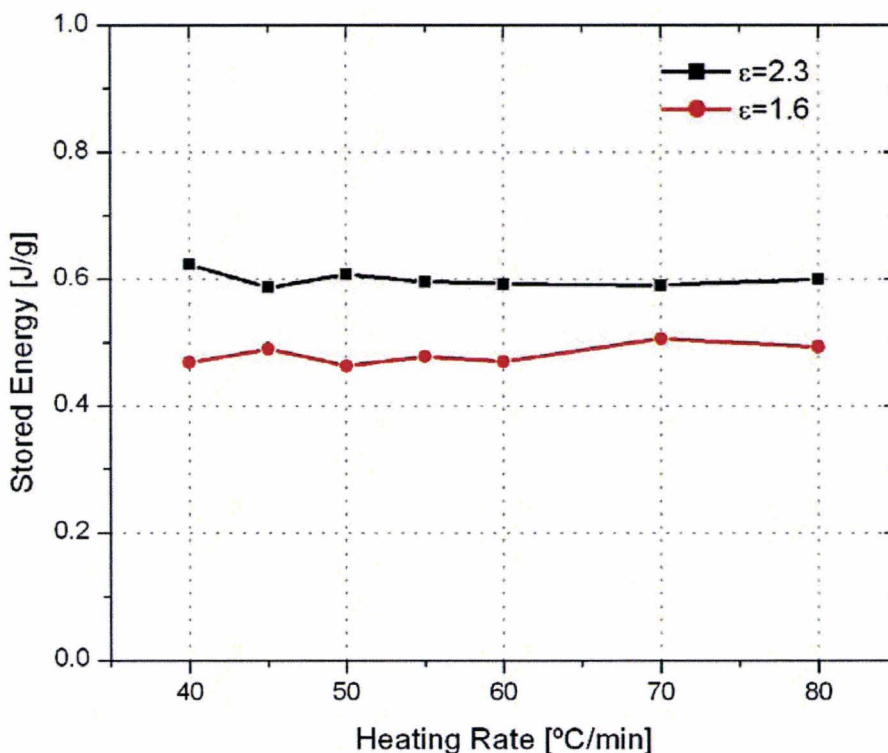


Figure 7.36: Variation of stored energy with heating rate for the 6111-NC alloy.

The invariance of the stored energy with heating rate was also observed for the alloys with the high and low Fe and Mn levels as shown in Figure 7.37 and Figure 7.38, respectively. The samples for the individual DSC scans of each alloy were randomly cut from different sections of the rolled sheets. Therefore, the nearly constant stored energy values imply a homogeneous deformation at such level of strains, at least from a macroscopic perspective. Accordingly, it is reasonable to regard the mean of the

individual measurements for each alloy as a valuable representative of the bulk stored energy of the material. Such values are listed in Table 7.1.

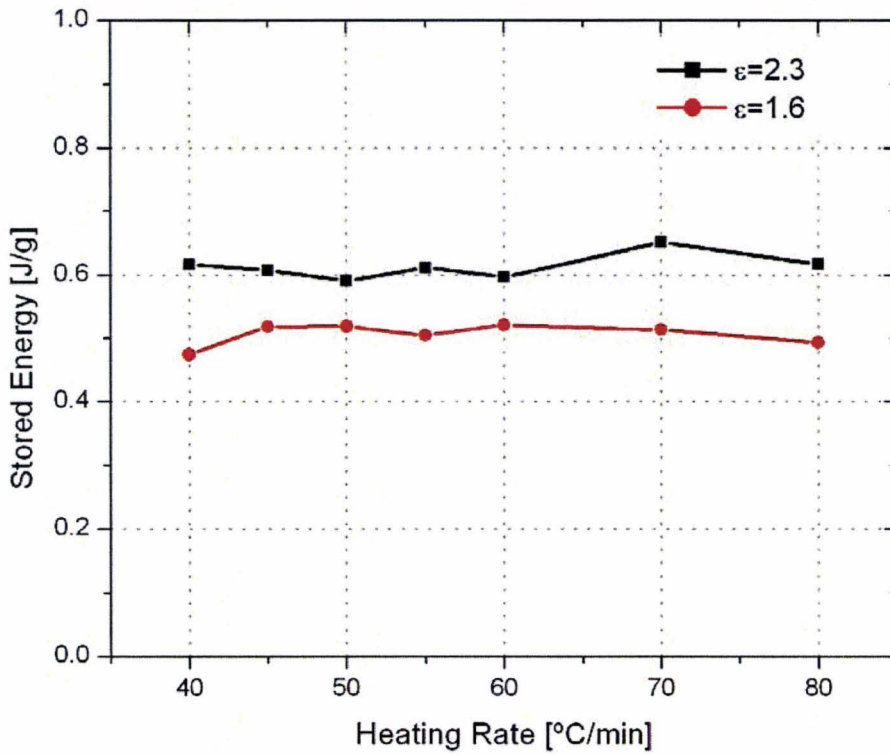


Figure 7.37: Variation of stored energy with heating rate for the 6111-HC alloy.

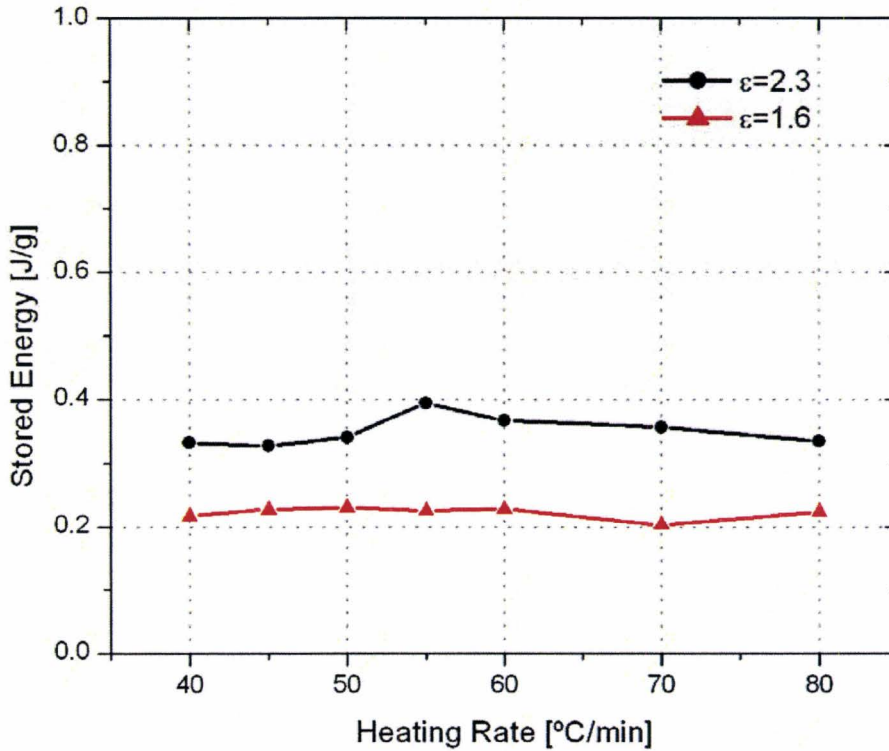


Figure 7.38: Variation of stored energy with heating rate for the 6111-LC alloy.

Table 7.1: Residual calorimetric stored energy released during recrystallization

Sample Designation	Stored Energy [J/g]
6111-NC-90	0.6
6111-NC-80	0.48
6111-HC-90	0.61
6111-HC-80	0.51
6111-LC-90	0.35
6111-LC-80	0.22

7.7.1 Effect of Solute Content and Degree of Deformation

The variation of stored energy with Fe and Mn levels for the two rolling strains is shown in Figure 7.39. The stored energy increased drastically with Fe and Mn additions up to the nominal AA6111 composition. An increase of about 71% and 117% was observed for the 90% and 80% rolled sheets, respectively. After reaching the nominal composition, increasing Fe and Mn levels did not have a significant effect on the stored energy values which seemed to tend towards a saturation level. Slight increases of 2.7% and 5.2% were observed for the 90% and 80% rolled sheets, respectively.

For the same alloy composition, increasing the thickness reduction from 80% to 90% resulted in an increase in stored energy. However, the effect was much less pronounced in comparison to compositional changes. The maximum recorded increase in stored energy was 57.2% for the alloy with the negligible Fe and Mn contents. For the remaining compositions, the increase was within 25%.

The stored energy in a material originates from the total dislocation density generated during deformation. This includes the statistically stored dislocations accumulated during the uniform deformation of the lattice and the geometrically necessary dislocations required to maintain grain boundary compatibility during deformation. In particle-containing material, additional geometrically necessary dislocations are also accumulated to accommodate the plastic strain gradient between the matrix and the non-deforming particles. Both types of dislocations increase with strain but tend to saturate at large strain levels due to a balance between dislocation

multiplication and dynamic recovery (Mandal and Baker, 1997). The statistically stored dislocations density is a characteristic of the material properties and is expected to remain fairly constant at a given strain for the three different alloy compositions. However, the geometrically necessary dislocations density increases with the decrease in grain size prior to deformation and/or the increase in the particle content (Baker et al., 1995; Mandal and Baker, 1996 & 1997). Both previous features are associated with the increase in Fe levels in AA6111 alloys (Jin and Lloyd, 2005). This explains the observed trends in Figure 7.39 and the low stored energy values for the alloy with the negligible Fe and Mn levels. Moreover, Baker et al. (1995) showed that variations in stored energy due to grain size effects are much more pronounced at low strains and gradually decrease with increasing strain until a saturation level is reached upon the formation of a cell structure. The density of dislocations along the grain boundaries then remains fairly constant and dislocations start accumulating along cell boundaries. Therefore, for the high strains employed in this study, it is expected that any significant increase in the geometrically necessary dislocation density should result from dislocations accumulating around the second-phase particles. This agrees with the drastic variation in stored energy values with the Fe and Mn additions and the lesser observed deviation in the stored energy values with rolling strains for the same alloy composition. In fact second-phase particles were shown to increase the stored energy by an amount proportional to their volume fractions (Martin et al., 1997). If for the sake of a qualitative assessment, the equilibrium amount of accumulated phases at 560 °C (the solution heat treatment temperature) as computed by Thermo-Calc in section 5.2 is used as an indicative of the volume fraction of the

second phase particles in the material. It is found that the weight percent of phases increases from 0.16% for the negligible Fe and Mn levels to 3.31% for the highest Fe and Mn additions. Such increase justifies the observed increase in the stored energy values.

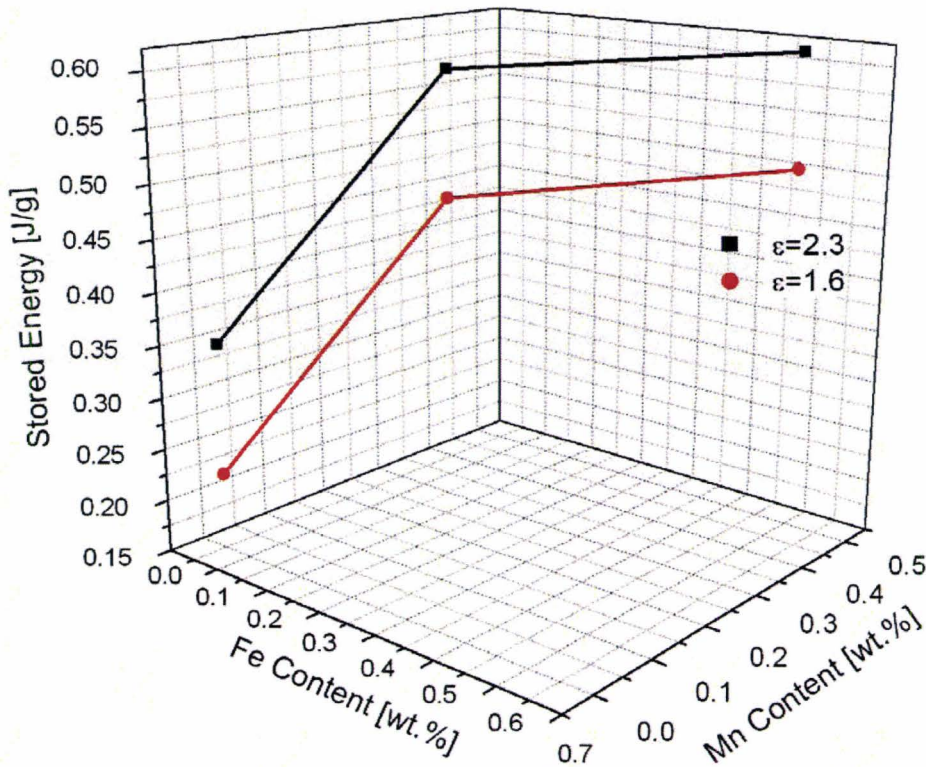


Figure 7.39: Effect of solute content and degree of deformation on the stored energy of deformation.

7.8 Recrystallization Kinetics

When discussing reaction kinetics, focus is usually directed towards the value of the activation energy rather than the preexponential factor. This is due to the ambiguous physical meaning of the preexponential factor which is merely regarded as a scaling

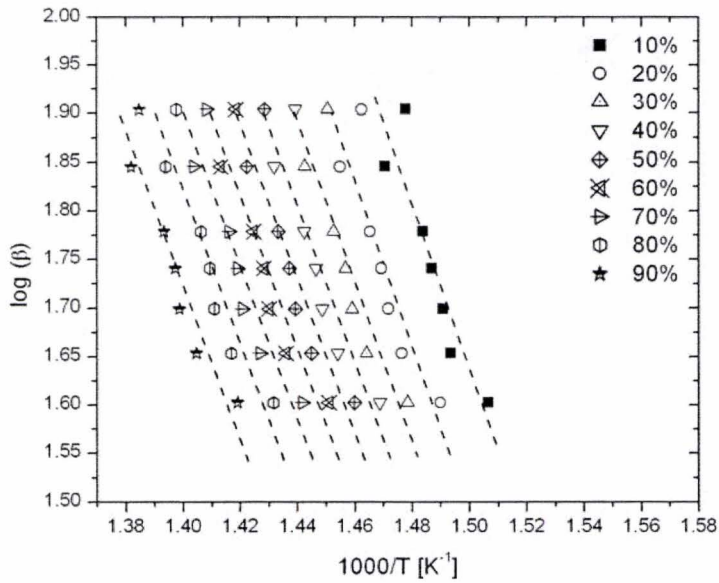
parameter determining the absolute value of the reaction rate (Vyazovkin, 2001). Moreover, the preexponential value is usually dependent on the activation energy via the compensation effect (see section 6.4.1). Therefore, values of the preexponential factor will not be discussed in this study. It should also be reminded that the activation energies determined in this study represent the overall reaction rate as measured by the DSC without an isolation of the different steps involved. As such, they include contributions from the multiple steps of the recrystallization process (ie. nucleation and growth). Therefore, they should only be regarded as effective or apparent representations of the recrystallization process.

7.8.1 Model-free Estimates of the Activation Energy of Recrystallization

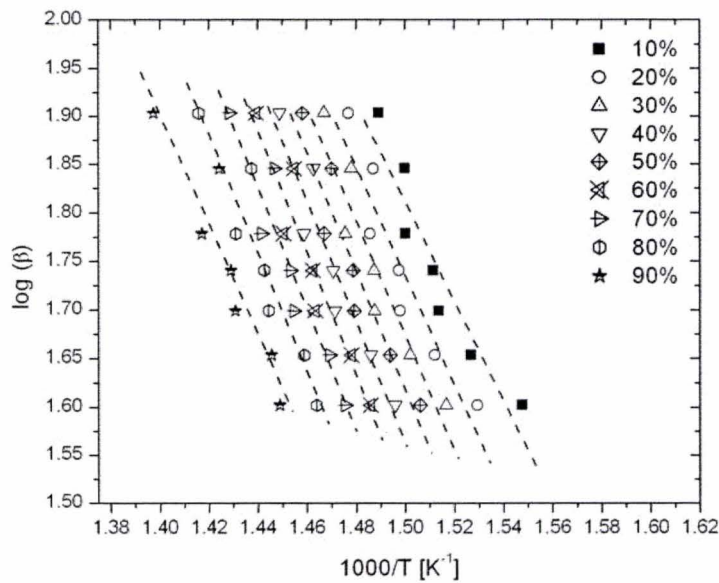
Model-free estimates of the activation energy of recrystallization in the AA6111 alloys were determined by the isoconversion Flynn-Wall-Ozawa (FWO) method described in section 6.1.2. The FWO plots and the dependence of the activation energy on the degree of recrystallization for the 6111-NC alloy are shown in Figure 7.40 and Figure 7.41, respectively. The isoconversional lines evaluated by linear regression were practically linear and parallel thus validating the basic assumption of isoconversional methods that the reaction model is independent of the heating rate (i.e. on the thermal history of the sample). Moreover, the activation energy values did not vary significantly with the degree of recrystallization within the associated experimental uncertainty. In fact, if the values corresponding to the low and high degrees of recrystallization were disregarded due to their associated inaccuracy (i.e low heat flow values), then the

activation energy for recrystallization could be represented by a single mean apparent value that is closely bound to the scatter of most of the experimental points. These mean values for the nominal composition alloy were 107.7 kJ/mol and 147.7 kJ/mol for the 90% and 80% thickness reductions, respectively. The activation energy value for the 80% thickness reduction compares favorably with the activation energy for lattice self-diffusion in aluminum and its alloys estimated at approximately 142-156 kJ/mol (Wang et al., 1996; Puchi-Cabrera et al., 2003). On increasing the effective strain to 2.3 (90% thickness reduction), the apparent activation energy for recrystallization dropped significantly to a value of 107.7 kJ/mol. Such decrease is expected in terms of the increased driving force for recrystallization. Although such value is lower than the activation energy of self-diffusion, it is just slightly higher than the activation energy for grain boundary diffusion in aluminum estimated at 86 kJ/mol.

For the alloy with the negligible Fe and Mn levels 6111-LC, the FWO plots were linear and the activation energy remained independent of the degree of recrystallization as shown in Figure 7.42 and Figure 7.43. The apparent activation energy values for recrystallization were 145.9 kJ/mol and 224 kJ/mol for the 90% and 80% thickness reductions, respectively. While the activation energy for the 90% thickness reduction is consistent with the activation energy for self-diffusion in aluminum, the much higher value for the 80% thickness reduction is in close agreement with the activation energy of bulk diffusion of Fe and Mn in aluminum estimated at 193 kJ/mol and 217 kJ/mol, respectively (Vandermeer and Jensen, 2001; Lens et al., 2005).



(a)



(b)

Figure 7.40: Flynn-Wall-Ozawa isoconversional plots for the 6111-NC alloy: a) 80% and b) 90% cold rolling reduction.

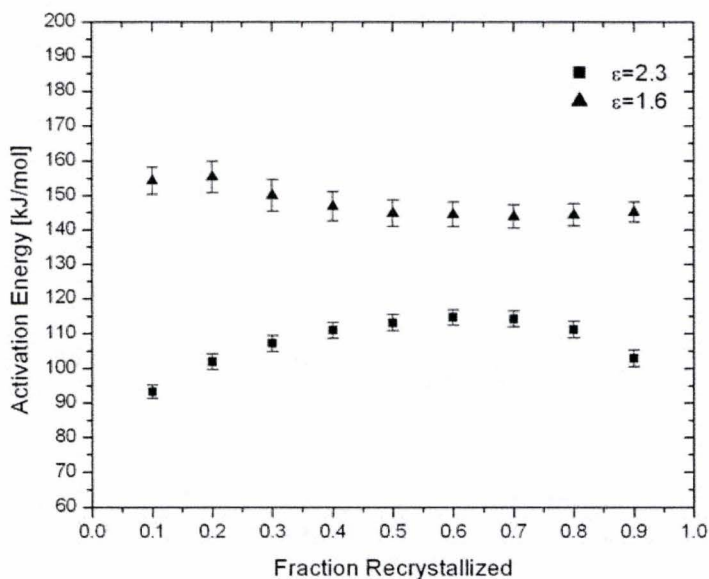
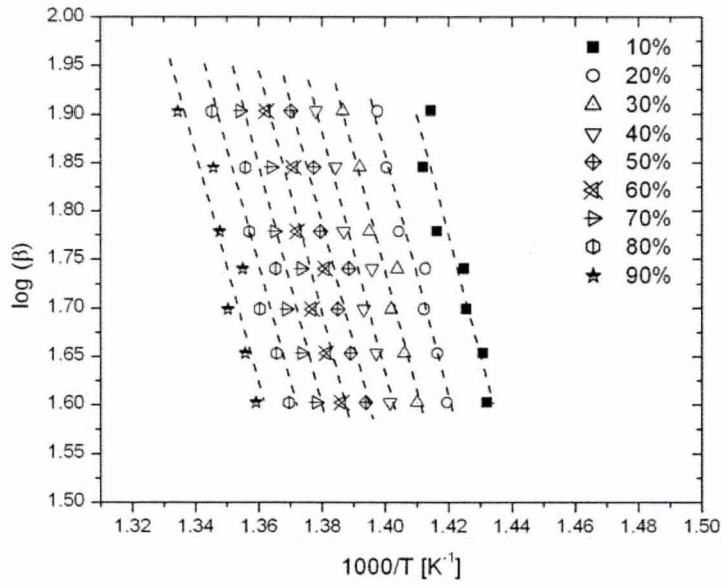


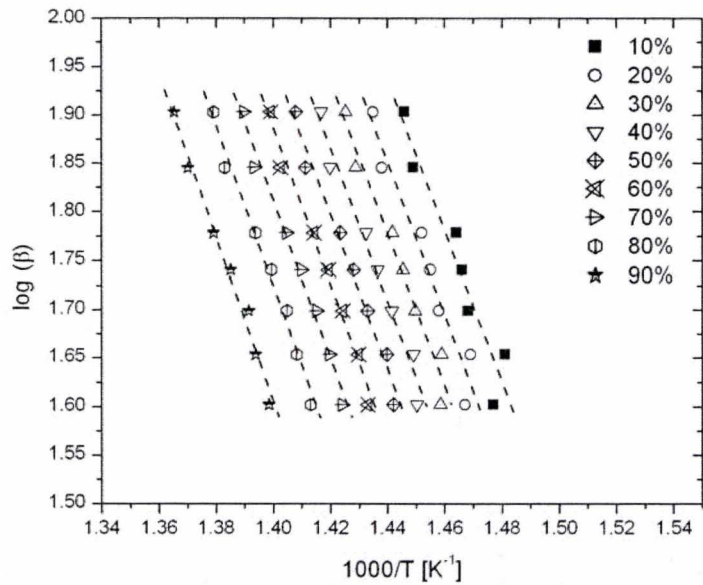
Figure 7.41: Dependence of the activation energy on extent of conversion for the 6111-NC alloy using the FWO method.

For the alloy with the high Fe and Mn content 6111-HC, the isoconversional lines in the FWO plots remained linear for the different cold rolling reductions as shown in Figure 7.44. Moreover, the activation energy was independent of the recrystallized fraction for the 80% cold rolled samples. The mean apparent activation energy value was 103.9 kJ/mol. However, a decrease in the activation energy with the fraction recrystallized was observed for the 90% cold rolled samples as seen in Figure 7.45. The activation energy values ranged from 97.3 kJ/mol at the beginning of the recrystallization process to 77.4 kJ/mol near the end. This observed dependency of the activation energy on the degree of recrystallization implies that the growth rate increases with the recrystallization progress. Such an effect is not generally expected in commercial aluminum alloys and in fact a decreasing interface migration rate of the recrystallization

front is usually observed either due to the pre-existing stored energy heterogeneities or the imposed Zener pinning pressure on the boundaries by the dispersed second-phase particles (Vandermeer et al., 1997; Vandermeer and Jensen, 2001). The combined DSC and TEM investigation of this particular alloy (see section 7.1.2) demonstrated an overlap between the end of the recrystallization process and the precipitation of Mg_2Si . Moreover, no evidence of the Q phase was visible following the end of the recrystallization peak. Both these findings, suggest an enhanced re-precipitation of the phases by the migrating recrystallization front. This in turn will be reflected by a decrease in the Zener pinning pressure with the recrystallization progress leading to an increase of the boundary migration rates. Higher average boundary migration rates are expected with any increase in the driving force for boundary mobility. This explains why the enhanced growth rates of the recrystallizing grains were more prevalent with the increase in the effective strain of the samples beyond 1.6.



(a)



(b)

Figure 7.42: Flynn-Wall-Ozawa isoconversional plots for the 6111-LC alloy: a) 80% and b) 90% cold rolling reduction.

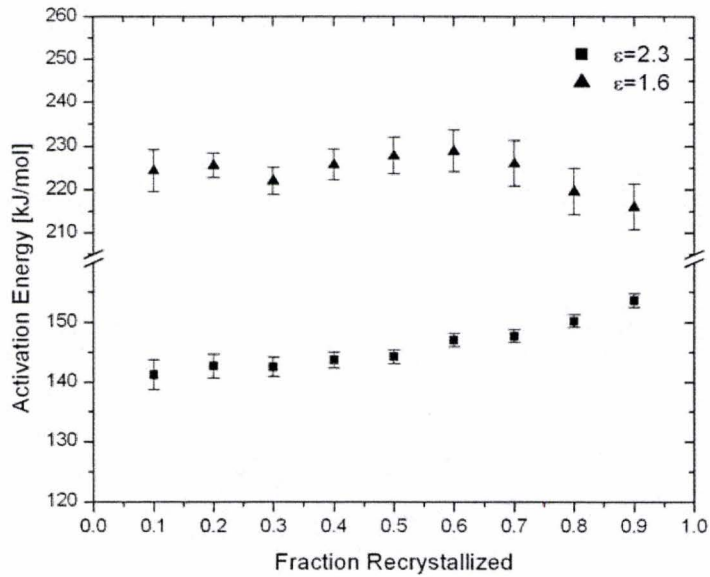
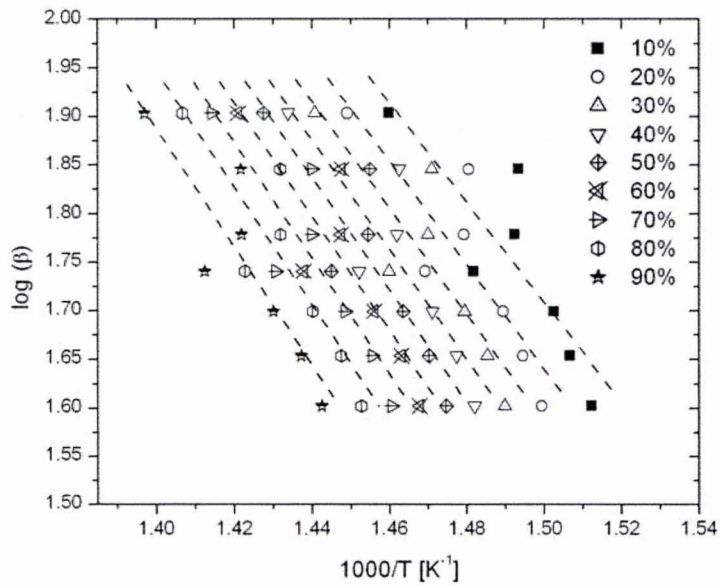
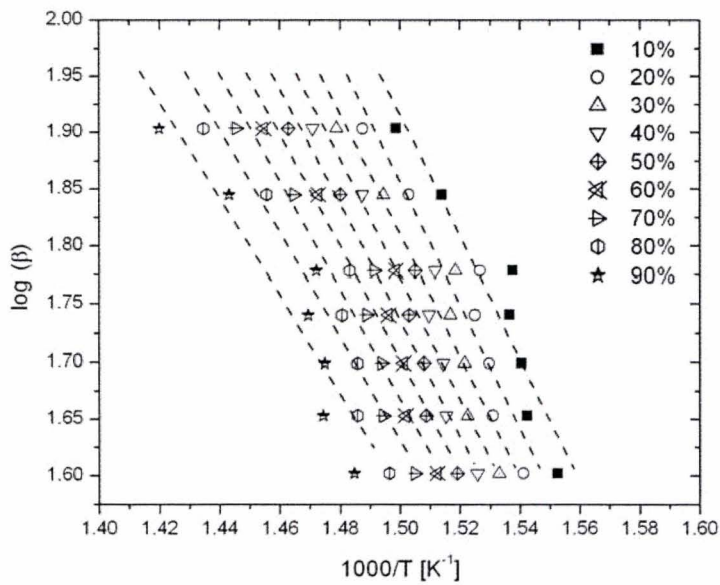


Figure 7.43: Dependence of the activation energy on extent of conversion for the 6111-LC alloy using the FWO method.

Despite the above observed variations of the activation energy values of the 6111-NC-90 alloy with the extent of conversion, reasonable agreement with the activation energy for grain boundary self-diffusivity in aluminum was still maintained. Thus, a change in the atomistic mechanism for boundary migration is not expected. Accordingly, a mean value of 90.5 kJ/mol could be regarded as a valuable representation of the apparent activation energy for recrystallization in this alloy.



(a)



(b)

Figure 7.44: Flynn-Wall-Ozawa isoconversional plots for the 6111-HC alloy: a) 80% and b) 90% cold rolling reduction.

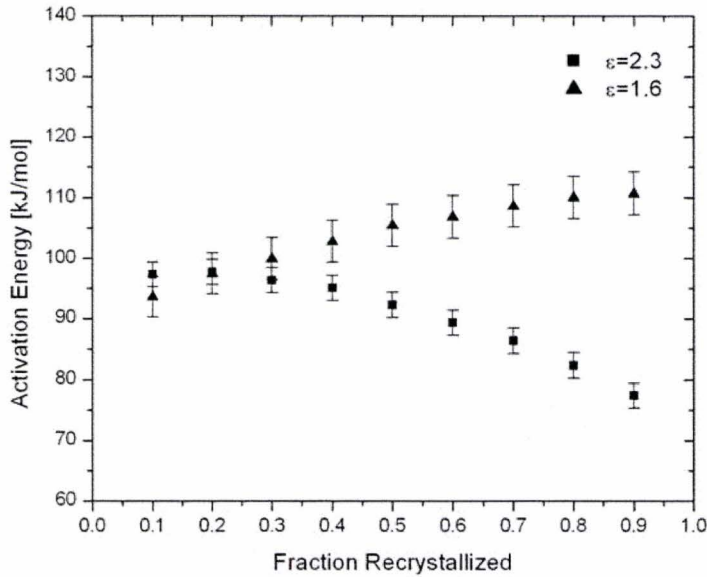
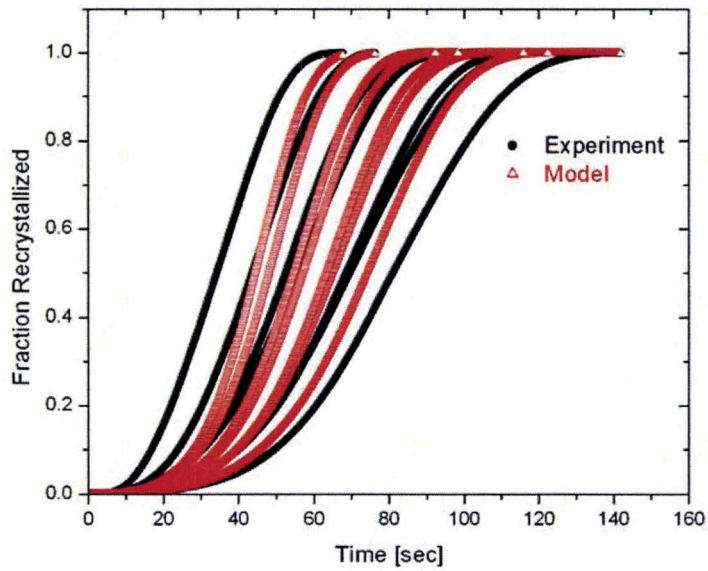


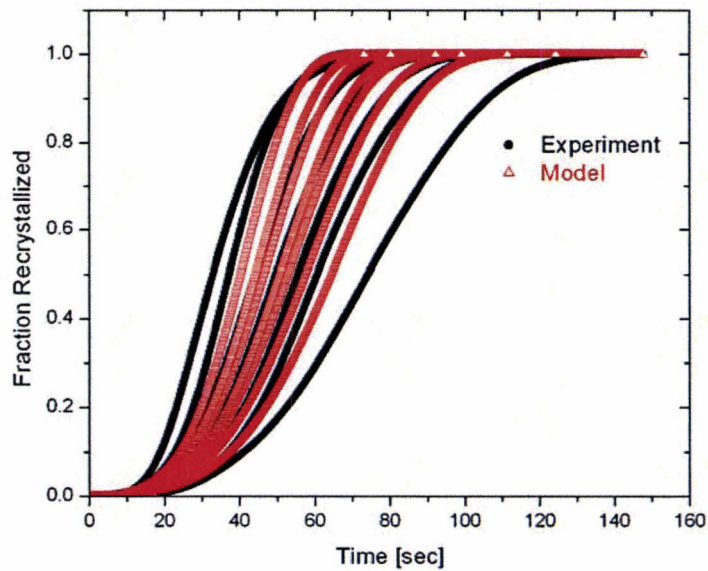
Figure 7.45: Dependence of the activation energy on extent of conversion for the 6111-HC alloy using the FWO method.

7.8.2 Formal JMAK Approach

As described in section 6.4.1, the first approach for modeling the overall recrystallization kinetics in the Al–Mg–Si–Cu alloys was based on a numerical solution of the JMAK expression derived for isothermal conditions. The experimental values of time, temperature and degree of recrystallization for each alloy were fitted simultaneously to the JMAK expression irrespective of the employed heating rate. All assumptions employed in the original derivations of the JMAK equation are implicitly assumed in this approach. Figures 7.46-7.48 show the modeling results for the three alloy compositions at the different strain levels.

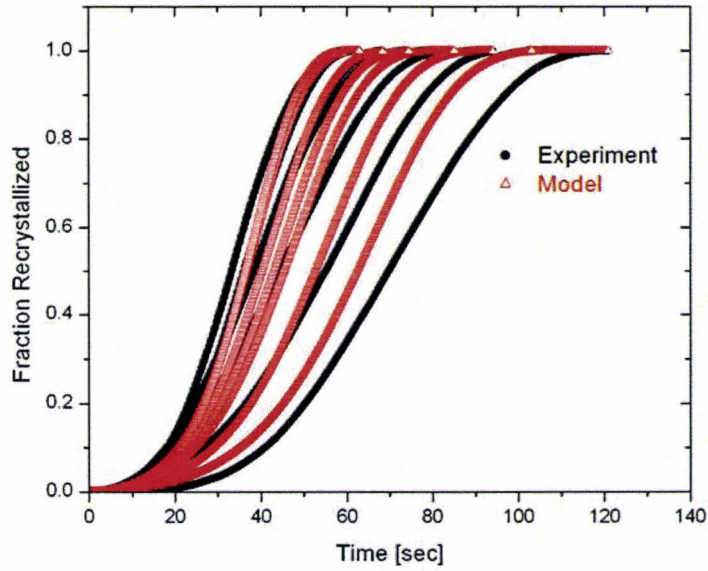


(a)

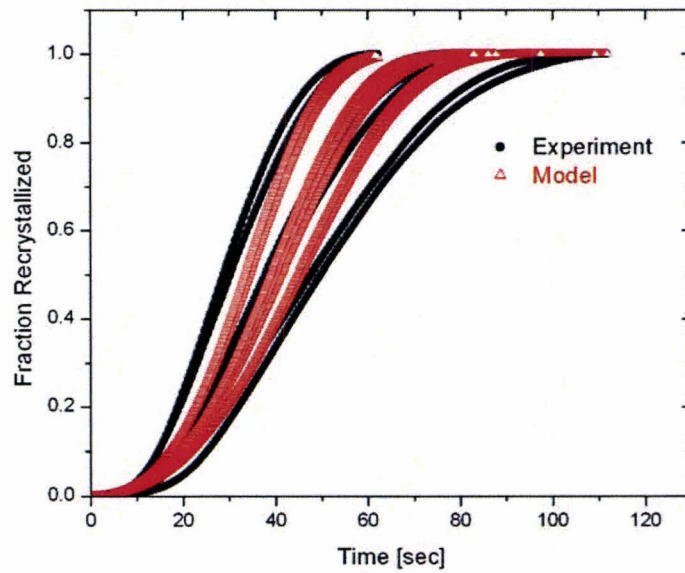


(b)

Figure 7.46: Recrystallization kinetics for the 6111-NC alloy during non-isothermal annealing at various heating rates: a) 80% and b) 90% cold rolling reduction.

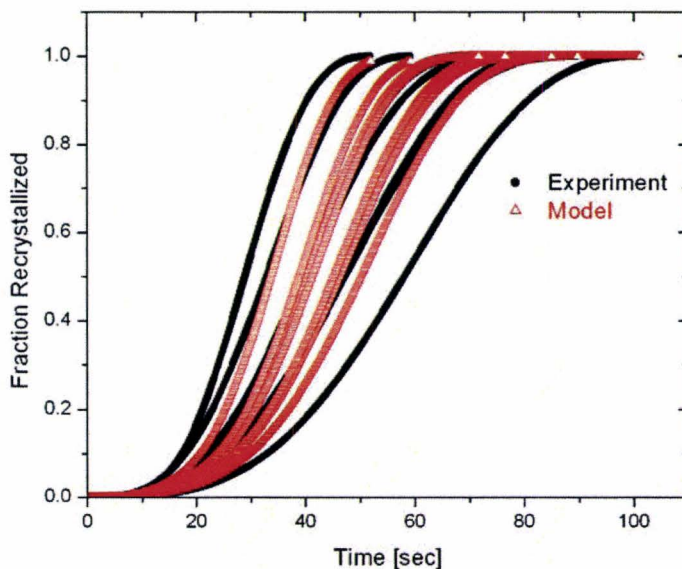


(a)

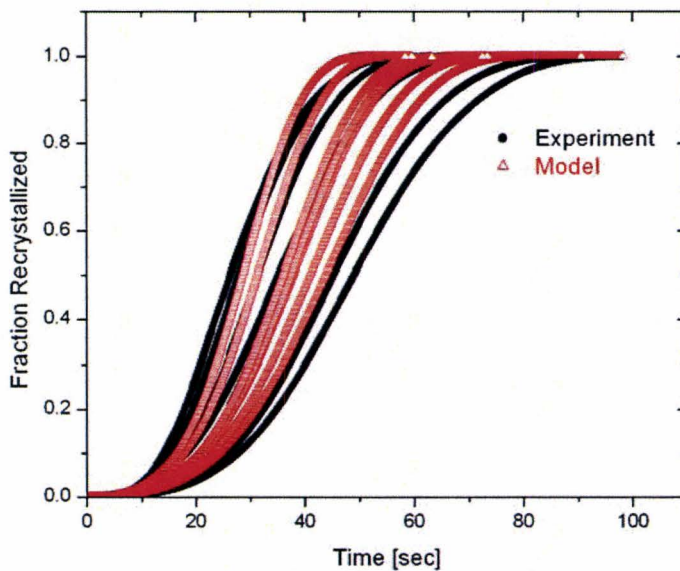


(b)

Figure 7.47: Recrystallization kinetics for the 6111-LC alloy during non-isothermal annealing at various heating rates: a) 80% and b) 90% cold rolling reduction.



(a)



(b)

Figure 7.48: Recrystallization kinetics for the 6111-HC alloy during non-isothermal annealing at various heating rates: a) 80% and b) 90% cold rolling reduction.

It is clear from the above results that the progress of recrystallization under non-isothermal conditions is not adequately described by the isothermal JMAK analysis. Despite the reproduction of the characteristic sigmoidal dependence of the transformed fraction and the good correlation between the experimental and model data for the intermediate heating rates, the accuracy of fitting for the extreme heating rate conditions was unsatisfactory. This shows that despite the extensive experimental measurements employed in the fitting procedure, the dependence of the degree of recrystallization on the temperature program was not completely eliminated. As such, the isokinetic relation which is the basic requirement for the use of the JMAK expression under non-isothermal conditions as discussed in section 6.2 was violated. Notwithstanding this fact, the kinetic parameters evaluated from the JMAK model are presented in Table 7.2. The Avrami exponent did not vary significantly with the degree of deformation but increased with the Fe and Mn additions as illustrated in Figure 7.49. As discussed in section 7.5.2, with the high Fe and Mn additions PSN tends to be the dominating recrystallization mechanism and nucleation can be regarded as site-saturated. Under such condition, the JMAK analysis predicts an Avrami exponent of 3 which is in close agreement with the 2.3 and 2.7 values observed for the alloys with the Fe and Mn additions. On the other hand, the Avrami exponent for the alloy with the negligible Fe and Mn contents ranged from 1.6-2 which agrees with typical values usually reported in recrystallization studies (see section 4.1.1). It should be reminded that nucleation by site-saturation reflects an isokinetic behavior of the transformation. This explains the improved accuracy of the JMAK modeling approach as the nucleation conditions shift towards site-saturation.

Table 7.2: Recrystallization kinetic parameters evaluated from the formal JMAK approach

Material Designation	Activation Energy [kJ/mol]	Avrami Exponent
6111-NC-80	145	2.3
6111-NC-90	112.5	2.4
6111-HC-80	123.5	2.7
6111-HC-90	120.7	2.4
6111-LC-80	214.7	1.6
6111-LC-90	98.7	2

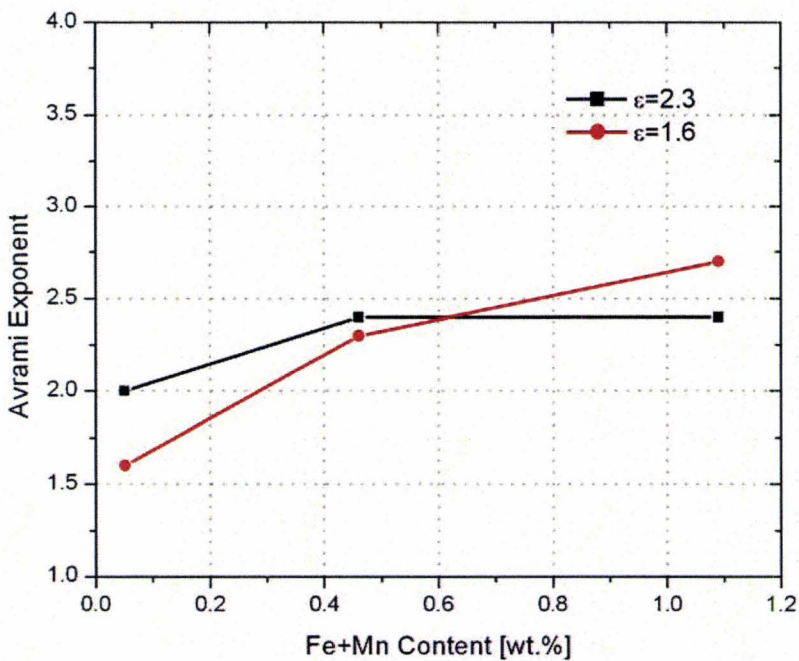
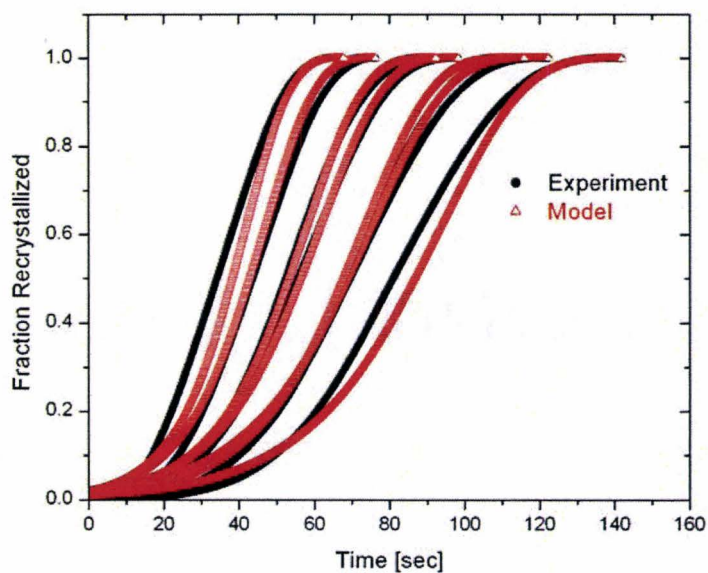


Figure 7.49: Effect of solute content and degree of deformation on the Avrami exponent evaluated from the formal JMAK approach.

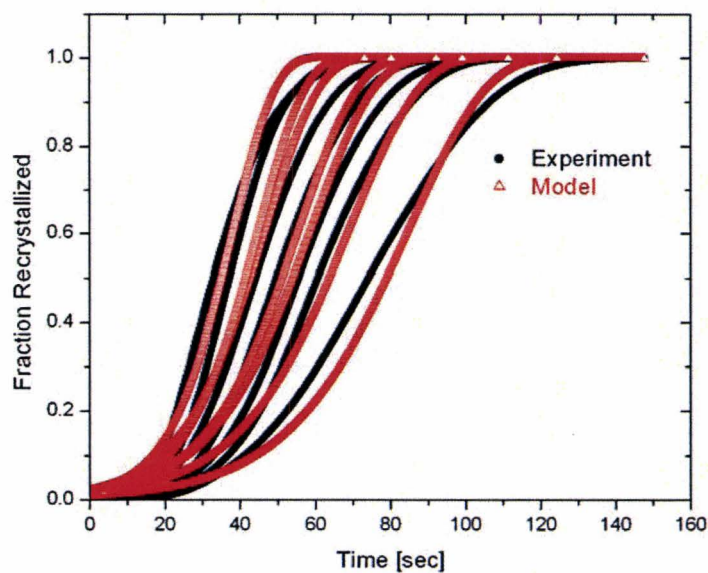
7.8.3 The Path Variable Approach

The second approach for evaluating the kinetics of recrystallization under non-isothermal conditions was based on the introduction of a path variable that depends on the thermal history of the material and that uniquely describes the progress of the reaction regardless of the employed time-temperature program. The functional form of the JMAK kinetics was assumed to hold for the recrystallization process and the degree of recrystallization was prescribed in terms of the path variable. The modeling results for the three alloys are presented in Figures 7.50-7.52. It is clear that the use of a path variable approach decreased the discrepancy of the JMAK model predictions and resulted in a better correspondence with the experimental observations. Table 7.3 summarizes the recrystallization kinetic parameters evaluated by the path variable approach. The activation energy values for recrystallization were in good agreement with the model-free estimates by the Flynn-Wall-Ozawa isoconversional method. This offers an additional validation to the use of the JMAK expression for the description of the overall recrystallization kinetics in Al-Mg-Si-Cu alloys under non-isothermal annealing conditions. However, the path variable approach still over predicts the transformation rate at higher fractions transformed. This is a common shortcoming of the JMAK kinetic description (Furu et al., 1990; Kruger and Woldt, 1992; Woldt, 2001). As discussed in section 4.1.1., the deviations are mainly due to a non-uniform distribution of the stored energy and/or a decreasing interface migration rate. Although the FWO analysis did not show a considerable deviation in the activation energy values during the course of recrystallization, grain-to-grain variations in the stored energy are still expected due to

the orientation dependence of the flow behavior (Vandermmmer and Rath, 1989a). In addition, when PSN is a potent nucleation mechanism as shown for the alloys with the Fe and Mn additions, stored energy gradients are expected in the local deformation zones around the particles (Furu et al., 1990). Moreover, the presence of the Q' and Q phases during recrystallization or the precipitation of the Mg₂Si phase at the final stages of recrystallization will significantly affect the growth rates. Any local changes in their spatial distribution will lead to an inhomogeneous Zener drag and consequently a non-constant growth rate of the recrystallization front (Furu et al., 1990). The non-uniform distribution of stored energy also accounts for the observed deviation of the Avrami exponents from the classical JMAK analysis. On the contrary to the previous results from the formal JMAK approach, a dependency of the Avrami exponent on the degree of deformation was observed in case of the path variable approach as shown in Figure 7.53. Such dependency is expected as the spatial distribution of particles in commercial aluminum alloys usually develops towards a more random configuration with the increase in rolling strains as observed by Marthinsen et al. (2003). This fulfills the basic JMAK assumption of random spatial variation of the nucleation sites and will lead to improved kinetic predictions. The Avrami exponent also increases with the Fe and Mn additions as in the case from the classical JMAK treatment. Under the favorable condition of high driving force for recrystallization and a dominating PSN nucleation mechanism (alloy 6111-HC-90), the nucleation kinetics were site-saturated with an Avrami exponent equal to 3.

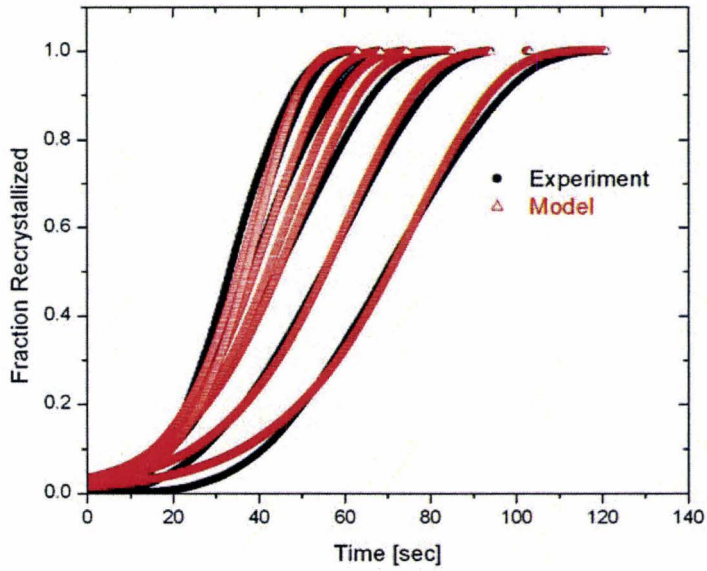


(a)

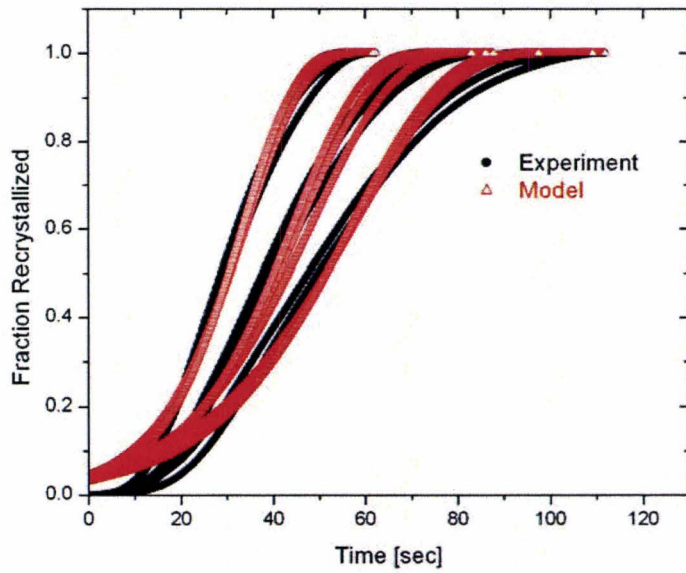


(b)

Figure 7.50: Recrystallization kinetics by the path variable approach for the 6111-NC alloy during non-isothermal annealing at various heating rates: a) 80% and b) 90% cold rolling reduction.

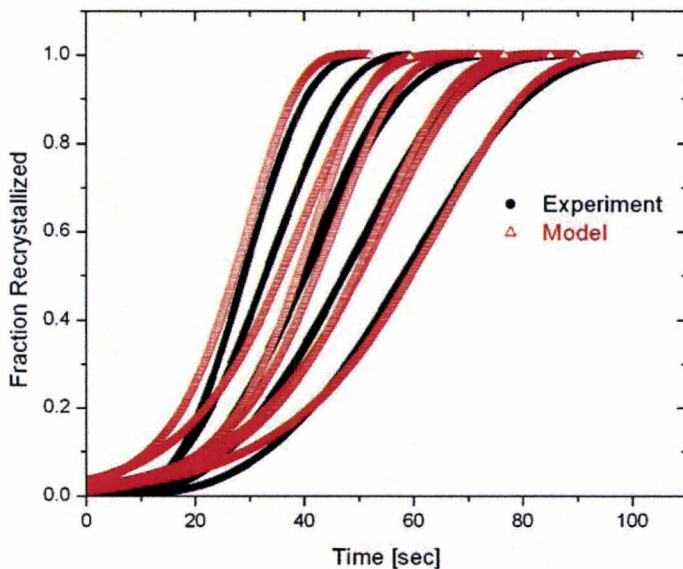


(a)

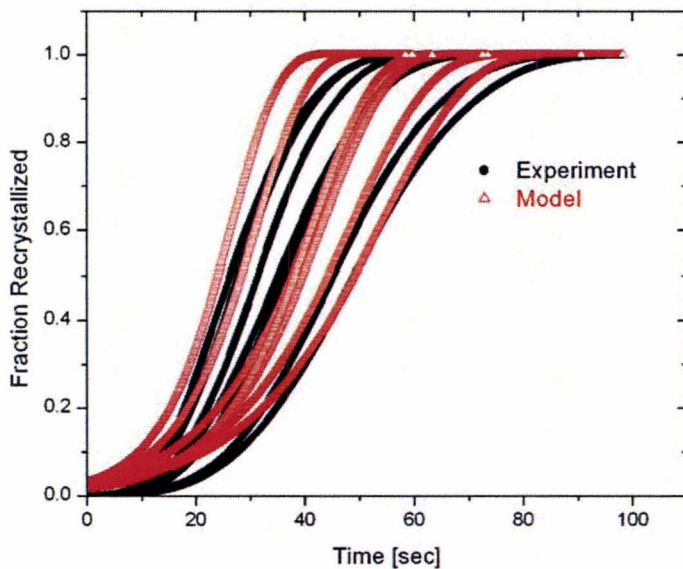


(b)

Figure 7.51: Recrystallization kinetics by the path variable approach for the 6111-LC alloy during non-isothermal annealing at various heating rates: a) 80% and b) 90% cold rolling reduction.



(a)



(b)

Figure 7.52: Recrystallization kinetics by the path variable approach for the 6111-HC alloy during non-isothermal annealing at various heating rates: a) 80% and b) 90% cold rolling reduction.

Table 7.3: Recrystallization kinetic parameters evaluated from the path variable approach

Material Designation	Activation Energy [kJ/mol]	Avrami Exponent
6111-NC-80	158.5	1.6
6111-NC-90	114.1	2.3
6111-HC-80	131	2.5
6111-HC-90	105.6	3
6111-LC-80	218.4	1.5
6111-LC-90	148.6	1.9

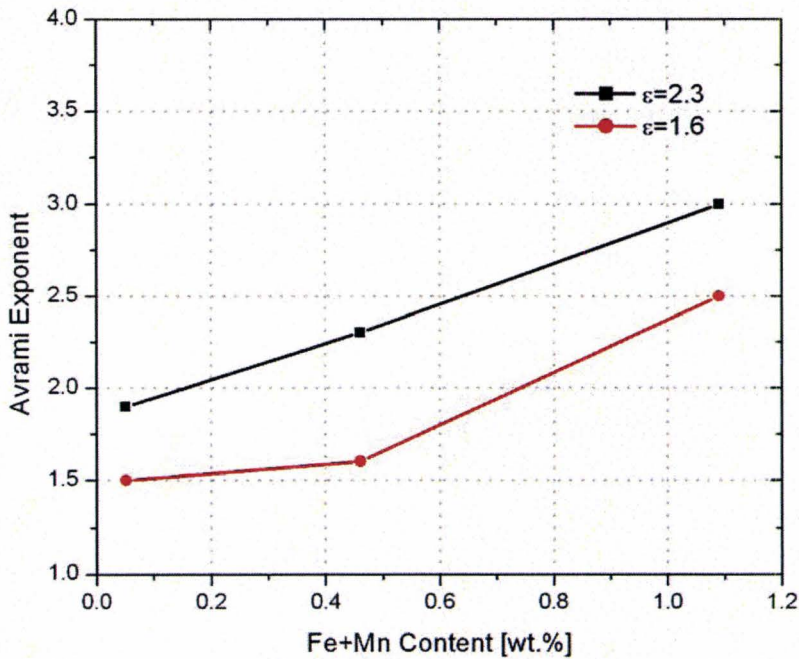


Figure 7.53: Effect of solute content and degree of deformation on the Avrami exponent evaluated from the path variable approach.

CHAPTER 8

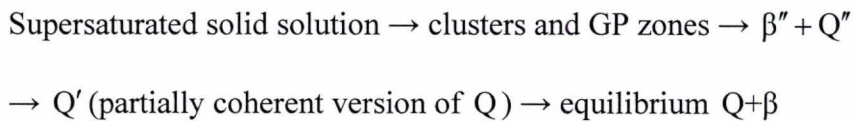
Conclusions

This research was undertaken in order to investigate recrystallization in the automotive Al–Mg–Si–Cu alloys with the intention of delineating an interaction between recrystallization and precipitation processes occurring along the whole annealing path. Differential power scanning calorimetry was selected as the main investigation technique due to the continuous nature of the recorded signal which allows the identification of phase transformations along the whole heat treatment path. Experiments were performed on solutionized and cold rolled samples under non-isothermal conditions. Heating rates varying from 40 to 80 °C/min with a 5-10 °C/min increment allowed the accumulation of a vast array of reliable experimental data suitable for a numerical modeling of recrystallization. The outcome of the calorimetric study was complemented by hardness measurements and an extensive optical and electron microscopy characterization of the alloys. The results and main contributions of the research are summarized below:

1. An investigation of intermetallic phases in the Al–Mg–Fe–Si–Mn–Cu system combined with a partial thermodynamic assessment of the Al–Fe–Si–Mn subsystem yielded more reliable thermodynamic properties of the ζ -phase

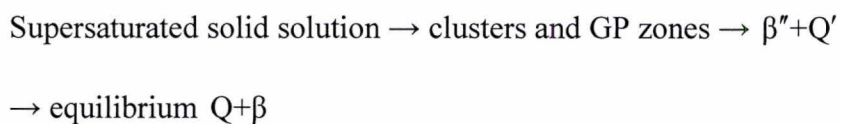
$Al_{16}(Fe,Mn)_4Si_3$, which is one of the most frequently seen intermetallics in as-cast and heat treated aluminum alloys.

2. The order of precipitation in the solutionized and quenched Al–Mg–Si–Cu alloys follows the sequence:



This sequence is in good agreement with previous investigations of alloys having similar compositions. Moderate variations of Fe and Mn concentrations do not alter this precipitation sequence, but the fraction of β'' precipitates decreases when the concentrations of Fe and Mn increase.

3. A severe deformation of solutionized and quenched Al–Mg–Si–Cu alloys alters both the kinetics and sequence of phase formation during subsequent heat treatment. The nucleation and growth of the intermediate phases β'' and Q' is accelerated by cold rolling. In addition, dislocations resulting from cold rolling promote the formation of the Q' phase instead of its metastable precursor Q'' . The precipitation sequence in a heavily deformed Al–Mg–Si–Cu alloys established in this research is:



4. The microstructure of cold rolled Al–Mg–Si–Cu alloys consists of tangled dislocations and loosely defined planar cells. A very few number of subgrains seen in the microstructure suggests that the dynamic recovery is slow. Upon annealing of the deformed samples, no separate thermal events pertaining to recovery processes are observed in the DSC thermograms. However, the microstructural examination and softening behavior indicate that recovery is still operative and precedes recrystallization over a wide temperature range. For all investigated alloy compositions, the recovery contribution to the released energy was minimized by the fast heating rates. It was ensured that the stored energy of deformation released in the calorimetric runs was independent of heating rate.

5. Recrystallization follows the precipitation of the Q' phase in the Al–Mg–Si–Cu alloys. The process goes to completion over a range of about 70-95 °C and is independent on the employed heating rates. The recrystallization temperature ranges identified by the DSC experiments were corroborated by hardness and microstructural observations. A good match between the onsets and extents of the temperature intervals within which recrystallization takes place, determined by different experimental techniques, was obtained. The Q' phase coarsens substantially and transforms to the equilibrium Q phase which then pins grain boundaries. This, in turn, leads to the formation of non-equiaxed grains with jagged boundaries. The enhanced coarsening of Q phase due to the contact with the recrystallizing interfaces results in a resaturation of solute in the Al matrix by

the end of recrystallization. This leads to an increase in the alloys strength following recrystallization.

6. With the increase of the Fe and Mn levels beyond the nominal composition, precipitation of Mg_2Si overlaps with the final stages of recrystallization. The precipitates form preferentially along the grain boundaries and exert an additional pinning effect on the migrating recrystallization fronts.
7. The strengthening characteristics of the deformed Al–Mg–Si–Cu alloys are mainly attributed to work hardening. In the course of a low-temperature annealing (below 400 °C), the hardness is controlled by the elimination of the cold-worked substructure through recovery and recrystallization without any contributions from the precipitating phases.
8. For the Al–Mg–Si–Cu alloys containing Fe and Mn, particle-stimulated nucleation (PSN) is the principal mechanism triggering recrystallization. When the concentrations of Fe and Mn are gradually decreased, nucleation in Cube or Goss bands as well as at other deformation heterogeneities may become and eventually does become an operative mechanism in the beginning of recrystallization.

9. A new method is proposed as an alternative fast and robust computational method for baseline construction utilizing interpolating cubic splines. The method is self-consistent in the sense that it is free of needless assumptions and that it provides linearity between the degree of transformation and heat measured.

10. A novel method of extracting kinetic information from non-isothermal calorimetric measurements is originated. It is based on a simultaneous fitting of all experimental triplets (time, temperature and degree of recrystallization) for the various heating rates to the classical JMAK expression with the aim of eliminating the dependency of the transformation rate on the employed temperature program. While the course of recrystallization was successfully reproduced, a good correlation between the experimental and model data was not obtained.

11. A procedure for evaluating non-isothermal measurements on the basis of a more general kinetic equation is presented. It is based on the introduction of a path variable that depends on the thermal history of the material in the JMAK kinetic description of the recrystallization process. The use of the path variable approach with a standard JMAK conversion function decreased the discrepancy of the JMAK model predictions and resulted in a more accurate description of experimental observations. The overall recrystallization kinetics conformed to the classical JMAK type behavior and the computed activation energies of

recrystallization were in good agreement with the model-free estimates by the Flynn-Wall-Ozawa isoconversional analysis.

12. The composition significantly influences the recrystallization kinetics in the Al–Mg–Si–Cu alloys. With higher Fe and Mn additions, the volume fraction of particles acting as recrystallization nuclei increases and recrystallization is promoted by an enhanced PSN frequency. Accordingly, the activation energy of recrystallization decreases and the recrystallization temperature shifts to lower values.

Bibliography

Andersen, N. H. & Jensen, D. J. (1984). Calorimetric studies of recrystallization. In N. H. Andersen, M. Eldrup, N. Hansen, D. J. Jensen, T. Leffers, H. Lilholt, O. B. Pedersen, & B. N. Singh (Eds.), *Microstructural Characterization of Materials by Non-Microscopical Techniques* (pp. 181-186). Roskilde, Denmark: Riso National Laboratory.

Avrami, M. (1939). Kinetics of phase change. I General theory. *The Journal of Chemical Physics*, 7, 1103-1112.

Baker, I., Liu, L., & Mandal, D. (1995). The effect of grain size on the stored energy of cold work as a function of strain for polycrystalline nickel. *Scripta metallurgica et materialia*, 32, 167-171.

Balitchev, E., Jantzen, T., Hurtado, I., & Neuschutz, D. (2003). Thermodynamic assessment of the quaternary system Al-Fe-Mn-Si in the Al-rich corner. *Calphad: Computer Coupling of Phase Diagrams and Thermochemistry*, 27, 275-278.

Barlock, J. G. & Mondolfo, L. F. (1975). Structure of some aluminum-iron-magnesium-manganese-silicon alloys. *Zeitschrift Fur Metallkunde*, 66, 605-611.

Bee, J. V., Jones, A. R., & Howell, P. R. (1981). The interaction of recrystallizing interfaces with intragranular precipitate dispersions in a Nickel-base superalloy. *Journal of Materials Science*, 16, 1471-1476.

Birol, Y. (2006). DSC analysis of the precipitation reactions in the alloy AA6082: Effect of sample preparation. *Journal of Thermal Analysis and Calorimetry*, 83, 219-222.

Birol, Y. (2005). Pre-straining to improve the bake hardening response of a twin-roll cast Al-Mg-Si alloy. *Scripta Materialia*, 52, 169-173.

Brooks, C. R. (1997). In J.R.Davis, G. M. Davidson, S. T. Lampman, T. B. Zorc, J. L. Daquila, A. W. Ronke, & K. L. Henniger (Eds.), *Heat Treating* (pp. 841-879). Ohio: ASM International.

Brown, M. E. (2001). *Introduction to Thermal Analysis : Techniques and Applications*. (2nd ed.) Boston: Kluwer Academic Publishers.

Bryant, J. D. (1999). Effects of preaging treatments on aging kinetics and mechanical properties in AA6111 aluminum autobody sheet. *Metallurgical and Materials Transactions A: Physical Metallurgy and Materials Science*, 30, 1999-2006.

- Budrugaec, P., Homentcovschi, D., & Segal, E. (2001). Critical analysis of the isoconversional methods for evaluating the activation energy. I. Theoretical background. *Journal of Thermal Analysis and Calorimetry*, 63, 457-463.
- Burger, G., Gupta, A. K., Sutak, L., & Lloyd, D. J. (1996). Recrystallization in a 6000-series automotive sheet alloy during solution heat treatment practice. *Materials Science Forum*, 217-222, 471-478.
- C.D.Doyle (1961). Kinetic analysis of thermogravimetric data. *Journal of Applied Polymer Science*, 5, 285-292.
- Cahn, J. W. (1956). Transformation kinetics during continuous cooling. *Acta Metallurgica*, 4, 572-575.
- Cerri, E. & Leo, P. (2005). Influence of severe plastic deformation on aging of Al-Mg-Si alloys. *Materials Science and Engineering A*, 410-411, 226-229.
- Chakrabarti, D. J. & Laughlin, D. E. (2004). Phase relations and precipitation in Al-Mg-Si alloys with Cu additions. *Progress in Materials Science*, 49, 389-410.
- Chen, D., Green, A., & Dollimore, D. (1996). DSC: the importance of baseline calibration. *Thermochimica Acta*, 284, 429.
- Christian, J. W. (1975). *The Theory of Transformations in Metals and Alloys: an Advanced Textbook in Physical Metallurgy*. Oxford: Pergamon Press.
- Claves, S. R., Elias, D. L., & Misiolak, W. Z. (2002). Analysis of the intermetallic phase transformation occurring during homogenization of 6xxx aluminum alloys. *Materials Science Forum*, 396-402, 667-674.
- Cumbrera, F. L. & Sánchez-Bajo, F. (1995). The use of the JMAKY kinetic equation for the analysis of solid-state reactions: critical considerations and recent interpretations. *Thermochimica Acta*, 266, 315-330.
- Deschamps, A., Livet, F., & Bréchet, Y. (1999). Influence of predeformation on ageing in an Al-Zn-Mg alloy-I. Microstructure evolution and mechanical properties. *Acta Materialia*, 47, 281-292.
- Doherty, R. D. (1982). Role of interfaces in kinetics of internal shape changes. In *Metal Science* (pp. 1-13). Teddington, Engl.
- Doherty, R. D., Kashyap, K., & Panchanadeeswaran, S. (1993). Direct observation of the development of recrystallization texture in commercial purity aluminum. *Acta Metallurgica et Materialia*, 41, 3029-3053.

Doherty, R. D., Li, K., Samajdar, I., Rollett, A. D., Suni, J. P., & Shuey, R. T. (1997). Modeling of recrystallization: An overview of some recent studies. In T. R. McNelley (Ed.), *Proceedings of ReX'96, the Third International Conference on Recrystallization and Related Phenomena* (pp. 69-81). Monterey, California: Monterey Institute for Advanced Studies.

Dupuy, J., Leroy, E., & Maazouz, A. (2000). Determination of activation energy and preexponential factor of thermoset reaction kinetics using differential scanning calorimetry in scanning mode: influence of baseline shape on different calculation methods. *Journal of Applied Polymer Science*, 78, 2262-2271.

Engler, O. & Hirsch, J. (2002). Texture control by thermomechanical processing of AA6xxx Al-Mg-Si sheet alloys for automotive applications - a review. *Materials Science and Engineering A*, 336, 249-262.

Erukhimovitch, V. & Baram, J. (1994). Crystallization kinetics. *Physical Review B (Condensed Matter)*, 50, 5854-5856.

Erukhimovitch, V. & Baram, J. (1996). Modeling recrystallization kinetics. *Materials Science and Engineering A*, A214, 78-83.

Esmaeili, S., Wang, X., Lloyd, D. J., & Poole, W. J. (2003). On the precipitation-hardening behavior of the Al-Mg-Si-Cu alloy AA6111. *Metallurgical and Materials Transactions A: Physical Metallurgy and Materials Science*, 34A, 751-762.

Flynn, J. H. (1997). The 'Temperature Integral' - Its use and abuse. *Thermochimica Acta*, 300, 83.

Furu, T., Marthinsen, K., Tundal, U., Ryum, N., & Nes, E. (1989). Recrystallization kinetics as studied experimentally, analytically and by computer simulation. In J. B. Bilde-Sorensen, N. Hansen, D. Juul Jensen, T. Leffers, H. Lilholt, & O. B. Pedersen (Eds.), *Materials Architecture. Proceedings of the 10th Riso International Symposium on Metallurgy and Materials Science* (pp. 343-350). Roskilde, Denmark: Riso National Laboratory.

Furu, T., Marthinsen, K., & Nes, E. (1990). Modelling recrystallisation. *Materials Science and Technology*, 6, 1093-1102.

Garcia-Cordovilla, C. & Louis, E. (1986). A differential scanning calorimetry study of recrystallization and its interaction with precipitation in Al-Fe-Si commercial alloys (AA1145 AND AA8011). *Journal of Materials Science*, 21, 971-979.

Gill, P. E., Murray, W., & Wright, M. H. (1981). *Practical optimization*. London, New York: Academic Press.

Go, J., Poole, W. J., Militzer, M., & Wells, M. A. (2003). The interaction between precipitation and recrystallization during annealing of cold rolled AA6111. *Materials Science Forum*, 426-432, 291-296.

Gokhale, A. M. & DeHoff, R. T. (1985). Estimation of nucleation rate and growth rate from time dependence of global microstructural properties during phase transformations. *Metallurgical transactions.A, Physical metallurgy and materials science*, 16 A, 559-564.

Gupta, A. K., Marois, P. H., & Lloyd, D. J. (1996). Review of the techniques for the extraction of second-phase particles from aluminum alloys. *Materials Characterization*, 37, 61-80.

Gutierrez-Urrutia, I., Munoz-Morris, M. A., & Morris, D. G. (2005). Recovery of deformation substructure and coarsening of particles on annealing severely plastically deformed Al-Mg-Si alloy and analysis of strengthening mechanisms. *Journal of Materials Research*, 21, 329-342.

Guttman, C. M. & Flynn, J. H. (1973). Drawing of the base line for differential scanning calorimetric calculation of heats of transition. *Analytical Chemistry*, 45, 408-410.

Haessner, F. (1992). Calorimetric investigation of recovery and recrystallization phenomena in metals. In R.D.Shull & A. Joshi (Eds.), *Thermal Analysis in Metallurgy* (pp. 233-257). TMS.

Hemminger, W. & Höhne, G. (1984). *Calorimetry Fundamentals and Practice*. Weinheim: Verlag Chemie.

Hemminger, W. F. & Sarge, S. M. (1991). Baseline construction and its influence on the measurement of heat with differential scanning calorimeters. *Journal of Thermal Analysis*, 37, 1455-1477.

Henderson, D. W. (1979). Thermal analysis of non-isothermal crystallization kinetics in glass forming liquids. *Journal of Non-Crystalline Solids*, 30, 301-315.

Hornbogen, E. & Koster, U. (1978). Recrystallization of two-phase alloys. In F.Haessner (Ed.), *Recrystallization of Metallic Materials* (2nd ed., pp. 159-194). Stuttgart: Riederer-Verlag.

Howe, J. M. (1986). Metallographic and differential scanning calorimetry analyses of precipitation and recrystallization in an Al-Mn alloy. *Metallurgical Transactions A (Physical Metallurgy and Materials Science)*, 17A, 593-605.

Humphreys, F. J. & Hatherly, M. (1995). *Recrystallization and Related Annealing Phenomena*. (1st ed.) New York: Pergamon.

Humphreys, F. J. (2002). VMAP (Version 8) [Computer software]. Manchester Materials Science Centre.

Humphreys, F. J. (2004). Nucleation in recrystallization. *Materials Science Forum*, 467-470, 107-116.

Janecek, M., Slamova, M., & Hajek, M. (2004). Structural transformations in continuously cast Al-Mg alloys. *Journal of Alloys and Compounds*, 378, 316-321.

Jensen, D. J. & Poulsen, H. F. (2000). Recrystallization in 3D. In N. Hansen, X. Huang, D. Juul Jensen, E. M. Lauridsen, T. Leffers, W. Pantleon, T. J. Sabin, & J. A. Wert (Eds.), *Recrystallization-Fundamental Aspects and Relations to Deformation Microstructure. Proceedings of the 21st Riso International Symposium on Materials Science* (pp. 103-124). Roskilde, Denmark: Riso National Laboratory.

Jin, H. & Lloyd, D. J. (2005). Roping in 6111 aluminum alloys with various iron contents. *Materials Science and Engineering A*, 403, 112-119.

Kemény, T. & Šesták, J. (1987). Comparison of crystallization kinetics determined by isothermal and non-isothermal methods. *Thermochimica Acta*, 110, 113-129.

Kemény, T. (1987). The evaluation of kinetic parameters from non-isothermal experiments. *Thermochimica Acta*, 110, 131-134.

Kempen, A. T. W., Sommer, F., & Mittemeijer, E. J. (2002). Determination and interpretation of isothermal and non-isothermal transformation kinetics; The effective activation energies in terms of nucleation and growth. *Journal of Materials Science*, 37, 1321-1332.

Kissinger, H. E. (1957). Reaction kinetics in differential thermal analysis. *Analytical Chemistry*, 29, 1702-1706.

Kruger, S. E., Moreau, A., Militzer, M., & Biggs, T. (2003). In-situ, laser-ultrasonic monitoring of the recrystallization of aluminum alloys. In *Materials Science Forum* (pp. 483-488). Madrid, Spain: Trans Tech Publications Ltd.

Krüger, P. & Woldt, E. (1992). The use of an activation energy distribution for the analysis of the recrystallization kinetics of copper. *Acta Metallurgica et Materialia*, 40, 2933-2942.

- Krüger, P. (1993). On the relation between non-isothermal and isothermal Kolmogorov-Johnson-Mehl-Avrami crystallization kinetics. *Journal of the Physics and Chemistry of Solids*, 54, 1549-1555.
- Kuijpers, N. C. W., Kool, W. H., & Van der Zwaag, S. (2002). DSC study on Mg-Si phases in as cast AA6xxx. *Materials Science Forum*, 396-402, 675-680.
- Lens, A., Maurice, C., & Driver, J. H. (2005). Grain boundary mobilities during recrystallization of Al-Mn alloys as measured by in situ annealing experiments. *Materials Science and Engineering A*, 403, 144-153.
- Lillywhite, S. J., Prangnell, P. B., & Humphreys, F. J. (2000). Interactions between precipitation and recrystallization in an Al-Mg-Si alloy. *Materials Science and Technology*, 16, 1112-1120.
- Lloyd, D. J., Evans, D. R., & Gupta, A. K. (2000). Precipitation reactions and the Differential Scanning Calorimetry response of AA6111 alloy. *Canadian Metallurgical Quarterly*, 39, 475-482.
- Malakhov, D. V. & Abou Khatwa, M. K. (2007). Constructing a self-consistent integral baseline by using cubic splines. *Journal of Thermal Analysis and Calorimetry*, 87, 595-599.
- Mandal, D. & Baker, I. (1996). The influence of grain boundaries on the stored energy of cold-work and recrystallization kinetics. *Materials Science Forum*, 207-209, 521-524.
- Mandal, D. & Baker, I. (1997). On the effect of fine second-phase particles on primary recrystallization as a function of strain. *Acta Materialia*, 45, 453-461.
- Marthinsen, K., Daaland, O., Furu, T., & Nes, E. (2003). The spatial distribution of nucleation sites and its effect on recrystallization kinetics in commercial aluminum alloys. *Metallurgical and Materials Transactions A: Physical Metallurgy and Materials Science*, 34, 2705-2715.
- Martin, J. W., Doherty, R. D., & Cantor, B. (1997). *Stability of Microstructure in Metallic Systems*. (2 ed.) Cambridge: Cambridge University Press.
- Matsuda, K., Uetani, Y., Sato, T., & Ikeno, S. (2001). Metastable phases in an Al-Mg-Si alloy containing copper. *Metallurgical and Materials Transactions A: Physical Metallurgy and Materials Science*, 32, 1293-1299.
- Málek, J. (1992). The kinetic analysis of non-isothermal data. *Thermochimica Acta*, 200, 257-269.

Miao, W. F. & Laughlin, D. E. (2000). A Differential scanning calorimetry study of aluminum alloy 6111 with different pre-aging treatments. *Journal of Materials Science Letters*, 19, 201-203.

Miao, W. F. & Laughlin, D. E. (2000). Effects of Cu content and preaging on precipitation characteristics in aluminum alloy 6022. *Metallurgical and Materials Transactions A: Physical Metallurgy and Materials Science*, 31A, 361-371.

Michaelsen, C., Dahms, M., & Pffuff, M. (1996). Comment on "Crystallization kinetics". *Physical Review B: Condensed Matter*, 53, 11877.

Miller, W. S., Zhuang, L., Bottema, J., Wittebrood, A. J., De Smet, P., Haszler, A. et al. (2000). Recent development in aluminum alloys for the automotive industry. *Materials Science and Engineering A: Structural Materials: Properties, Microstructure and Processing*, 280, 37-49.

Miodownik, M. A. (2002). A review of microstructural computer models used to simulate grain growth and recrystallisation in aluminium alloys. *Journal of Light Metals*, 2, 125-135.

Mittemeijer, E. J. (1992). Review analysis of the kinetics of phase transformations. *Journal of Materials Science*, 27, 3977-3987.

Myhr, O. R., Furu, T., & Bardal, A. (1997). The effect of small particles on recrystallization kinetics in commercial aluminum alloys. In T. R. McNelley (Ed.), *Proceedings of ReX'96, the Third International Conference on Recrystallization and Related Phenomena* (pp. 163-171). Monterey, California: Monterey Institute for Advanced Studies.

Nes, E., Vatne, H. E., Pettersen, T., Furu, T., & Marthinsen, K. (2000). Modelling of recrystallization applied to industrial processing of aluminium alloys. In N. Hansen, X. Huang, D. Juul Jensen, E. M. Lauridsen, T. Leffers, W. Pantleon, T. J. Sabin, & J. A. Wert (Eds.), *Recrystallization-Fundamental Aspects and Relations to Deformation Microstructure. Proceedings of the 21st Riso International Symposium on Materials Science* (pp. 139-155). Roskilde, Denmark: Riso National Laboratory.

Orsund, R. & Nes, E. (1988). Model for the nucleation of recrystallization from particles: the texture aspect. *Scripta Metallurgica*, 22, 671-676.

Ozawa, T. (1971). Kinetics of non-isothermal crystallization. *Polymer*, 12, 150-158.

Ozawa, T. (1986). Applicability of Friedman plot. *Journal of Thermal Analysis and Calorimetry*, 31, 547-551.

Ozawa, T. (1984). Nonisothermal kinetics of crystal growth from preexisting nuclei. *Bulletin of the Chemical Society of Japan*, 57, 639-643.

Ozawa, T. (1992). Estimation of activation energy by isoconversion methods. *Thermochimica Acta*, 203, 159-165.

Paillard, P. & Humphreys, F. J. (1996). The Influence of particle distribution on the recrystallization of Al-4%Cu alloys. *Materials Science Forum*, 217-222, 511-516.

Perovic, A., Perovic, D. D., Weatherly, G. C., & Lloyd, D. J. (1999). Precipitation in aluminum alloys AA6111 and AA6016. *Scripta Materialia*, 41, 703-708.

Phragmen, G. (1950). On the phases occurring in alloys of aluminum with copper, magnesium, manganese, iron and silicon. *Journal of the Institute of Metals*, 77, 489-553.

Puchi-Cabrera, E. S., Villalobos-Gutierrez, C. J., Carrillo, A., & Di Simone, F. (2003). Non-isothermal annealing of a cold rolled commercial twin roll cast 3003 aluminum alloy. *Journal of Materials Engineering and Performance*, 12, 261-271.

Quainoo, G. K. & Yannacopoulos, S. (2004). The effect of cold work on the precipitation kinetics of AA6111 aluminum. *Journal of Materials Science*, 39, 6495-6502.

Ravi, C. & Wolverton, C. (2005). Comparison of thermodynamic databases for 3xxx and 6xxx aluminum alloys. *Metallurgical and Materials Transactions A: Physical Metallurgy and Materials Science*, 36, 2013-2023.

Riontino, G., Ferro, G. L., Lussana, D., & Massazza, M. (2005). The use of DSC in describing the structure evolution of an AlZnMg alloy. *Journal of Thermal Analysis and Calorimetry*, 82, 83-87.

Rollett, A. D., Srolovitz, D. J., Anderson, M. P., & Doherty, R. D. (1992). Computer simulation of recrystallization. III. Influence of a dispersion of fine particles. *Acta Metallurgica et Materialia*, 40, 3475-3495.

Ruitenbergh, G., Woldt, E., & Petford-Long, A. K. (2001). Comparing the Johnson-Mehl-Avrami-Kolmogorov equations for isothermal and linear heating conditions. *Thermochimica Acta*, 378, 97-105.

Schönborn, K. H. & Haessner, F. (1985). Kinetics of nucleation and growth reactions investigated by differential scanning calorimetry. *Thermochimica Acta*, 86, 305-320.

Simon, P. (2004). Isoconversional methods. Fundamentals, meaning and application. *Journal of Thermal Analysis and Calorimetry*, 76, 123-132.

Srolovitz, D. J., Grest, G. S., & Anderson, M. P. (1986). Computer simulation of recrystallization - I. Homogeneous nucleation and growth. *Acta Metallurgica*, 34, 1833-1845.

Srolovitz, D. J., Grest, G. S., Anderson, M. P., & Rollett, A. D. (1988). Computer simulation of recrystallization - II. Heterogeneous nucleation and growth. *Acta Metallurgica*, 36, 2115-2128.

Starink, M. J. (2004). Analysis of aluminium based alloys by calorimetry: Quantitative analysis of reactions and reaction kinetics. *International Materials Reviews*, 49, 191-226.

Starke, E. A. (1989). Heat-treatable aluminum alloys. In A.K.Vasudevan & R. D. Doherty (Eds.), *Treatise on Materials Science and Technology, Vol. 31* (pp. 35-63). Toronto: Academic Press, Inc.

Tanaka, H. (1995). Thermal analysis and kinetics of solid state reactions. *Thermochimica Acta*, 267, 29.

Tiryakioglu, M. & Staley, J. (2003). Physical metallurgy and the effect of alloying addition in aluminum alloys. In G.E.Totten & M. Scott (Eds.), *Handbook of Aluminum. Volume 1: Physical Metallurgy and Processes* (1st ed., pp. 81-210). New York: Marcel Dekker AG.

Van der Plaats, G. (1984). A theoretical evaluation of a heat-flow differential scanning calorimeter. *Thermochimica Acta*, 72, 77-82.

Vandermeer, R. A. (1995). Analytical modeling of the kinetics of recrystallization. In N. Hansen, D. Juul Jensen, Y. L. Liu, & B. Ralph (Eds.), *Microstructural and Crystallographic Aspects of Recrystallization. Proceedings of the 16th Riso International Symposium on Materials Science* (pp. 193-213). Roskilde, Denmark: Riso National Laboratory.

Vandermeer, R. A. & Rath, B. B. (1989). Modeling recrystallization kinetics in a deformed iron single crystal. *Metallurgical Transactions A (Physical Metallurgy and Materials Science)*, 20A, 391-401.

Vandermeer, R. A. & Rath, B. B. (1989). Modeling of recrystallization. In J. B. Bilde-Sorensen, N. Hansen, D. Juul Jensen, T. Leffers, H. Lilholt, & O. B. Pedersen (Eds.), *Materials Architecture. Proceedings of the 10th Riso International Symposium on Metallurgy and Materials Science* (pp. 589-599). Roskilde, Denmark: Riso National Laboratory.

Wang, X., Esmaeili, S., & Lloyd, D. J. (2006). The sequence of precipitation in the Al-Mg-Si-Cu alloy AA6111. *Metallurgical and Materials Transactions A: Physical Metallurgy and Materials Science*, 37, 2691-2699.

Weiland, H. (1995). Nucleation and growth of recrystallized grains during industrial thermomechanical processing of aluminum alloys. In N. Hansen, D. Juul Jensen, Y. L. Liu, & B. Ralph (Eds.), *Microstructural and Crystallographic Aspects of Recrystallization. Proceedings of the 16th Riso International Symposium on Materials Science* (pp. 215-245). Roskilde, Denmark: Riso National Laboratory.

Weiland, H. (2004). Industrial application of recrystallization control in aluminum products. *Materials Science Forum*, 467-470, 349-356.

Woldt, E. (1992). The relationship between isothermal and non-isothermal description of Johnson-Mehl-Avrami-Kolmogorov kinetics. *Journal of the Physics and Chemistry of Solids*, 53, 521-527.

Woldt, E. & Juul Jensen, D. (1995). Recrystallization kinetics in copper: comparison between techniques. *Metallurgical and Materials Transactions A (Physical Metallurgy and Materials Science)*, 26A, 1717-1724.

Woldt, E. (2001). New kinetic model for primary recrystallization of pure metals. *Metallurgical and Materials Transactions A: Physical Metallurgy and Materials Science*, 32, 2465-2473.

Yassar, R. S., Field, D. P., & Weiland, H. (2005). The effect of predeformation on the β'' and β' precipitates and the role of Q' phase in an Al-Mg-Si alloy; AA6022. *Scripta Materialia*, 53, 299-303.

Yassar, R. S., Field, D. P., & Weiland, H. (2005). The effect of cold deformation on the kinetics of the β'' precipitates in an Al-Mg-Si alloy. *Metallurgical and Materials Transactions A: Physical Metallurgy and Materials Science*, 36, 2059-2065.

Yinnon, H. & Uhlman, D. R. (1983). Applications of thermo analytical techniques to the study of crystallization kinetics in glass-forming liquids, part I: theory. *Journal of Non-Crystalline Solids*, 54, 253-275.

Zakharov, A. M., Gul'din, I. T., Arnol'd, A. A., & Matsenko, Y. (1988). Phase equilibria in the Al-Si-Fe-Mn system within the 10-14% Si, 0-3% Fe and 0-4% Mn concentration interval. *Izvestiya VUZov. Tsvetnaya Metallurgiya*, 4, 89-94.

Zakharov, A. M., Gul'din, I. T., & Arnol'd, A. A. (1989). Phase diagram of the Al-Si-Fe-Mn system in the 10-14% Si, 0-3% Fe, and 0-4% Mn concentration ranges. *Izvestiya Akademii Nauk SSSR. Metally*, 4, 214-218.

Zakharov, A. M., Gul'din, I. T., Arnol'd, A. A., & Matsenko, Y. (1989). Sections of isothermal tetrahedrons of the Al-Si-Fe-Mn system for the 10-14% Si (with up to 3% Fe and 4% Mn) and temperatures between 660 and 580 °C. *Izvestiya VUZov.Tsvetnaya Metallurgiya*, 4, 78-81.

Zhang, H. & Mitchell, B. S. (2000). A method for determining crystallization kinetic parameters from one nonisothermal calorimetric experiment. *Journal of Materials Research*, 15, 1000-1007.

Zhao, Y. M., Wen, W., & Morris, J. G. (2004). The differences in particle structures and recrystallization behaviors between DC and CC AA5052 aluminum alloys. *Materials Science and Engineering A*, 373, 167-174.

Zhen, L., Fei, W. D., Kang, S. B., & Kim, H. W. (1997). Precipitation behaviour of Al-Mg-Si alloys with high silicon content. *Journal of Materials Science*, 32, 1895-1902.

Appendix

Cubic Spline

A cubic spline is a function defined on a mesh of knots x_1, \dots, x_n , $x_i < x_{i+1}$, $i = 1, \dots, n-1$. Within each interval $[x_i, x_{i+1}]$, the spline is a piece of a cubic polynomial. Adjacent polynomials are “glued” in the internal knots in such a way that the spline is twice continuously differentiable function on $[x_1, x_n]$.

The second derivative of the cubic spline is a linear function on $[x_i, x_{i+1}]$:

$$Sp''(x) = m_{i+1} \frac{x - x_i}{h_i} + m_i \frac{x_{i+1} - x}{h_i}, i = 1, \dots, n-1 \quad (A1)$$

where m_i and m_{i+1} are the second derivatives in knots x_i and x_{i+1} , correspondingly, and $h_i \equiv x_{i+1} - x_i$. The expression (A1) ensures the continuity of the second derivative in the inner knots x_2, \dots, x_{n-1} . To obtain the expression for the spline, (A1) has to be integrated twice:

$$Sp(x) = \frac{m_{i+1}}{6h_i} (x - x_i)^3 + \frac{m_i}{6h_i} (x_{i+1} - x)^3 + \frac{C_{i+1}}{h_i} (x - x_i) + \frac{C_i}{h_i} (x_{i+1} - x) \quad (A2)$$

where C_i and C_{i+1} are integration constants. They can be determined using known values of function in knots x_i and x_{i+1} :

$$Sp(x_i) = f_i = \frac{m_i h_i^2}{6} + C_i \Rightarrow C_i = f_i - \frac{m_i h_i^2}{6} \quad (A3)$$

$$Sp(x_{i+1}) = f_{i+1} = \frac{m_{i+1}h_i^2}{6} + C_{i+1} \Rightarrow C_{i+1} = f_{i+1} - \frac{m_{i+1}h_i^2}{6} \quad (A4)$$

Substituting (A3) and (A4) into (A2) and then differentiating the expression obtained, one arrives at the following representation of the first derivative on $[x_i, x_{i+1}]$:

$$Sp'(x) = \frac{m_{i+1}}{2h_i}(x - x_i)^2 - \frac{m_i}{2h_i}(x_{i+1} - x)^2 + \left(\frac{f_{i+1}}{h_i} - \frac{m_{i+1}h_i}{6}\right) - \left(\frac{f_i}{h_i} - \frac{m_ih_i}{6}\right)$$

The requirement that the first derivative of spline must be continuous in the inner knots leads to the following system of linear equations with respect to second derivatives:

$$m_{i-1}\frac{h_{i-1}}{6} + m_i\left(\frac{h_{i-1}}{3} + \frac{h_i}{3}\right) + m_{i+1}\frac{h_i}{6} = \frac{f_{i-1}}{h_{i-1}} - f_i\left(\frac{1}{h_{i-1}} + \frac{1}{h_i}\right) + \frac{f_i}{h_i}, i = 2, \dots, n-1 \quad (A5)$$

While the total number of unknowns is equal to n , the system (A5) contains only $n-2$ equations. If an accurate estimation of the first or second derivative is available in the first and last knots, they can be used as such conditions. Otherwise, the so-called “not-a-knot” conditions are employed:

$$\begin{aligned} Sp'''(x_2 - 0) = Sp'''(x_2 + 0) &\Rightarrow m_1 - 2m_2 + m_3 = 0 \\ Sp'''(x_{n-1} - 0) = Sp'''(x_{n-1} + 0) &\Rightarrow m_{n-2} - 2m_{n-1} + m_n = 0 \end{aligned} \quad (A6)$$

Whatever the choice, two equations representing two boundary conditions can be added to the system (A5) in such a way that its matrix will be tridiagonal with diagonal dominance. The latter means that it is positive definite, which, in turn, prompts that an extremely simple, fast and robust algorithm can be used for building the interpolating cubic spline.